

# Stray Light Measurement and In-Orbit Validation of an Atmospheric Limb Sounder

A DISSERTATION PRESENTED

BY

TOBIAS AUGSPURGER

TO

THE DEPARTMENT OF INSTITUTE FOR ATMOSPHERIC AND ENVIRONMENTAL RESEARCH

IN PARTIAL FULFILLMENT OF THE REQUIREMENTS

FOR THE DEGREE OF

DOCTOR OF NATURAL SCIENCES (DR. RER. NAT.)

IN THE SUBJECT OF

ATMOSPHERIC PHYSICS

UNIVERSITY OF WUPPERTAL

WUPPERTAL, GERMANY

OCTOBER 2024



# Stray Light Measurement and In-Orbit Validation of an Atmospheric Limb Sounder

## ABSTRACT

Stray light characterisation is critical to the success of limb sounder satellite missions, which provide a unique database for atmospheric and climate research. Most satellite missions have relied mainly on stray light simulations without an experimental validation strategy, making it impractical to determine measurement errors caused by stray light. In particular, Spatial Heterodyne Interferometer, which are investigated in this work, lack suitable measurement methods for the impact of stray light and its interference. State-of-the-art stray light simulations are not able to predict interferences from scattering within the instrument based on the nominal design. Therefore, in the context of this work, existing calibration setups for the characterisation of spectral and spatial instrument properties were extended to allow high-resolution and automated stray light measurements based on the point spread function over the entire field of view. The developed Point Source Mapping method allows the analysis of parasitic interference patterns caused by ghost artefacts. In addition, stray light source angles and their sinks can be resolved over the entire detector. When complemented by Ronchi ruling and slit measurements, a comprehensive picture of stray light artefacts and resulting interference can be determined. High resolution out-of-field stray light measurements have been combined with radiative transfer models to reconstruct in-orbit stray light images and their interferences for future correction methods. In addition, in-orbit verification strategies were simulated to replicate pre-launch calibrations based on observations of the Moon and other celestial bodies.

In order to facilitate the early identification of unsuitable instrument configurations during the construction process, the methodologies developed for the measurement of stray light were initially employed as part of the SHIPAS (Spatial Heterodyne Interferometer Performance Assessment in Space), INSPIRESat<sub>3</sub> (International Space Program In Research and Education) and INSPIRESat<sub>4</sub> satellite missions. The stray light measurements and literature review resulted in recommendations for improvements in manual alignment, stray light correction and instrument design. In particular, the use of Ronchi ruling targets for instrument alignment has shown considerable potential. It provides all relevant instrument properties such as signal visibility, stray light and its visibility, spatial resolution and spectral variance to be adjusted from a single experimental setup. By reducing stray light visibility, interference and its effect on the measurement, observational errors can be significantly reduced. The application of an anti-reflection coating to the detector surface was identified as a potential solution to reduce the occurrence of ghost artefacts and thus reduce stray light by an order of magnitude. With these and stray light correction methods for coherent light a reduction in stray light to less than 1% is to be expected with the existing instrument design.

# Streulichtmessung und In-Orbit-Validierung eines atmosphärischen Limb Sounders

## ABSTRACT

Die Charakterisierung von Streulicht spielt eine entscheidende Rolle für den Erfolg der Limb-sounder-Satellitenmissionen, die eine einzigartige Datenquelle für die Atmosphären- und Klimaforschung darstellen. Bislang haben die meisten Satellitenmissionen vorwiegend auf Streulicht Simulationen gesetzt, ohne eine Strategie zur experimentellen Verifizierung zu entwickeln. Dadurch ist es nicht möglich, Messfehler, die durch Streulicht verursacht werden, zu bestimmen. Insbesondere für Spatial Heterodyne Interferometer gibt es bisher keine adäquaten Messverfahren zur Bewertung des Einflusses von Streulicht und dessen Interferenz. Nach dem Stand der Technik sind Streulichtsimulationen nicht in der Lage, Interferenzen durch Streuung innerhalb des Geräts auf der Grundlage des nominalen Designs vorherzusagen. Im Rahmen dieser Dissertation wurden daher bestehende Kalibriereinrichtungen zur Charakterisierung von Spektren und räumlichen Instrumenteneigenschaften erweitert, um hochauflösende und automatisierte Streulichtmessungen auf Basis der Punktspreizfunktion über das gesamte Sichtfeld zu ermöglichen. Die entwickelte Point Source Mapping (PSM) Methode ermöglicht die Analyse parasitärer Interferenzmuster, die durch Geisterartefakte verursacht werden. Des Weiteren können die Einfallswinkel der Streulichtquelle sowie die entsprechenden Senken über den gesamten Detektor hinweg aufgelöst werden. In Kombination mit Ronchi-Ruling- und Schlitzmessungen lässt sich ein umfassendes Bild von Streulicht Artefakten und resultierenden Interferenzen gewinnen. Die Kombination von hochauflösenden Messungen des Streulichts außerhalb des Fokus mit Strahlungstransfermodell ermöglicht die Rekonstruktion von Streulichtbildern und deren Interferenzen während der Mission für die Entwicklung von Korrekturalgorithmen. Darüber hinaus wurden beispielhaft Verifikationsstrategien im Orbit simuliert, um Kalibrierungsexperimente vor dem Start des Satelliten durch Beobachtungen des Mondes und anderer Himmelskörper zu reproduzieren.

Um die frühzeitige Erkennung ungeeigneter Instrumentenkonfigurationen während des Entwicklungsprozesses zu erleichtern, wurden die für die Messung von Streulicht entwickelten Methoden im Rahmen der Satellitenmissionen SHIPAS (Spatial Heterodyne Interferometer Performance Assessment in Space), INSPIRESat<sub>3</sub> (International Space Program In Research and Education) und INSPIRESat<sub>4</sub> erstmals eingesetzt. Die Streulichtmessungen und die Literaturrecherche führten zu Empfehlungen für Verbesserungen bei der manuellen Ausrichtung, der Streulichtkorrektur und dem Instrumentendesign. Insbesondere die Verwendung von Ronchi Ruling Targets für die Instrumentenausrichtung hat sich als sehr nützlich erwiesen. Damit können alle relevanten Instrumenteneigenschaften wie Signal Interferenzkontrast, Streulicht und dessen Interferenzkontrast, räumliche Auflösung und spektrale Varianz mit einem einzigen Versuchsaufbau eingestellt werden. Durch die Verringerung der Interferenzkontrast von Streulicht können Auswirkungen auf den Messfehler erheblich reduziert werden. Das Aufbringen einer Antireflexionsbeschichtung auf die Detektoroberfläche wurde als mögliche Lösung zur Verringerung des Auftretens von Geisterartefakten und damit

zur Reduzierung des Streulichts um eine Größenordnung ermittelt. Mit diesen und Streulichtkorrekturmethode für kohärentes Licht ist bei der bestehenden Gerätekonstruktion eine Reduzierung des Streulichts auf weniger als 1% zu erwarten.

# Contents

1	INTRODUCTION	I
2	SCIENTIFIC OBJECTIVE	5
3	STATE OF THE ART	11
3.1	Spatial Heterodyne Spectrometer . . . . .	12
3.1.1	Imaging Spatial Hedrodyne Spectrometer . . . . .	14
3.1.2	Investigated Instrument Models . . . . .	19
3.2	Forward Model and Data Retrieval . . . . .	20
3.3	Stray Light Definitions . . . . .	20
3.4	Detector and Noise . . . . .	21
3.5	Field-of-View and Limb Perspective . . . . .	23
3.6	Point Spread Function and Deconvolution . . . . .	25
3.7	In-Field Stray Light and Ghosting . . . . .	27
3.8	Spectral Stray Light . . . . .	32
3.9	Out-of-Field Stray Light . . . . .	34
3.10	Stray Light Estimations and Simulations . . . . .	37
3.11	In-Orbit Validation . . . . .	42
3.12	Simulation of Orbits and Line-of-Sight . . . . .	44
4	EXPERIMENTAL SETUP	46
4.1	Modular AtmoX Calibration Unit . . . . .	47
4.2	mACU Alignment and Point Source Configuration . . . . .	48
4.3	Wavefront and Collimation . . . . .	51
4.4	Point Source Assessment . . . . .	53
4.5	Laser Light Source . . . . .	57
4.6	Instrument Stage . . . . .	59
4.7	Calibration Targets for mACU . . . . .	61
4.8	Point Source Mapping . . . . .	63
4.9	Experimental Procedure . . . . .	64
5	DATA PROCESSING AND METHODOLOGY	68
5.1	Pre-Processing and Timing . . . . .	69
5.2	Point Spread Function . . . . .	70
5.3	In-Field Stray Light . . . . .	73
5.3.1	Background Stray Light . . . . .	73

5.3.2	First Order Ghost . . . . .	75
5.3.3	Stray Light Irradiance Distribution . . . . .	78
5.3.4	Ronchi Ruling and Slit . . . . .	79
5.4	Out-of-Field Stray Light . . . . .	83
5.4.1	Point Source Transmittance . . . . .	83
5.4.2	In-Orbit Out-of-Field Stray Light . . . . .	86
5.4.3	Stray Light Measurement Uncertainty and Error . . . . .	89
5.5	In-Orbit Validation and Recalibration Methods . . . . .	92
5.5.1	Moon Observation Maneuver . . . . .	93
5.5.2	Lunar Stray Light and Spatial Resolution . . . . .	96
5.5.3	Limb Scan Maneuver . . . . .	98
6	CONCLUSION AND RECOMMENDATIONS	100
6.1	Assessment of Stray Light and Spatial Resolution . . . . .	102
6.2	Instrument Stray Light Reduction and Correction . . . . .	104
6.3	Evolution of Laboratory Calibration and Methodology . . . . .	106
6.4	In-Orbit Simulation and Validation . . . . .	111
	APPENDIX A APPENDIX	113
	REFERENCES	141
	ACRONYMS	143

THIS WORK IS DEDICATED TO MY WIFE FOR ALL HER LOVE AND PATIENCE.

# Acknowledgments

The creation of this thesis is based on the knowledge and preliminary work of a large number of scientists, engineers and PhD students. This includes in particular the team around the laboratory at the University of Wuppertal. Marco Miebach, Martin Gauß and my predecessor Oliver Wroblowski were essential in constructing the optical setups for generating the experimental data. The transfer of knowledge through joint work and discussion has contributed significantly to the acquisition of the necessary basic knowledge and technical skills required for the scientific investigations described here. The open exchange of mistakes and experiences allowed the further development of existing experiments. Konstantin Ntokas has played a central role in supporting the automation of experimental setups. I'd also like to thank Gregor Gemba, who was a great help with reviewing this thesis.

The development of the instrument is based on the commitment of several people from Forschungszentrum Jülich and the University of Wuppertal. Martin Kaufmann's commitment to advancing the development as a principal investigator, team leader, scientist, and engineer has been inspiring to me. His support, broad knowledge and experience helped to steer this work in the right direction, but also gave me the freedom I needed to follow my own creative path. Special thanks also go to Prof. Dr. Martin Riese (Forschungszentrum Jülich Stratosphere IEK-7), Prof. Dr. Ralf Koppmann and Prof. Dr. Michael C. Volk (both Institute for Atmospheric and Environmental Research, University of Wuppertal) for their confidence, support and time. Without their foresight in atmospheric research and long experience in the development of scientific instruments, the development of a satellite instrument used on several space missions would not have been possible.

The institutes "Electronic Systems" (ZEA-2) and "Engineering and Technology" (ZEA-1) of Forschungszentrum Jülich are also significantly involved in the systems developed in this thesis. Special thanks to Tom Neubert, Heinz Rongen, Guido Offermanns and Heidi Straatmann, who supported me with various mechanical and electrical solutions during our experiments.

During my time at the University of Wuppertal, I was fortunate to have the assistance of several research assistants. These include in particular Friedhelm Olschewski, Peter Knieling and Axel Frohschauer.

I am particularly grateful to my predecessors whose insights paved the way for this work. The prototype developments and the experience from the first AtmoHIT and AtmoSHINE projects have led to the remarkable achievement of equipping four satellites with the developed instrument. These include the theses of: Michael Deiml<sup>1</sup>, Rui Song,<sup>2</sup> Jilin Liu<sup>3</sup>, Qiuyu Chen<sup>4</sup>, Qiucheng Gong<sup>5</sup>, Oliver Wroblowski<sup>6</sup> and Konstantin Ntokas<sup>7</sup>.

A major part of the content and experiments presented here was financed by MetEOC-4 (Metrology for Earth Observation and Climate) in cooperation with the Physikalisch-Technische Bundesanstalt (PTB).

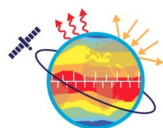
This project [19ENV07 MetEOC-4] has received funding from the EMPIR programme co-financed by the Participating States and from the European Union's Horizon 2020 research and innovation programme.



**BERGISCHE  
UNIVERSITÄT  
WUPPERTAL**



**JÜLICH**  
Forschungszentrum



**Metrology for Earth  
Observation and Climate**



**InOrbit** Demonstration  
Validation  
An EU research and innovation initiative  
funded under EU's Horizon 2020 programme

# 1

## Introduction

Forschungszentrum Jülich, in collaboration with Bergische Universität Wuppertal, has developed a novel limb-sounding satellite instrument based on a Spatial Heterodyne Interferometer (SHI) design. It is ideally suited for space applications, since it is monolithic, without moving parts and enables a high étendue.<sup>8</sup> Unlike conventional SHI designs, the observed object plane is imaged onto two diffraction gratings and this intermediate image is then imaged onto the detector. The Imaging Spatial Heterodyne Interferometer (ISHI) design provides high spectral resolution within a limited bandwidth and high spatial resolution by heterodyning the spectral and spatial information in a 2D image. Compared to conventional spectrometers used in Earth observation, which image a narrow slit, this instrument measures spectral information horizontally and spatial information both hori-



**Figure 1.1:** Different airglow colours in the visible spectrum as seen from the International Space Station at night. The airglow extends from the mesosphere up into the thermosphere. The  $O_2$  A-band maximum can be observed at an altitude of about 90 km in the near infrared spectrum around 763 nm. Credits: NASA

zonally and vertically simultaneously. These features are ideal for obtaining atmospheric composition and dynamics over a wide range of altitudes without the need to scan the instrument's line of sight, as required by conventional spectrometers.

Spectrometers play a key role in Earth-orbiting observation. Installed on an Earth satellite, they provide a unique opportunity to understand global change and its relation to processes in the atmosphere, biosphere and hydrosphere. Proven imaging spectrometers such as TROPOMI<sup>9</sup> on board the Sentinel-5P satellite enable us to understand complex relationships in our Earth systems and provide traceable evidence of global environmental threats such as climate change. Typically, instruments are pointed to the ground in the so called nadir view. The limb view, on the other hand, captures the vertical structure of the atmosphere in more detail, as shown in figure 1.1. A variety of atmospheric limb sounders provide comprehensive data on trends in the atmosphere going back decades. Some aging limb instruments are still operating like ODIN/OSIRIS, AURA/MLS, ACE/FTS-MAESTRO, TIMED/SABER or OMPS-NPP/LS, but they are all beyond their nominal lifetime. This represents a risk for continuous and long-term observation of the upper atmosphere, especially for observations that require high vertical resolution.<sup>10</sup> Innovative, cost-effective, compact and robust instruments can close this gap.

The scientific objective of this work is to develop a comprehensive calibration methodology for the stray light and spatial characteristics of a ISHI instrument installed as an atmospheric limb sounder on several satellite missions. Figure 1.2 shows a typical atmospheric temperature profile that defines

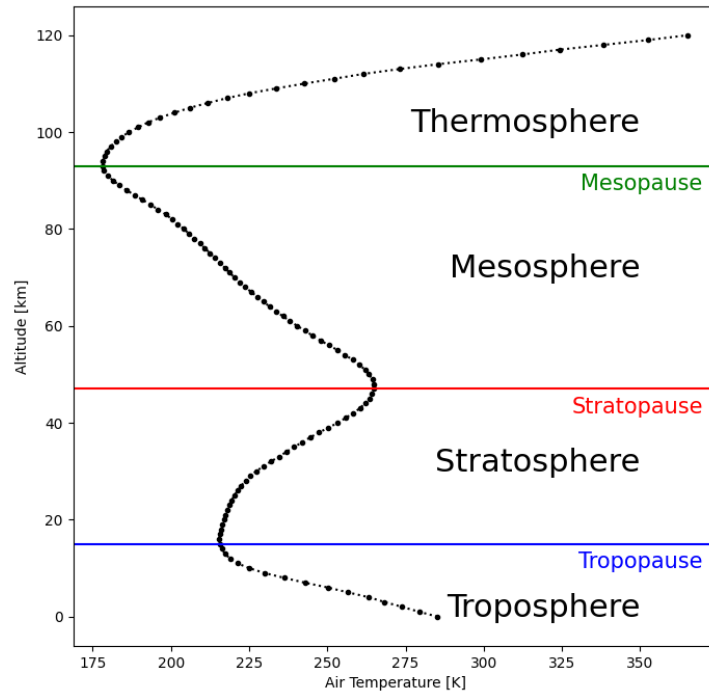


**Figure 1.2:** Temperature lapse rate of MiPAS 2007-Midlatitude Day atmospheric model<sup>11</sup> by using the open source software Joseki.<sup>12</sup> The different atmospheric layers are separated by the tropopause, stratopause and the mesopause by abrupt changes in temperature.

distinct atmospheric layers. The scientific objective of this instrument is to observe the  $O_2$  A-band to derive temperatures distributions in the mesosphere and lower thermosphere. The temperature structures can be used to identify dynamics and wave motions, such as gravity waves, which can influence weather and climate change worldwide. Unlike other methods, no absolute irradiance of the observed  $O_2$  emission is required, and therefore no radiometric calibration of the instrument is necessary. The relative intensities of the emission lines follow a Boltzmann distribution, and the kinetic temperature can be derived from the ratio of the lines.<sup>8</sup> This greatly simplifies the measurement methodology and the physical models required.

To keep the cost and effort of calibration low, while ensuring comparability between different development stages, the instruments go through a pre-launch calibration process followed by in-orbit validation of the experiments. This ensures the reproducibility and traceability of measurements and their uncertainties. The so-called "test as you fly" development principle requires that all operational space conditions are replicated on the ground as part of the calibration process. Pre-launch experiments are then replicated in orbit to study the same instrument characteristics, but under operational

conditions with similar calibration targets.

In this thesis the calibration process and the associated in-orbit validation for the satellite missions INSPIRESat3, INSPIRESat4 and SHIPAS (Spatial Heterodyne Interferometer Performance Assessment in Space) will be further developed with a focus on the stray light and spatial characterisation of the instrument. Although the stray light and spatial characterisation calibration process is applied to an ISHS instrument, the methods presented here are general enough to be applied to other satellite optical instruments. In particular, the fully automated Point Source Mapping (PSM) measurement setup presented here can be applied to a wide range of optical systems for spatial, in-field and out-of-field stray light characterisation on a single test bench. High-resolution acquisition of stray light source angles and sinks opens up new possibilities for stray light correction, evaluation, and validation of stray light simulations.

Furthermore, this thesis presents novel stray light measurement methods using Ronchi ruling and slit targets. These methods enable the measurement of stray light in large image areas, allowing for a quick evaluation of stray light and its visibility. It is also demonstrated that these methods have the potential to adjust all relevant instrument parameters based on a single measurement, making them ideal for fine-tuning instrument performance.

# 2

## Scientific Objective

Gravity waves are a mechanism in the Earth's atmosphere that transfers momentum from the troposphere to the stratosphere, mesosphere and beyond. They are generated by airflow over mountains and other anomalies in the troposphere, such as convection. Also volcanic eruptions generate gravity waves. As the waves reach higher altitudes and encounter, amplitude increases. Nonlinear effects then cause the waves to break, transferring their momentum to the mean flow. The transfer of momentum is responsible for many of the large-scale dynamical features of the atmosphere. Disturbances of the middle atmosphere can affect the dynamics of the lower atmosphere up to tropospheric weather systems and surface temperatures.<sup>13 14</sup> Figure 2.1 shows exemplary the circular propagation of gravity waves from the Hunga Tonga-Hunga Ha'apai volcanic eruption in 2022 as observed by

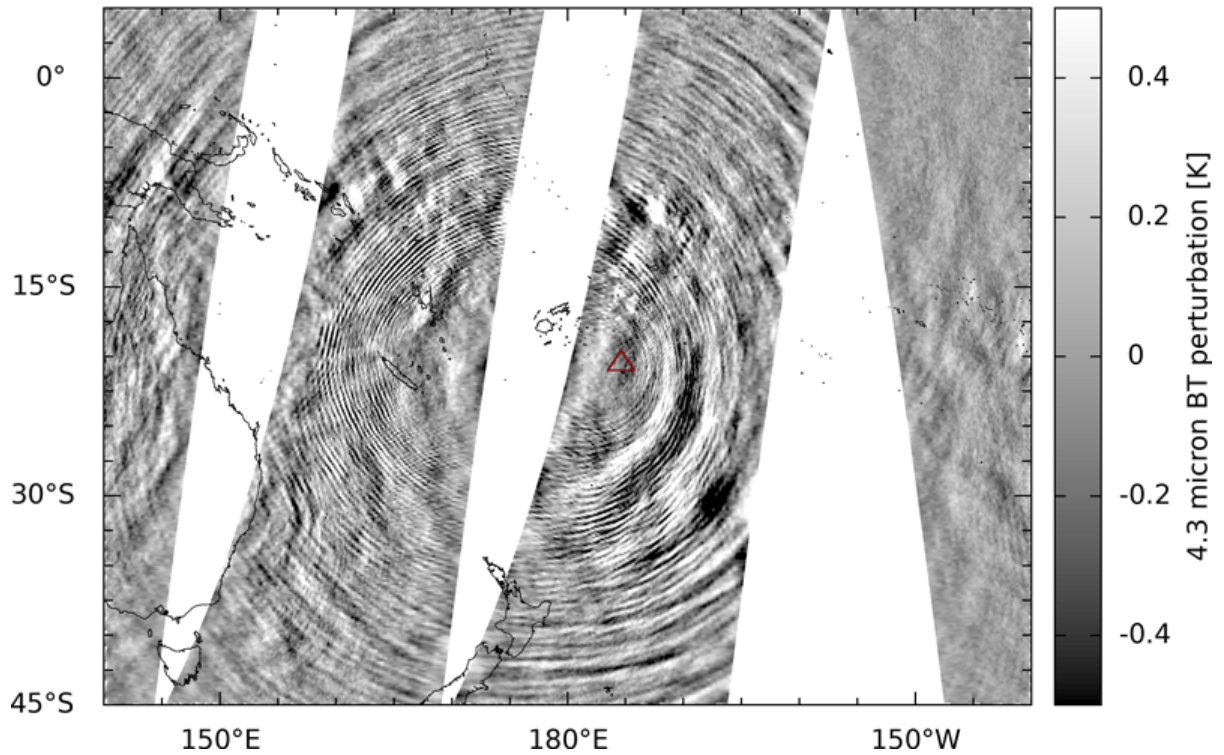


**Figure 2.1:** The gravity waves from the Tonga eruption observed by the AIRS instrument on the NASA's Aqua satellite. Image courtesy of Lars Hoffmann from Forschungszentrum Jülich.<sup>15</sup>

NASA's Aqua satellite using the AIRS instrument 4.3  $\mu\text{m}$  brightness temperature perturbations retrievals.

The Mesosphere and Lower Thermosphere (MLT) atmospheric regions ranges from heights between 50 to 110 km. This region of the atmosphere has distinct characteristics that differentiate it from others. It is the coldest region with a unique property of being cooler in summer than in winter. The summer-winter temperature gradient is due to adiabatic cooling and warming caused by a strong circulation driven mainly by gravity waves. Tides and planetary waves also contribute to the circulation and the large dynamical variability in the MLT.<sup>16</sup>

In order to gain a deeper understanding of the atmospheric dynamics and their impact on climate change, a novel type of SHI has been developed that is capable of resolving temperature structures associated with wave dynamics in a single image.<sup>17,8</sup> The O<sub>2</sub> A-band has been utilised in recent years to obtain global MLT temperatures by instruments like Odin OSIRIS grating spectrometer.<sup>18</sup> By re-

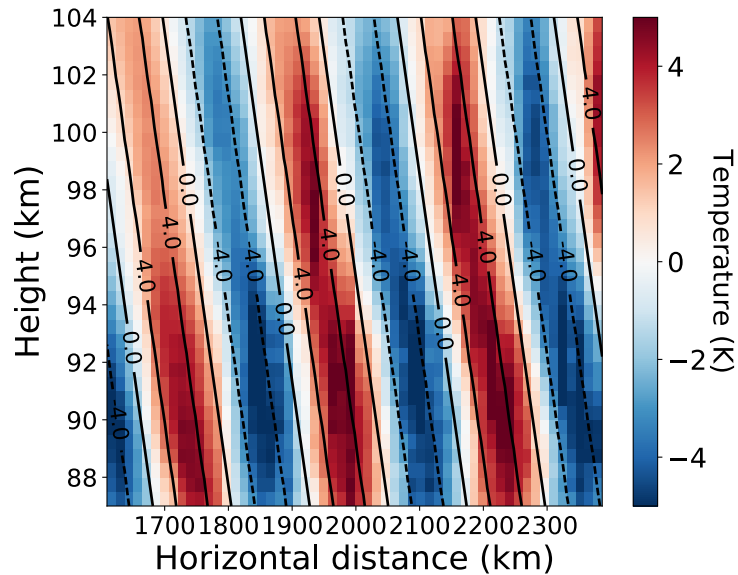
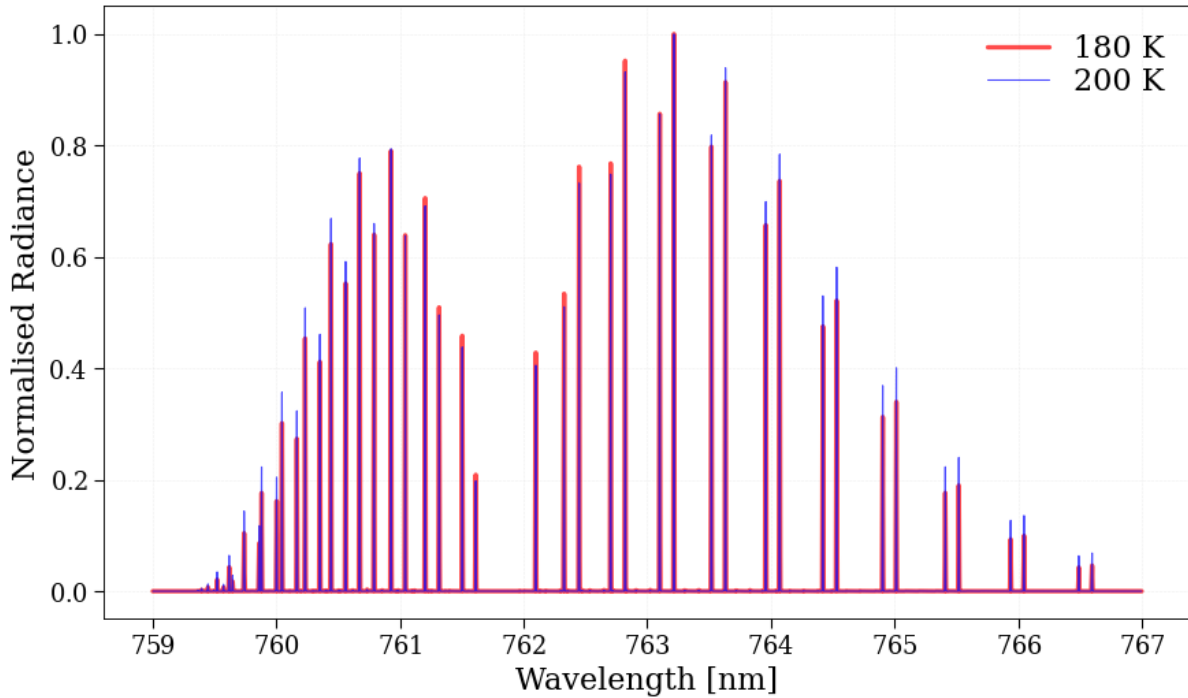


Figure 2.2: Simulation by Rui Song of a typical temperature distribution generated by a gravity wave between 86 and 104 km.<sup>19</sup>

solving temperature gradients with high spatial resolution, simulations have shown that it is possible to observe the temperature fields of wave structures. Figure 2.2 illustrates a simulation showing how temperature variations reveal wave structures from the limb view.

Figure 2.3 shows exemplary the  $O_2$  Atmospheric Band or A-band emission radiance for a kinetic temperature of 180K and 200K. The peak radiance between both states is visible in the peak radiance of the emission spectrum. Since the kinetic temperature is in equilibrium with the rotational temperature of the ground state, the rotational temperature observed in the spectrum is identical to the gas temperature.<sup>20</sup> The spectrum's envelope is measured to determine temperature variability, providing insights into the upper atmosphere's dynamics.

The objective of this thesis is to extend the knowledge of the spatial and stray light characteristics and their impact on the overall scientific objectives. To achieve this, various calibration methods are developed to ensure the reproducibility and traceability of the measurement results and derived atmospheric conditions. The presence of stray light results in radiance being directed towards the imaging sensor, which is not compatible with the instrument's design specifications. In particular, limb sounding techniques suffer from stray light because direct solar radiation and reflections from the Earth interfere with the measurement signal being investigated.<sup>18 23 24</sup> Experience with the first



**Figure 2.3:** Exemplary  $O_2$ -A-band emissions to illustrate the shift in the emission peak ratio between 2 states for a temperature of 180K and 200K for local thermodynamic equilibrium. Simulation are performed with line-by-line radiative code RADIS<sup>21</sup> and the HITRAN database.<sup>22</sup>

technical demonstrators from the AtmoSHINE mission also showed strong stray light image artefacts in the form of ghosts caused by undesired reflections within the instrument.<sup>6</sup> Figure 2.4 shows an in-orbit AtmoSHINE measurement with the  $O_2$ -A band emissions peak at row 820. At row 350 a reflection of this measurement is visible, that is caused by in-field stray light of the instrument. The MIGHTI limb sounding instrument, in operation from 2019 to 2022 on board NASA's ICON satellite, is also based on a SHI design. When observing the airglow, the instrument shows measurement artifacts in the same spectral range. It is presumed that these artifacts can be explained by stray light.<sup>25</sup>

There is a deficit of scientific empirical coverage on stray light in general, including measurement methodologies, validation strategies, and correction algorithms. Specifically, the scientific understanding of stray light in the SHI optical design is limited. Current stray light evaluations are typically simulation-based using frameworks where the underlying source code is not accessible. Such an approach lacks the necessary traceability, and the necessary adaptations to analyse stray light in-

467 th, 8 s, 2019-05-21 13:17:07, 98.64 km , lat -17.0°, lon 107.4°

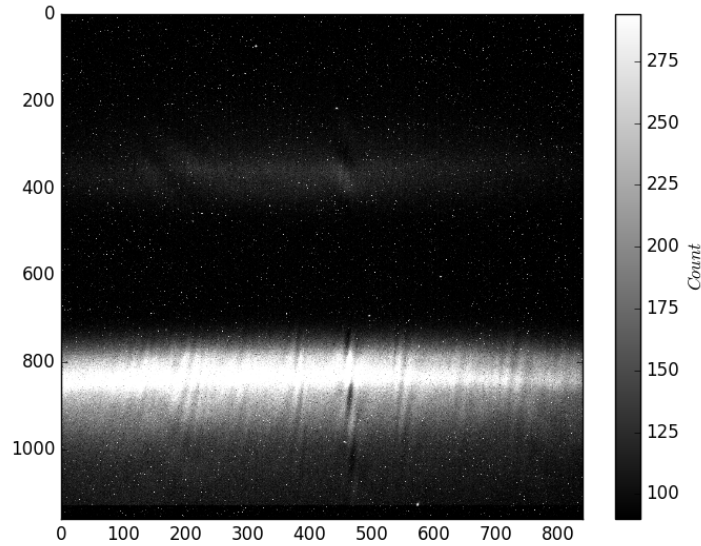


**Figure 2.4:** In-Orbit Nighttime airglow observation at an altitude of about 90 km with the AtmoSHINE instrument. Ghost artefacts as one type of stray light causes the airglow at line 820 to be reflected to higher altitudes around line 350.

terference in SHI cannot be implemented in current closed-source models. Therefore, the following objectives were set for the thesis:

1. Prepare a review of existing experimental measurement methods for stray light and spatial characterisation with subsequent in-orbit validation strategies.
2. Based on the existing experimental setup, a stray light and spatial calibration setup should be created that is traceable to known standards, reproducible between different instrument versions, and similar to light sources observable in orbit.
3. Perform stray light measurements inside and outside the field of view of the instrument, including spatial resolutions over the entire field of view, and compare with existing total stray light requirements of 1%.<sup>6</sup>
4. Establish an in-orbit validation strategy for both in-field and out-of-field stray light, including spatial characterisation.

5. Propose stray light improvements in the instrument design and calibration process, including stray light correction methods and requirements.

# 3

## State of the Art

”STANDING ON THE SHOULDER OF GIANTS”. Isaac Newton used this metaphor to illustrate the core of the scientific process: constantly reprocessing and expanding existing knowledge. In the field of spaceflight and earth observation, it is crucial to build on the experience of previous missions due to the high costs associated with development, operation, and launch. Hardware changes are typically not possible after launch. As a result, scientists and engineers can only learn from the extensive experience of missions already performed. A successful satellite mission therefore requires extensive literature research and experience. This chapter provides an overview of the existing scientific basis and experience with similar satellite instruments:

### 3.1 SPATIAL HETERODYNE SPECTROMETER

The first approaches to the development of a Spatial Heterodyne Interferometer (SHI) go back to Pierre Connes in 1958.<sup>26</sup> As part of his research, he showed that the moving mirrors of a Michelson interferometer could be replaced by tilted diffraction gratings without losing the ability to measure multiple wavelengths simultaneously on a 2D screen. This eliminates the need for moving parts in the optical design, making it particularly interesting for space applications where low maintenance and robust designs are preferred.

However, it was not until the development of high resolution digital image sensors in the early 1990s that this development became applicable for Earth observation. John Harlander and Christoph Englert continued to develop this optical design. Through a large number of scientific publications, they laid the scientific foundation for a wide range of other designs. By introducing the field-widening technique, more than two times the etendue of a classical optical spectrometer could be realized.<sup>27</sup>

During further research, relevant design features of the instrument such as flat-fielding<sup>28</sup> or phase distortion correction<sup>29</sup> have been improved. The first optical designs are based on a non-imaging SHI. Thus, the entire atmospheric column within the field of view (FOV) of the instrument contributes to the spectral signal. The development of ISHI designs made it possible to separate spatial and spectral information within the measured signal.<sup>30 31 32</sup> This development is a result of the previous design called HEIFTS (High Etendue Imaging Fourier Transform Spectrometer).<sup>33</sup> These design studies laid the foundation for several satellite missions and atmospheric science instruments:

- SHIMMER (Spatial Heterodyne Imager for Mesospheric Radicals) was the first SHI system in space, launched 2007 on the the Satellite STPSat-1.<sup>34</sup> It was designed specifically to make global measurements of hydroxyl (-OH) in the middle atmosphere from low Earth orbit.<sup>35</sup> However the first publication on the instrument reach back to 2002.<sup>36 37</sup> The comparison of the design with the predecessor spectrometer MAHRSI shows a significant increase in performance. "Despite its small size and great simplicity, laboratory calibrations demonstrate that

the responsivity of SHIMMER is more than 10,000 times larger than MAHRSI and its spectral resolution (0.0058 nm) is 3.5 times better.”<sup>36</sup>

- SHOW’s (Spatial Heterodyne Observations of Water) primary objective was the development of a new instrument designed to measure water vapour at the upper troposphere, through the stratosphere and into the lower mesosphere, on a global scale, using the unique capabilities provided by the SHI design.<sup>38</sup> This instrument has so far only been installed on a NASA ER-2 aircraft, but a satellite design is planned.<sup>39</sup>
- DASH (Doppler asymmetric spatial heterodyne spectroscopy) is a patented<sup>40</sup> design variant of an SHI which allows to detect a phase shift within the measured spectrum by offsetting one of the gratings. This enabled the measurement of the Doppler shift in the signal and thus the wind speed in the atmosphere.<sup>41</sup> Based on these design studies the instrument MIGHTI (Global High-Resolution Thermospheric Imaging) was developed and launched in 2019 on NASA’s Ionospheric Connection Explorer (ICON) satellite.<sup>42</sup> The instrument was designed to measure thermospheric horizontal wind velocity profiles and thermospheric temperature in altitude regions between 90 km and 300 km, during day and night.<sup>43</sup> Daytime MIGHTI temperatures are on average 18 K higher in the 99-105 km altitude range than coincident observations by the Sounding of the Atmosphere using Broadband Emission Radiometry (SABER) instrument on NASA’s TIMED satellite.<sup>25</sup> The first in-orbit data from this mission have significantly improved our understanding of how solar storms<sup>44</sup> or the eruption of the Hunga Tonga-Hunga Ha’ap volcano affected the upper atmosphere.<sup>45</sup> Data from this mission is freely available at the [ICON website](#) including data tutorials. Interferometer for Neutral-Thermosphere Dynamics Imaging (INDI) is another DASH based design that is currently under development. It targeted to measure red-line ( $\lambda=630.0$  nm) oxygen with a small footprint that will fit in a 6U cubesat or smallsat.<sup>46 47 48</sup>
- AtmoSHINE was the first ISHI on a satellite, which was successfully deployed in 2018 into a sun-synchronous orbit.<sup>49</sup> It obtained data from in-orbit measurements, resolving O<sub>2</sub> A-band

emissions.<sup>34</sup> The resulting measurement data made it possible to comprehensively analyse the newly developed board electronics and detector in space operation.<sup>50 51</sup>

- GMI (Greenhouse Gas Monitoring Instrument) was launched on two Chinese Satellites on board (GF-5) in 2018 and GF5-02 in 2021. Unlike previous designs for atmospheric science, these four band SHI systems explore the atmosphere from the nadir perspective. Earlier instrument implementations captured the atmospheric properties from the limb perspective. "GMI has four optical channels: the O<sub>2</sub> channel (0.765 μm), the CO<sub>2</sub> weak absorption channel (1.575 μm) (defined as CO<sub>2</sub>-1), the CO<sub>2</sub> strong absorption channel (2.050 μm) (defined as CO<sub>2</sub>-2) and the CH<sub>4</sub> channel (1.650 μm)."<sup>52 53</sup>

### 3.1.1 IMAGING SPATIAL HEDRODYNE SPECTROMETER

The schematic optical diagram of a field-widened ISHI system is shown in figure 3.1. The incoming wavefront is filtered by an interference filter to limit the incoming spectrum to the bandwidth of the investigated O<sub>2</sub> A-band emissions. Depending on whether it is an ISHI or a conventional SHI design, the wavefront is either focused or collimated on the diffraction grating. The beam splitter cube divides the wavefront into two coherent arms equally. These arms are then followed by a field-widening prism to increase the FOV. At the end of each arm is a blazed diffraction grating with the groove density  $\frac{1}{d}$  being tilted relative to the optical axis by the Littrow angle  $\theta_L$ . Depending on the incoming wavenumber  $\sigma$  the wavefront is reflected at the grating by the angle  $\gamma$  according to equation 3.1<sup>27</sup>. Wavenumber, as used in spectroscopy and most chemistry fields, is defined as the number of wavelengths  $\lambda$  per unit distance centimetre according to equation 3.2.

$$\sigma(\sin(\theta_L) + \sin(\theta_L - \gamma)) = \frac{m}{d} \quad (3.1)$$

$$\sigma = \frac{1}{\lambda} \quad (3.2)$$

$\sigma_L$  refers to the Littrow wavenumber at which wavefront is reflected back into the same direction

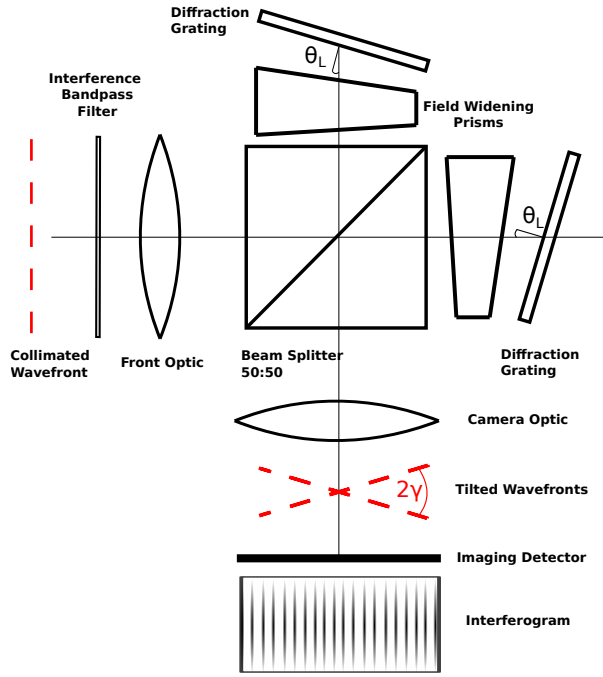


**Figure 3.1:** The core component that forms the interferogram is the Spatial Heterodyne Interferometer (SHI), which consists of diffraction gratings, field widening prisms, and the beam splitter.

as the incoming wavefront.  $m$  is the order of diffraction. The following equations can be used to determine the Littrow wavenumber:

$$\sigma_L = \frac{m}{2d \sin \theta_L} \quad (3.3)$$

In this so-called Littrow configuration, the diffracted optical power  $P$  is highest in the first diffraction order  $m = 1$  with a diffraction efficiency  $\eta$  relative to incident power  $P_i$ . The remaining power in the other orders must be suppressed so that it does not contribute to the measurement signal in the form of stray light:

$$\eta = \frac{P_d}{P_i} \quad (3.4)$$

After the wavefront has been diffracted at the gratings and tilted by  $\gamma$  depending on the wavenumber, both wavefronts pass the beam splitter again. This results in 50% of the light leaving the instrument through the front optics and not contributing to the measurement signal. The remaining light

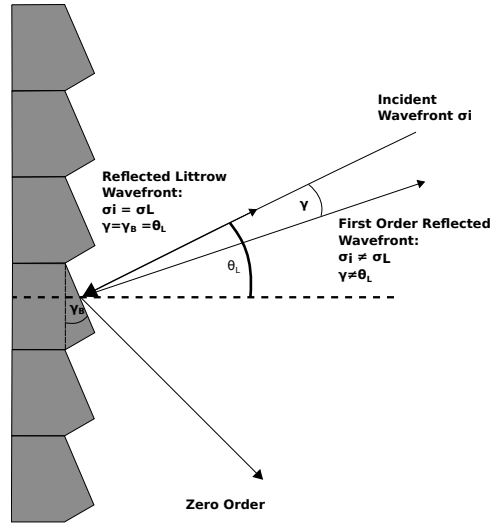


**Figure 3.2:** Blazed diffraction grating in Littrow configuration. The reflected wavefront is tilted by the angle  $\gamma$  depending on the wavelength.

is focused on the detector surface by the camera optics. The beam splitter and the grating are aligned so that the focal plane of the camera optics is on the surface of both gratings. Due to the difference in Optical Path Length (OPL) and the resulting phase differences, the two coherent wavefronts interfere, creating a 2D interferogram at the detector plane. When observing a monochromatic light source with an ideal instrument, the interferogram appears sinusoidal in the horizontal detector direction  $x$ , but has no modulation in the vertical direction  $y$ . The spatial frequency  $f_x$  of such an interferogram can be described by the equation 3.5<sup>30</sup>:

$$f_x = 4\theta_L \tan(\sigma - \sigma_L) \quad (3.5)$$

In case of a light source with spectral radiance  $B$ , which itself consists of a spectral density within the entire bandwidth  $\sigma_{max}$  to  $\sigma_{min}$ , the integral over the infinitesimal wavenumber  $d\sigma$  in the x-direction of the detector gives the intensity  $I$  as defined by the equation 3.6:

$$I(x) = \int_{\sigma_{min}}^{\sigma_{max}} B(\sigma) [1 + V(x, \sigma) \cos(2\pi f_x + \delta(x, \sigma))] d\sigma \quad (3.6)$$

The equation introduces two essential quantities to approximate the model to the real physical bonds:

1. Interferometric visibility, or simply visibility, denoted by  $V$ , is a measure of the contrast of interference in any system subject to wave superposition. In the context of an SHI, it is the modulation depth that the interferogram can reach, taking into account the limitations of the optical systems. This includes variation of the beam splitter ratio and the resulting unbalance of the power between the two arms. As a result, the entire power cannot be superimposed uniformly. Another deviation of the power balance between both arms can be caused by imbalance in diffraction efficiency  $\eta$ . The limitation of the spatial resolution of the camera optics can also lead to a reduction in visibility. Equation 3.7 shows how visibility is defined for a single detector line, using the maximum envelope function  $I_{max}$  and the minimum envelope  $I_{min}$  as can be seen in figure 3.11 and figure 3.3:

$$V(x, \eta, r, \dots) = \frac{I_{max} - I_{min}}{I_{max} + I_{min}} \quad (3.7)$$

Under ideal conditions, the total incident power contributes to the interference and thus corresponds to the numerical optical design of the instrument. The visibility is thus 100%. The temporal coherence length is the difference in OPL at which the visibility decreases to  $1/e = 37\%$ .<sup>54</sup>

2. The phase distortion  $\delta$  causes the interferogram fringes to rotate. This can be caused by distortion of the camera optics or slight misalignment of the gratings. Phase distortion can generally be corrected without significant loss of the signal-to-noise ratio.<sup>29</sup>

Figure 3.3 illustrates typical spectral and visibility data generated with an early stage SHIPAS Qualification Model (QM) instrument and a homogeneous narrow-band laser light source of 761.42 nm. The visibility heatmap shows the modulation depths over entire FOV. The sliding window's visibility was estimated by scaling its size according to the interferogram's period. The central section illustrates the modulation of the mean of 10 horizontal image lines by the laser wavelength. Within the spectrum, the low frequencies indicate that the unmodulated part of the interferogram is also

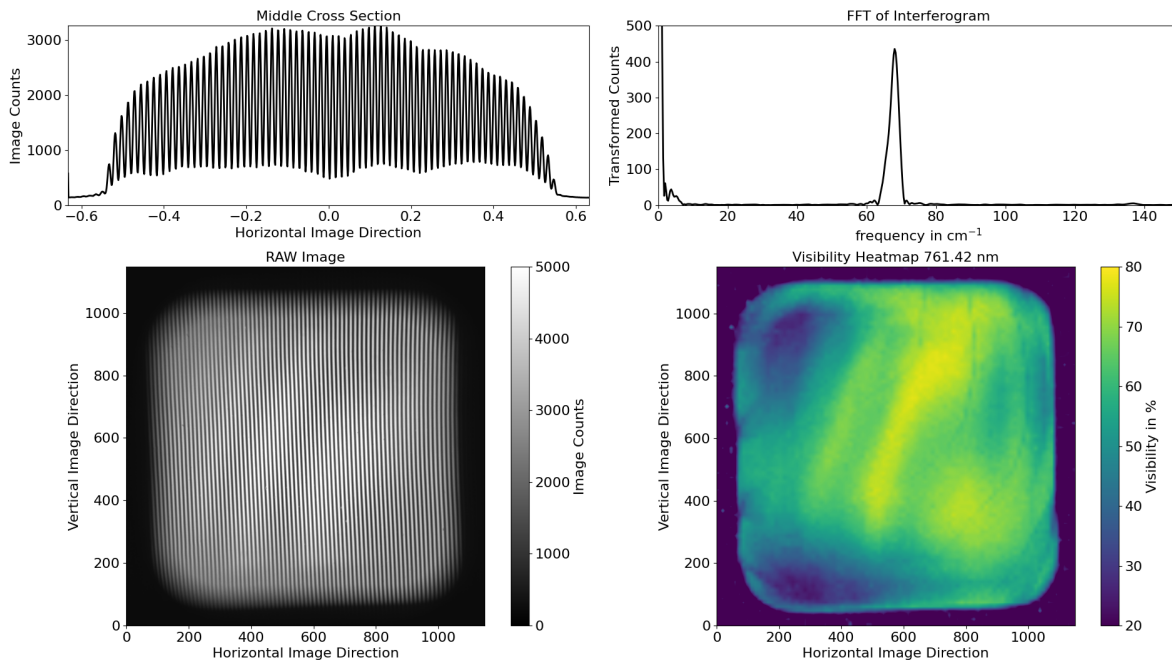


**Figure 3.3:** Calibration data in the very early design phase of the first qualification model for the SHIPAS mission. The instrument is stimulated by a monochromatic laser light source of 761.42 nm. The **RAW Image** show the homogenous frequency of the interferences. The **Middle Cross Section** illustrates the high interference contrast, also known as visibility. The **FFT of Interferogram** cross section shows a single peak at about  $68 \text{ cm}^{-1}$ . For the **Visibility Heatmap**, the visibility is not evaluated for the whole cross section as defined in equation 3.7, but for a window function to reveal the 2D profile of the visibility trend.

present. The image distortion caused by the camera optics is not corrected in this simplified data processing, resulting in an deviated representation of the interferogram in the corner of the image.

The required spectral resolving power  $R$  to separate the emission line of the target spectrum are defined by equation 3.8. The difference  $\Delta\sigma$  is defined between adjacent emission lines that have a relative emission intensity of more than one percent at a background atmospheric temperature of 200 K referring the  $O_2$  A-Band at a center wavenumber  $\sigma$  of  $13127\text{ cm}^{-1}$ .<sup>6</sup>

$$R = \frac{\sigma}{\Delta\sigma} \quad (3.8)$$

The spectral resolving power  $R$  can be determined with reference to the diffraction gratings specifications by the following equation given the illuminated grating area width  $W$  and grating groove densities  $\frac{1}{d}$ :

$$R = 2 \cdot W \cdot \frac{1}{d} \quad (3.9)$$

### 3.1.2 INVESTIGATED INSTRUMENT MODELS

The optical design of the ISHI instruments used as part of the investigated satellite mission is referred to as AtmoLITE design within this thesis. The optical design has been developed in ZEMAX Optical Studio based on the experience with the AtmoSHINE design. Further specifications can be found in table A.1.<sup>6</sup> During the first instrument calibration with this novel optical design as part of the INSPIRESat-4 mission in 2021, a correlation between instrument temperature and optical performance was found.<sup>5</sup> This is likely due to the aluminum optomechanics, which have been shown to expand thermally in a thermal vacuum chamber. In conclusion, for the SHIPAS mission, an optomechanics made of Invar was developed, which has a lower thermal expansion compared to aluminum under the expected thermal range in space. The novel optomechanics also provides additional degrees of freedom for adjusting the front lens and camera optics to improve the instrument alignment process. Figure A.1 shows the main optical components of the first QM as part of the SHIPAS mission. The optomechanical design of this thesis was familiarized using the SHIPAS QM instrument

version and the stray light calibration process was developed. It is important to note that this is not the Flight Model (FM) that will be delivered for the SHIPAS mission.

### 3.2 FORWARD MODEL AND DATA RETRIEVAL

For the data processing of the instrument a forward model is coupled with a retrieval algorithm. The forward model simulates the physical properties of the whole observation by the instrument including: The modelled atmosphere,  $O_2$  A-Band emissions, the radiative transfer of the measurement signal and the instrument itself. The forward model simulates the measurement signal for a given atmospheric state (temperature, trace gases), taking into account radiation transfer and instrument characteristics.<sup>1</sup> Since light from the observed measuring volume passes through multiple atmospheric layers to the limb sounder, physical properties like absorption must also be included in the forward model and are based on experience of previous limb sounder developments.<sup>55,4</sup> These simulations serve not only to define detailed requirements for planned missions, but also to investigate possible future missions.<sup>56</sup> Figure A.15 shows exemplary a simulated airglow observation observed from space with airglow intensity peak in the middle cross section of the image. The horizontal modulation in the intensity represents the interferogram caused by the observed emission lines.

### 3.3 STRAY LIGHT DEFINITIONS

*”Stray light is defined as unwanted light that reaches the focal plane of an optical system.”*<sup>57</sup> This definition is still widely used in the literature, although it does not accurately describe what is referred to as stray light in state-of-the-art publications. For example, the ISHI has three different focal planes, which theoretically requires three different stray light values. The term ”unwanted light” can also be misleading, as ”wanted light” can also lead to stray light when reaching the wrong position on the detector. A better definition would be: *Radiance on a detector due to undesired scattering, reflection or diffraction effects within an optical system.* There are also only a few conclusive mathematical definitions of stray light that can be found consistently in the scientific literature. Therefore, quantitative comparisons between different optical systems are often not applicable. Stray light levels are highly

dependent on predefined spatial boundaries between what is still considered as part of the signal<sup>58</sup> and the assessment methods chosen. Scattering within the FOV but outside the instrument is also not considered as part of the stray light. The scattering of the atmosphere is already covered by the radiative transfer model of the data retrieval. Scattering on components surrounding the instrument, such as satellite solar panels, plays a special role. Although they are not located within the instrument, they still can be considered as part of the instrument and therefore cause stray light.

In the following, we will concentrate primarily on in-field and out-of-field stray light. Other stray light effects such as out-of-band stray light<sup>59</sup> will not be considered in this thesis. Such effects are caused by light transmission outside the bandpass, which results in light outside the nominal spectrum passing through the bandpass filter at the first aperture of the instrument. However, the spectral stray light is part of the further examination. In spectrographs, spectral stray light causes the spectral linespread function (LSF) to broaden due to cross talk between different spectral lines: "The LSF describes the spectral stray light and is conceptually equivalent to the point-spread function that is used to describe the spatial stray light response of an instrument."<sup>60</sup> This artefact can be caused by stray light sources inside and outside the FOV.

### 3.4 DETECTOR AND NOISE

To evaluate the impact of stray light from different field angles on the detector, it is necessary to distinguish between very low signal levels and detector noise artifacts. The GSENSE400BSI detector was chosen because of its low noise, high dynamic range and high external quantum efficiency at the observed wavelength of about 763 nm. Table 3.1 summarise the essential quantities relevant for the stray light evaluation.

The noise produced by the detector consists of five distinct types of noise<sup>62,63</sup>:

- Dark current  $\sigma_D$  is a thermal phenomenon that results in the flow of current within the silicon chip, even when no photons are incident on the camera. This is caused by electrons being spontaneously generated within the chip, as valence electrons are thermally excited into the conduction band.

**Table 3.1:** The specifications of the image detector, as provided by the manufacturer in the datasheet.<sup>61</sup>

Detector Type	GSENSE400BSI (CMOS)
Dark Current	$0.27 e^-/\text{pixel/s}$ @40°C
Readout Noise	$1.6 e^-$
Fix Pattern Noise	$1.6 e^-$
Discharging Lag Noise	$2 e^-$
Dynamic range	94dB (HDR mode)
Detector AR Coating	None
Illuminated Detector Plane	approx. 20 mm x 18.2 mm
Illuminated Pixels	approx. 1100 Vertical x 1000 Horizontal

- Readout Noise  $\sigma_R$  is the amount of electronic noise generated during the transfer of charge from the pixels to the readout electronics.
- Photon Shot Noise  $\sigma_S$  is the statistical noise that occurs when discrete photons arrive at the pixel with a certain probability.
- Fixed Pattern Noise  $\sigma_F$  is caused by non-uniformities of the pixels, which is independent of the signal level and the temperature of the sensor. Figure A.2 illustrates the fix pattern offset that becomes visible for very low exposure times of 1ms.
- Discharging lag noise  $\sigma_L$  is caused by overexposing the pixel beyond their full well capacity with a sudden decrease of irradiance.<sup>63</sup>

$$\sigma_{total} = \sqrt{\sigma_D^2 + \sigma_R^2 + \sigma_F^2 + \sigma_L^2} \quad (3.10)$$

Equation 3.10 defines the Total Effective Noise  $\sigma_{total}$  of the individual noise artifacts that are independent of the signal level. To accurately quantify stray light, it is necessary to know all the counts of the detector caused by temperature drift and other noise source. As in-field and out-of-field stray light affects the entire detector area, a large number of pixels and their detector noise uncertainties can lead to high uncertainty in stray light assessment. Especially when using small light sources, which make it possible to determine the propagation of stray light, signal level can be in the order of magnitude of the detector noise.

In particular, measurements taken over a long period of time may show fluctuations in detector temperature and therefore different dark current and readout noise values. Therefore, stray light measurements use optical choppers or controlled light sources that allow rapid on/off switching. This allows dark images to be obtained continuously for each measurement.<sup>64</sup> Such sudden changes in illumination can cause other noise effects, such as the discharging lag noise  $\sigma_L$ , which must be taken into account. By subtracting the dark image from the signal image, signal independent noise effects can be subtracted from the stray light measurement. This leaves the photon shot noise  $\sigma_S$  as the largest detector noise contributor to the stray light uncertainty.

### 3.5 FIELD-OF-VIEW AND LIMB PERSPECTIVE

Understanding the Field-of-View (FOV) of the instrument is essential for the interpretation of the measurement data. It defines the geometric extension of the light cone from the object plane at the tangent point of the atmosphere to the image plane in the instrument. Ideally, no other light should reach the detector outside this angular range. The line-of-sight (LOS) is the path of a light beam that is perpendicular to the object and image plane. For a FOV that is symmetrical in the horizontal and vertical directions, the LOS is the axis of symmetry for the FOV. Intensive research has shown that the definition of LOS in the literature is ambiguous in relation to the optical axis of the instrument. Within this work, the LOS is therefore equated with the light ray that passes perpendicular through the centre of the first aperture. This assumption is also the basis for the calibration of the LOS during the prelaunch calibration of the instrument.<sup>6</sup> This calibration is highly relevant for limb-viewing instruments. Unlike nadir-viewing satellite instruments, LOS uncertainties and variations cannot be continuously referenced by ground control points. Uncertainties in the line of sight can be caused by the thermal expansion of the satellite body or instrument, uncertainties in the mounting of the instrument or by the pointing error of the spacecraft attitude control.<sup>65 66</sup>

Figure 3.4 outlines the basic dimensions of the limb sounder geometry. Assuming the object plane is exactly on the tangent point between the LOS and the atmosphere, the geometries of the observation can be estimated using simple trigonometry. Table 3.2 shows the derived pitch angle  $U =$

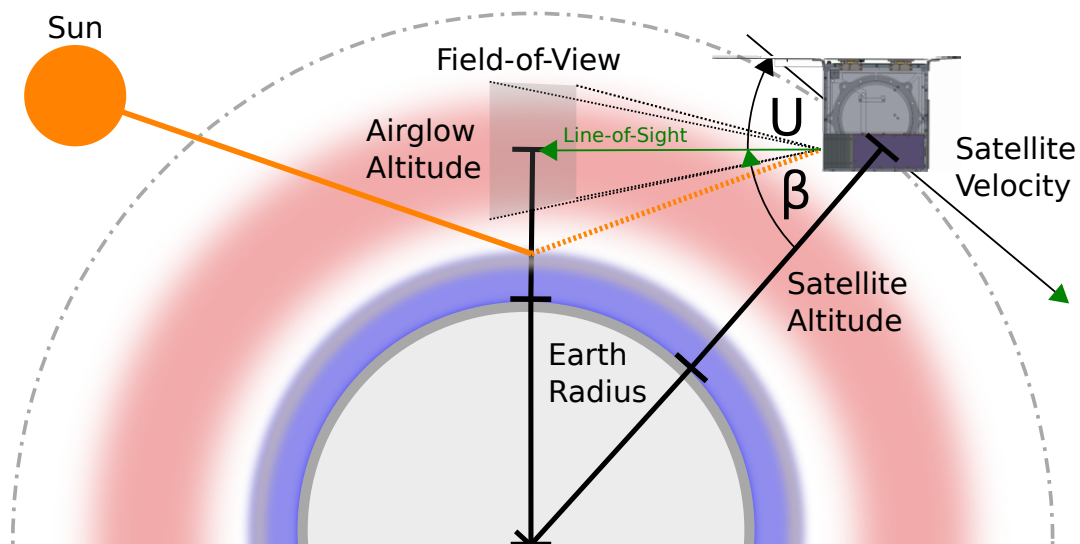


**Figure 3.4:** Exemplary limb sounding geometry with the LOS tangential to the target atmospheric layer where the peak airglow signal is expected. Sunlight scattering at lower altitudes, especially from clouds, is expected to be the highest out-of-field stray light source.

-26.095 deg of the satellite relative to the velocity vector assuming a spherical earth shape and pointing the LOS at the tangent point of 90 km. Relevant out-of-field stray light from this perspective is caused by the Sun, the Moon and, above all, by reflection and scattering in the lower atmosphere, especially clouds. Similar instruments reported a positive correlation between cloudiness and out-of-field stray light, specially at the red end of the spectrum.<sup>67</sup> For the similar MIGHTI instrument, the bright Earth below the FOV and the Sun whenever it is in the front quadrant were also identified as the main sources of out-of-field stray light.<sup>43</sup>

**Table 3.2:** An example of the dimensions of the limb-sounding perspective using the sun-synchronous orbit of Sentinel 5p. The simulation was performed with the help of the open source project Skyfield.<sup>68</sup>

Altitude of Satellite	830.51 km
LOS Tangent Point Altitude	90 km
Observation Distance	3180.73 km
Pitch Angle $U$ of Instrument	-26.1 deg
Off-Nadir Angle $\beta$ of Instrument	-63.9 deg
Field-of-View	1.4 deg x 1.4 deg
Object Plane	77.72km x 77.72km

### 3.6 POINT SPREAD FUNCTION AND DECONVOLUTION

The Point Spread Function (PSF) describes the response of an imaging system to an incoherent point light source. It can be thought of as the expanded spot in an image that represents a single point object, a single spatial impulse. In functional terms, it is the inverse Fourier transform of the Optical Transfer Function (OTF) of a incoherent imaging system.<sup>69</sup> The PSF therefore describes how the object of the optical system is transformed into the image, without taking into account possible interference caused by coherent light. For coherent imaging, the equivalent is referred to as the coherent transfer function and coherent point spread function.<sup>70</sup> In observational astronomy, the abundance of point sources provided by stars often makes the experimental determination of a PSF straightforward. If atmospheric reanalysis data is included in the PSF simulation, even atmospheric aberration can be taken into account, as has been shown in the processing of astronomical data.<sup>71</sup> Such point sources can also be created in the laboratory to determine the pre-launch performance of earth observation instruments.<sup>72</sup>

So far, the PSF measurements from the AtmoLITE or InspireSat4 instruments differ significantly in shape and magnitude from the values expected from the simulation.<sup>65</sup> One possible reason for this is the lack of a reference telescope as part of the alignment process to validate the shape of the point source. However, the Modulation Transfer Function (MTF) was successfully determined as a 1D representation of the PSF in one direction of the image. The MTF is formally defined as the magnitude (absolute value) of the complex OTF.

Figure 3.5 illustrates the convolution of the object with the PSF resulting in the observed image. The chosen point spread function represents an airy disc, the PSF of the best-focused spot of light that a perfect lens with a circular aperture can achieve, limited by the diffraction of light. Considering an object  $f$  as a function of the object coordinates  $x$  and  $y$ , the object is convolved by the point spread function  $h$  to produce the image  $g$ . (see equation 3.11). Then, both sides of the equation are transformed to the frequency domain using the Fourier transform, resulting in the equation 3.12. Thus, the convolution is transformed into a matrix multiplication, which allows the reconstruction of the

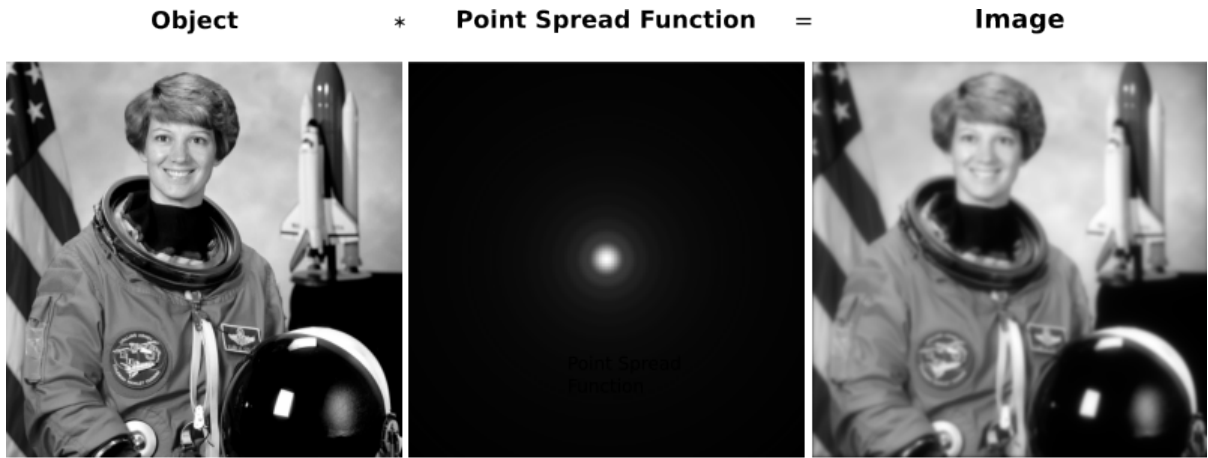


**Figure 3.5:** The object is convolved with the ideal airy disk-shaped PSF, resulting in a bluish image of the object. Data processing was done using scikit-image<sup>73</sup>, convolution methods from SciPy<sup>74</sup> and an airy disk model from AstroPy<sup>75</sup>

object in the frequency domain by dividing the image by the PSF in the frequency domain. By taking the inverse Fourier transform of the reconstructed image in the frequency domain, the original image is reconstructed in the spatial domain.

$$f(x, y) * h(x, y) = g(x, y) \quad (3.11)$$

$$F(uv) \cdot H(u, v) = G(u, v) \quad (3.12)$$

$$F(uv) = \frac{G(u, v)}{H(u, v)} \quad (3.13)$$

$$f(x, y) = \mathcal{F}^{-1}\left(\frac{G(u, v)}{H(u, v)}\right) \quad (3.14)$$

This simplified consideration assumes a noise-free image. A non-ideal image also contains detector noise, as described in equation 3.4, resulting in equation 3.15.

$$f(x, y) * h(x, y) + \sigma_{total}(x, y) = g(x, y) \quad (3.15)$$

Without prior knowledge of the noise to signal ratio (NSR) of the image, simple deconvolution can result in amplifying the noise rather than the signal of the image. Methods such as the Wiener deconvolution<sup>76</sup> attempt to overcome this problem by integrating the NSR into the deconvolution

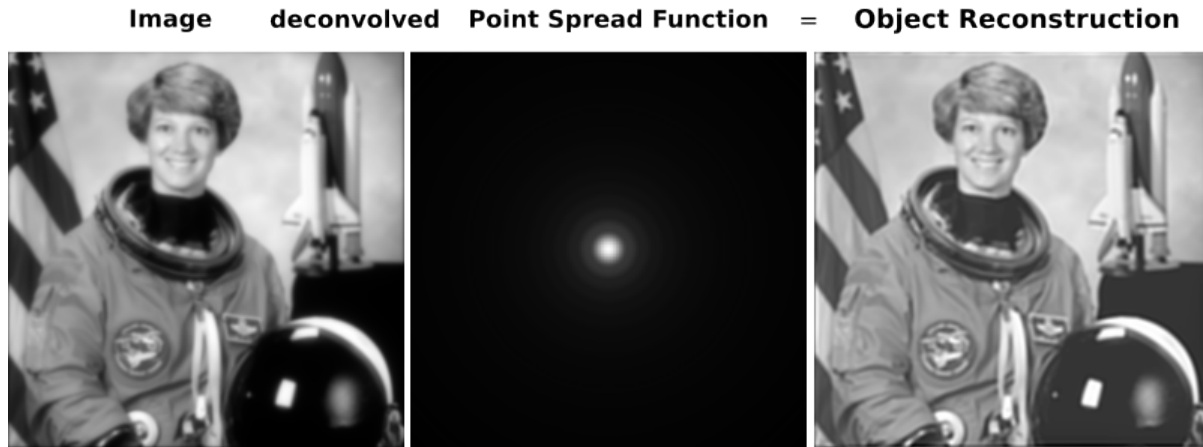


**Figure 3.6:** Deconvolution of the blurred image to reconstruct the original data using the Wiener deconvolution methods provided by scikit-image.<sup>73</sup>

to suppress the noise in the reconstruction of the signal as defined in equation 3.16:

$$F(u, v) = \frac{G(u, v)}{H(u, v)} \left[ \frac{1}{1 + \frac{(NSR(u, v))}{\|H(u, v)\|^2}} \right] \quad (3.16)$$

Similar deconvolution methods can also be applied for stray light correction for a wide range of applications.<sup>77 78</sup> Figure 3.6 shows exemplary the Wiener deconvolution to reconstruct the object. State-of-the-art spectrometer like TROPOMI use the Van Cittert deconvolution.<sup>64</sup> In these methods, the stray light is considered as an extension of the dynamic range and spatial coverage of the PSF over the detector. Such an extended PSF is also known as a stray light kernel and is widely used for stray light assessment and correction.

### 3.7 IN-FIELD STRAY LIGHT AND GHOSTING

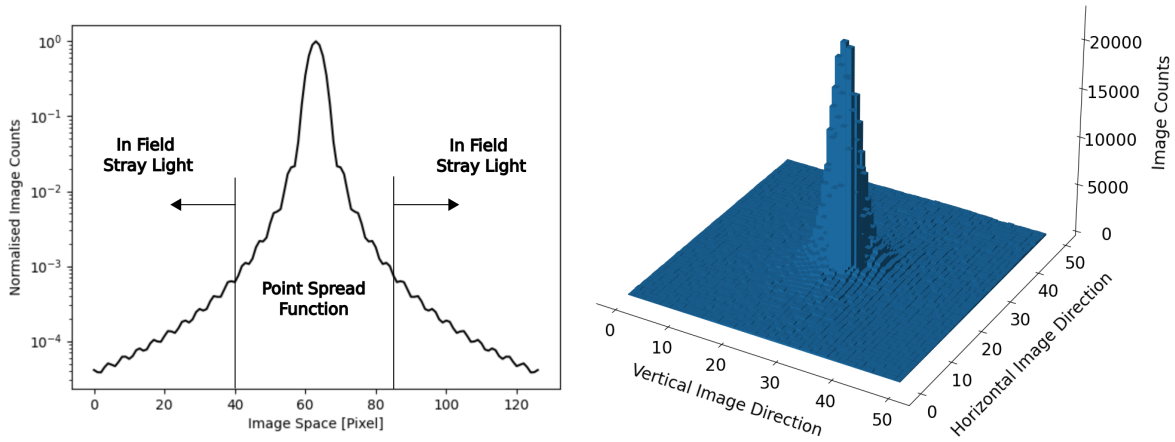
In-field stray light refers to multiple light scattering artefacts within an optical system that are caused by a light source visible within the FOV, resulting in unwanted radiance on the image detector. It can be an effect of surface reflection, surface scattering or aperture diffraction.<sup>57</sup> In practice, in-field stray light is typically measured as the ratio between the power of the stray light and the power of the nominal signal. The boundaries between the two are typically given by spatial resolutions, source boundaries, or mission requirements.<sup>64 58</sup> Figure 3.7 shows the cross section of a normalised airy disk

image in logarithmic scale. For an imaging system with a circular pupil, the diffraction-limited PSF is represented by a series of concentric rings known as an Airy disk. The exact definition of the boundary between the PSF and the stray light is arbitrary. Changing the definition of the size of this region will affect the apparent stray light in the instrument. Therefore, definitions must be carefully considered and disclosed when stray light performance is specified.<sup>58</sup> One way of determining the distance to the signal is using multiples of full width at half maximum (FWHM) of the PSF.<sup>64</sup>

Stray light kernels for simple imaging systems assume a constant level of stray light across the FOV, which is valid for in-field stray light that is distributed homogeneously across the detector. This is typically the case due to dust contamination scattering. To comprehensively characterize an incoherent instrument's response to stray light, it is necessary to determine the relative stray light response, also known as the Stray-Light Distribution Function (SDF)  $d_{i,J}$  for each excitation array element  $J$  on all detecting pixels  $i$ .<sup>79</sup>

$$D = \begin{bmatrix} d_{1,1} & d_{1,2} & \dots & d_{1,J} & \dots & d_{1,n-1} & d_{1,n} \\ d_{2,1} & d_{2,1} & \dots & d_{2,J} & \dots & d_{2,n-1} & d_{2,n} \\ \dots & \dots & & \dots & & \dots & \dots \\ d_{i,1} & d_{i,1} & \dots & d_{i,J} & \dots & d_{i,n-1} & d_{i,n} \\ \dots & \dots & & \dots & & \dots & \dots \\ d_{n-1,1} & d_{1,2} & \dots & d_{n-1,J} & \dots & d_{n-1,n-1} & d_{n-1,n} \\ d_{n,1} & d_{n,1} & \dots & d_{n,J} & \dots & d_{n,n-1} & d_{n,n} \end{bmatrix} \quad (3.17)$$

Since  $d_{i,J}$  varies with both the excitation element  $J$  and the detection element  $i$ , measuring the SDF for each element in the array is impractical for high resolution detectors. The result is a Stray Light Distribution Function Matrix  $D$  (see equation 3.17<sup>79</sup>), where the total number of elements is equal to the number of detector pixels squared. Even for a small detector area of 100x100 pixels used, the resulting matrix contains 1.46 trillion elements. However, since the shape of  $d_{i,J}$  typically changes smoothly across the array with excitation element  $J$ , the  $d_{i,J}$  can be measured at intervals much larger than the detector element interval, and the  $d_{i,J}$  for  $J$  between the measured excitation elements can be



**Figure 3.7:** Left: Cross section of an Airy disk showing diffraction pattern resulting from circular aperture. Right: Measured Point Spread Function from a LED behind a 25  $\mu\text{m}$  pinhole.

obtained by interpolation.

To achieve comparability between instruments and to meet design requirements, it is necessary to derive a one-dimensional in-field stray light quantity from  $D$ . Such a quantity is not clearly defined in the standard literature, so a definition similar to that used by TROPOMI<sup>64</sup> and EnMAP<sup>58</sup> is applied. These are based on PSF measurements with extended dynamic range and spatial coverage. Figure 3.8 explains how the peak position of the PSF is used to define a signal and a background area around the PSF. This spatial separation assumes that stray light locally incident on signal pixels is part of the signal, which cannot be assumed for stray light artefacts leading to interference from ghosts. The signal and background distances can be defined in both directions, as a PSF extension can vary strongly in different image directions. For the simple symmetric case the Background Stray Light (BSL) is defined by equation 3.18 where  $a_{\text{signal}}$  and  $b_{\text{signal}}$  defines the rectangular signal boundaries in vertical and horizontal image direction.  $a_{\text{background}}$  and  $b_{\text{background}}$  define the boundaries where stray light is evaluated. Due to the different number of pixels used in the ratio, all detector noise effects must be subtracted for this analysis. When surveying large detectors based on point light sources, where the entire pixel noise cannot be reduced through dark image subtraction, the background must be chosen so that stray light can still be distinguished from detector noise. Assuming that the stray light to noise level is sufficient for the entire detector, the Total In-Field Stray Light (TIFSL) is given by

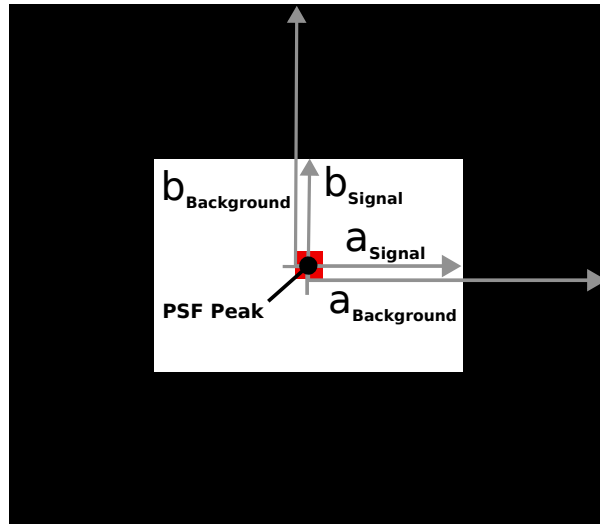


**Figure 3.8:** To compare stray light quantities for point source measurement, boundaries between signal stray light must be defined around the PSF peak to evaluate the Background Stray Light (BSL).

equation 3.19. To make the limits of the background and the PSF more comparative between instruments, the FWHM of the PSF can be used as a scaling value. Particularly with extended light sources, the total signal power is sufficient to allow TIFSL to be used as a theoretical general case.

$$BSL(a_{Signal}, a_{Background}) = \frac{\sum_0^{a_{Background}} J}{\sum_0^{a_{Signal}} i} \quad (3.18)$$

$$TIFSL(a_{Signal}, a_{Detector}) = \frac{\sum_0^{a_{Detector}} J}{\sum_0^{a_{Signal}} i} \quad (3.19)$$

Ghost reflection are another in-field stray light artefact that is caused by reflection from lenses or any other refractive surface like the diffraction gratings or the detector surface. These artifacts, also known as lens flare in photography, can also occur with the light source outside the FOV with strong light sources. However, for most instruments with an optical baffle, these effects can only be seen close to the FOV. The number of refracting surfaces  $n$  is quadratic in the number of possible ghost images  $\Phi$ :<sup>57</sup>

$$\Phi = \frac{1}{2}(n^2 - n) \quad (3.20)$$

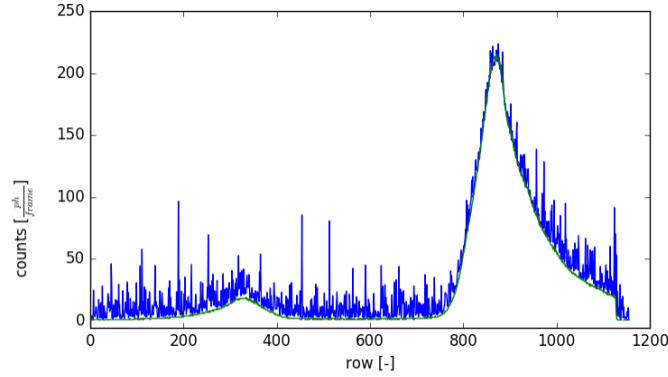


**Figure 3.9:** Ghost seen with the AtmoSHINE instrument at detector pixel row 350 reflected from the airglow signal at row 900. Upon examination of a series of images, it becomes evident that the second maximum is mirrored along the horizontal centre axis. The green line represents the mean row value and the blue line maximum value in this row.

This equation illustrates why the number of optical elements is kept to a minimum for stray light reasons. In particular, plane-parallel surfaces relative to the optical axis can produce strong ghosting effects. Such a strong ghost was visible in the AtmoSHINE instrument, causing a reflection of the airglow peak emission to other detector areas. This was caused by a plane-parallel integrated band-pass filter. Since about 50% of the power entering the instrument is reflected by the SHI, the reflected wavefront at the bandpass filter created a strong ghost of about 10% of the measurement signal mirrored on the central horizontal image axis. Figure 3.9 shows the mean counts in horizontal direction of the AtmoSHINE data already introduced in figure 2.4. In the development of successor instruments, this ghost artifact was eliminated by slightly tilting the bandpass filter by one deg. Due to the angular dependence of the ghost, such reflections cannot be corrected with an averaged stray light kernel. Each field angle has its own ghost shape, position and intensity.

To detect angle-dependent stray light in optical systems, the stray light kernel is measured for individual angular ranges using automated stages for the instrument or the light source.<sup>80 81 58</sup> Similar measurements can also be performed on satellites by scanning an isolated star over the entire FOV.<sup>82</sup> Given a PSF dataset with high angular resolution and high dynamic range, ghost artefacts can be corrected by deconvolution with very large kernels.<sup>83 84</sup> The latest experimental methods even allow the propagation of ghost reflections from lenses within an optical system to be measured directly using time-of-flight imaging with streak cameras.<sup>85</sup>

However, all these methods apply to incoherent stray light, where the phase of the measured light does not provide any further information about the observed scene. Energy within the FOV can be spatially shifted to other positions without taking into account possible interference.

### 3.8 SPECTRAL STRAY LIGHT

Spectral resolving instruments, such as the ISHI, may experience interference from stray light, resulting in spectral stray light. For the Michelson interferometer, parasitic interference causes spectral stray light due to interference from ghost artefacts caused by light reflected from optical surfaces or the detector.<sup>86</sup> Another reported cause is piston, the mean value of a wavefront or a phase profile through the pupil of an optical system.<sup>87</sup> Such parasitic interference has also been reported for state-of-the-art limb sounding instruments based on partially scanned interferograms<sup>88</sup> or static Fourier transform spectrometer<sup>89</sup> designs. After intensive research, no publications on a correction method of parasitic interference could be found for similar instruments and wavelength. However, the theoretical foundations can be transferred from the deconvolution of interference in interferometric radio signals<sup>90</sup> or holographic microscopes<sup>91</sup>. With conventional spectrometers, the stray light between different wavelengths can be measured and corrected in post-processing with relatively simple means as spatial and spectral information are not overlapping in 2D space. This allows to measure the crosstalk between different spectral lines<sup>60</sup> and therefore to correct the spectral and spatial stray light of instruments like EnMAP<sup>58</sup> or TROPOMI.<sup>64</sup> A rather novel method to significantly reduce the spectral stray light in the spectrometer design is by Periodic Shadowing. The spectrometer captures images of a Ronchi ruling target, as shown in figure 3.10, mounted on the intermediate image at the entrance slit of the instrument. This consists of evenly spaced, opaque stripes. Such a technique creates shadowed image regions throughout the FOV that are blocked from incident light. By continuously capturing this shadowed image area, a stray light measurement is provided for every image. Subtracting the stray light signal from the corresponding signal can reduce the signal-to-noise ratio by two orders of magnitude.<sup>92</sup>

Since the ISIS system derives its spectral information from a Fourier transform of the interfero-

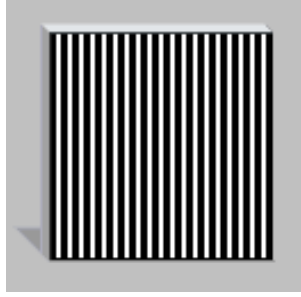


**Figure 3.10:** A Ronchi ruling, Ronchi grating or Ronchi mask is a specific type of optical target or mask that employs a constant-interval bar and space square-wave pattern. Created by BorkaGoose. CC BY-SA 3.0

grams, it is important to know whether the stray light is homogeneously distributed across the detector or produces artefacts with high frequency components. The Fourier transform used by the data retrieval separates the unmodulated signal from the modulated signal. For example, direct sunlight on satellite-based systems is unmodulated because this light is not subject to spectral modulation by atmospheric absorption bands. Direct sunlight is therefore represented by the transmission spectrum of the bandpass filter and can therefore be easily separated from the airglow emission spectrum. Figure 3.11 shows a typical laboratory calibration measurement using a narrow band laser source to generate an ideal interferogram. A key issue for data retrieval and measurement error is the extent to which stray light leads to interference or not. As can be seen from previous definitions, the signal-to-noise ratio (SNR) of the instrument is directly proportional to the signal visibility  $V_{Signal}$ .<sup>6</sup> Considering the effective signal as  $S_{Signal}$ ,  $S_{SLIF}$  as the stray light signal in-field and  $S_{SLOF}$  as the stray light signal contributing out-of-field we can define the total signal as can be seen in equation 3.21.

$$S_{Total} = S_{Signal} + S_{SLIF} + S_{SLOF} \quad (3.21)$$

Assuming that the signal terms are independent, equation 3.21 can be converted into equation 3.23 as a multiplication of Visibility  $V$  and number of photons of the individual source  $N$ , by using equation 3.22. The variations in the visibility of the out-of-field stray light sources can be explained by the change in the wavefront when light is scattered by the vanes or other parts of the instruments as has been simulated in ZEMAX.<sup>6</sup> Variations in in-field stray light visibility can be caused by different optical path lengths of the ghost artefacts, as will be shown in the measurements and analysis.

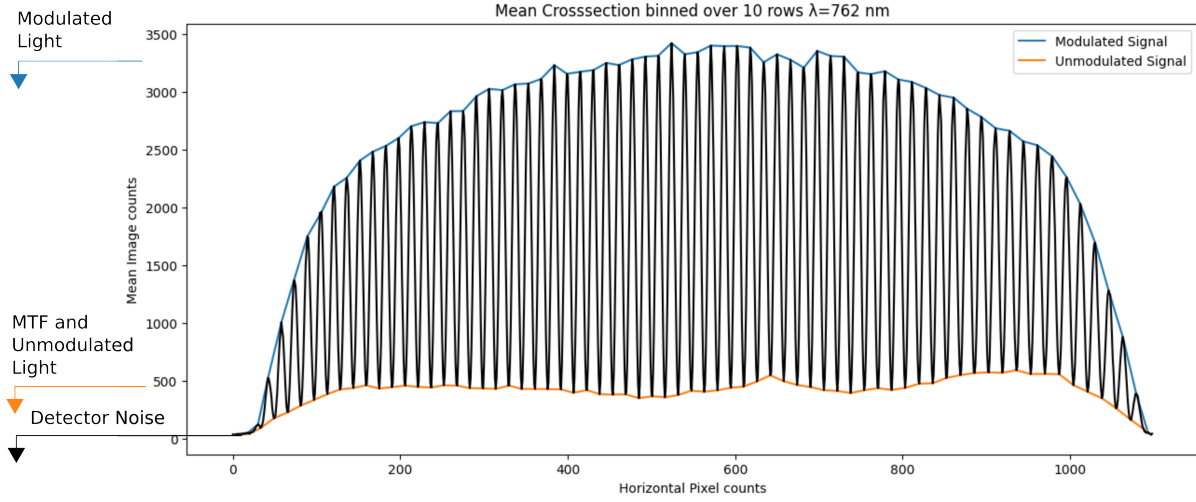


**Figure 3.11:** Depending on the spectrum of observed light source the intensity contributes to the interference or to a constant signal offset. Dark image correction almost entirely eliminates the constant noise floor. High-frequency modulation that cannot be resolved by the instrument MTF also contributes to the unmodulated signal.

$$S = V \cdot N \quad (3.22)$$

$$S_{Total} = V_{Signal} \cdot N_{Signal} + V_{SLIF} \cdot N_{SLIF} + V_{SLOF} \cdot N_{SLOF} \quad (3.23)$$

To determine the measurement error caused by stray light, the correlation between the individual terms is critical and an important result of the following measurements. Only when considering the retrieval process and corrections for 2D in-field and out-of-field stray light distribution, the final measurement error due to stray light can be determined. In order to roughly estimate the influence of different stray light artefacts on the instrument measurement signal, we therefore define the Interfering Stray Light to Signal Ratio (ISR):

$$ISR = \frac{S_{SLIF} + S_{SLOF}}{S_{Signal}} = \frac{V_{SLIF} \cdot N_{SLIF} + V_{SLOF} \cdot N_{SLOF}}{V_{Signal} \cdot N_{Signal}} \quad (3.24)$$

### 3.9 OUT-OF-FIELD STRAY LIGHT

Out-of-Field Stray Light is caused by light sources outside the FOV. Light sources become visible due to scattering from the first optical elements, even if they are not in the nominal FOV of the

instrument. To make out-of-field stray light comparable between different instruments, the Point Source Transmittance (PST) is used as a measure. The term can be traced back to the year 1977.<sup>93</sup> Several definitions have been used, but the most common is: The ratio of the irradiance incident on the detector  $E_{SL}$  to the irradiance incident on the entrance aperture  $E_{inc}$  as seen in equation 3.25:<sup>57</sup>

$$PST_{(\theta_{source})} = \frac{E_{SL}}{E_{inc}} \quad (3.25)$$

Figure 3.12 illustrates this definition. The optical system is aligned at the incident angle  $\theta_{source}$  relative to a light source with the projected solid angle  $\Omega_{source}$ , the atmospheric transmittance  $\tau_{atm}$  and apparent radiance  $L_{Source}$ . By given transmittance  $\tau_{optics}$  and a solid angle of the optics  $\Omega_{optics}$  equation 3.26 can be simplified to:

$$PST_{(\theta_{source})} = BSDF_{optics(\theta_{source})} \cdot \Omega_{optics} \cdot \tau_{optics} \quad (3.26)$$

By a given Bidirectional Scattering Distribution Function (BSDF), a common and well-defined way of describing the scattering properties of surfaces, the out-of-field properties of an optic can be estimated. The out-of-field stray light characteristics of a optical system without baffle can be simply determined by BSDF of the first optical surface.<sup>94</sup> This highlights the critical nature of the contamination and surface quality of this optical element. The incidence irradiance  $E_{inc}$  at the instrument first aperture of a source of radiance  $L$ , size  $A$  and distance  $d$  is defined by the equation 3.27<sup>57</sup>.

$$E_{inc} = \frac{LA \cos^4(\theta_{source})}{d^2} \quad (3.27)$$

To reduce the out-of-field irradiance of the first optical surface, an optical baffle is a standard component used in most space optics and earth observation instruments. Especially for limb sounders the baffle design plays a fundamental role, as weak in-field signal levels must be isolated from strong reflections of clouds and the earth surface. Therefore, larger limb sounding instruments for O<sub>2</sub>-A band observations like MATS use a baffle length of 650 mm.<sup>95</sup> The resulting high aspect ratio of the instrument makes integration more challenging for smaller satellites. For SHIPAS QM instrument a

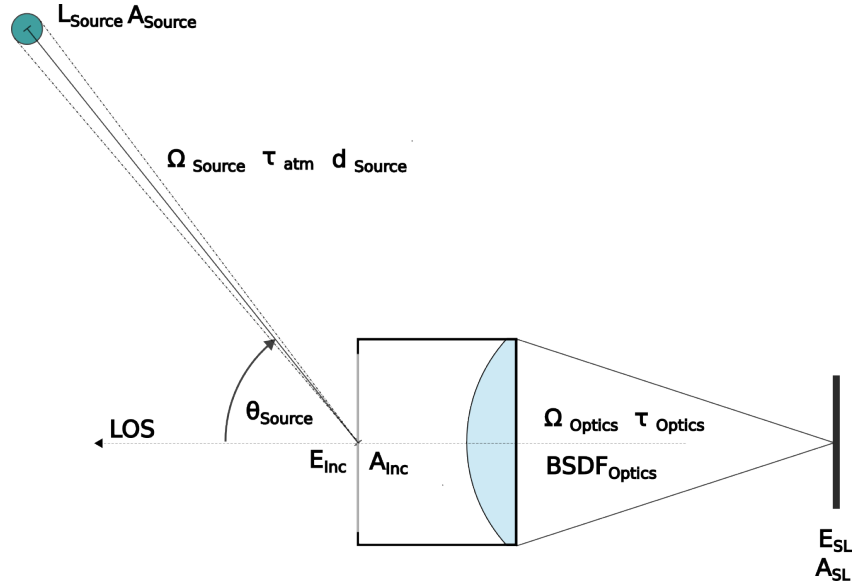


**Figure 3.12:** A sketch of the basic quantities used to evaluate the Point Source Transmittance (PST). The angle  $\theta_{source}$  defines the angle between the LOS and sight vector of a light source.

tradeoff between baffle length and size has been chosen. Table 3.3 lists the relevant baffle dimensions.

Figure 3.13 illustrates the basic baffle geometries that lead to equations 3.28 and 3.29.

**Table 3.3:** SHIPAS QM baffle specification.

Baffle Length - L	235 mm
Baffle Aperture - D	86 mm
Filter Aperture - d	80 mm
Sun Exclusion Angle Full Cone - $\theta_{sun\ exclusion\ angle}$	39.0 deg
Max Field-of-View Full Cone - $\alpha_{max}$	1.56 deg

$$\alpha_{max} = \tan^{-1} \left( \frac{D - d}{2L} \right) \quad (3.28)$$

$$\theta_{sun\ exclusion\ angle} = \tan^{-1} \left( \frac{D + d}{2L} \right) \quad (3.29)$$

When designing baffles, it is crucial to ensure that there is no vignetting caused by the baffle. Therefore, the aperture of the baffle needs to be large enough so that the light cone defined by the FOV does not intersect with any baffle vanes.  $\alpha_{max}$  defines the maximum possible FOV and the relation to the aperture dimensions of the baffle. The sun exclusion angle for SHIPAS QM is equal to  $\theta_{sun\ exclusion\ angle}$  and indicates the minimum angle to the line-of-sight (LOS) at which the amount

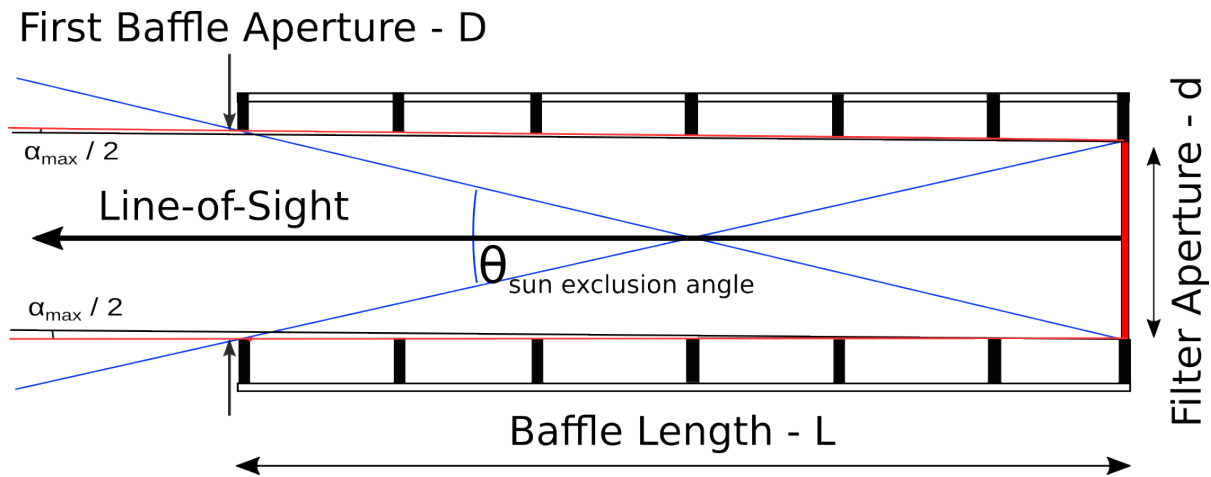


**Figure 3.13:** The angle  $\theta_{sun\ exclusion\ angle}$  defines the largest angle at which a light beam still reaches the first optical surface (for SHIPAS QM the band-pass filter).

of stray light caused by direct sunlight should theoretically be acceptable. The practical stray light limited sun exclusion angle may be different from  $\theta_{sun\ exclusion\ angle}$  and must be determined by measurement, as scattering from the vanes may still be relevant. To determine the effectiveness of the baffle on the PST reduction, the percentage overlap between the entrance aperture of the baffle and the surface of the first optical element is determined. This function is called the shadow function  $SF$ . It provides the percentage of a light cone entering the baffle that illuminates the first optical surface as a function of the angle of incidence  $\theta_{source}$ .<sup>57</sup>

### 3.10 STRAY LIGHT ESTIMATIONS AND SIMULATIONS

Since stray light has a decisive influence on the measurement error and the spatial resolution of an optical system, an initial evaluation is already carried out with the aid of simulation during the design phase of optics. This enables early identification of critical surfaces and design choices that affect stray light. Such simulations have been performed for the revised optical design used for the INSPIRESat3, INSPIRESat4 and SHIPAS mission. Based on the CAD data of the INSPIRESat 4 optomechanics and the optical design file from ZEMAX, a stray light simulation was build using the an non-sequential ray tracing software ASAP.<sup>96</sup> This simulation includes the beam splitter and both diffraction gratings. The detector reflectivity of 30% was assumed to be homogeneous and specular

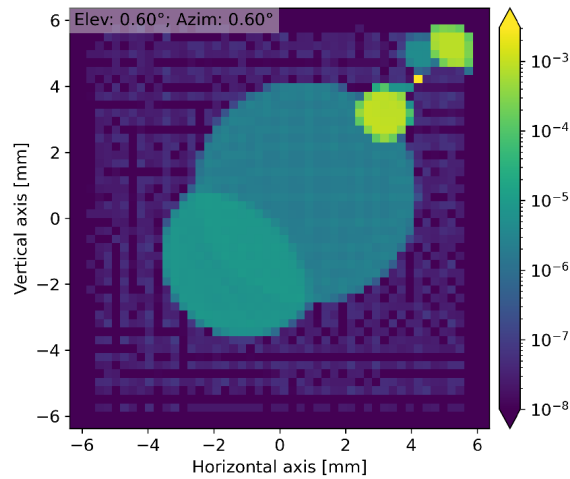


**Figure 3.14:** Simulated ghosts up to 5<sup>th</sup> order caused by a point source at 0.6 degrees vertically and 0.6 degrees horizontally in the FOV, indicated by a yellow pixel. Credit goes to Martin Kaufmann and Konstantin Ntokas for the creation of this illustration.<sup>96</sup>

over the entire surface. Since interference is not taken into account in this simulation, statements can only be made about intensity distributions from a broad band light source and not about parasitic interferograms caused by stray light of modulated light.

**Table 3.4:** Optical quantities to derive relative ghost irradiance caused by reflections between detector and diffraction grating. The values are based on information provided by the component manufacturers.

Detector External Quantum Efficiency - EQE	70%
Detector Reflectivity - R	30%
Beamsplitter Ratio - BR	50%
Diffraction Gratings 1 <sup>th</sup> Order Efficiency - $\eta$	70 %

The ASAP simulations predicted a first order ghost with a peak irradiance of about 7% of the nominal light. This is the only ghost focused on the sensor. Its light path is predicted as the nominal path, so the ghost represents quasi-nominal light. This artefact is caused by an optical cavity created between the detector and the two diffraction gratings and is inherent to the SHI design. All simulated ghost artifacts account for 8.6% of the irradiance of the nominal light, making it the largest contributor to the TIFSL of 9.37%. Table 3.4 shows the essential optical quantities to derive the stray light irradiance of the first order ghost. The algebraic estimation of the ghost stray light (GSL) by simple ray tracing, as shown in Figure 3.15, gives a comparable solution to the numerical simulation in-field, as can be seen from the equations 3.31 and 3.30, assuming that all other optics are fully transparent:

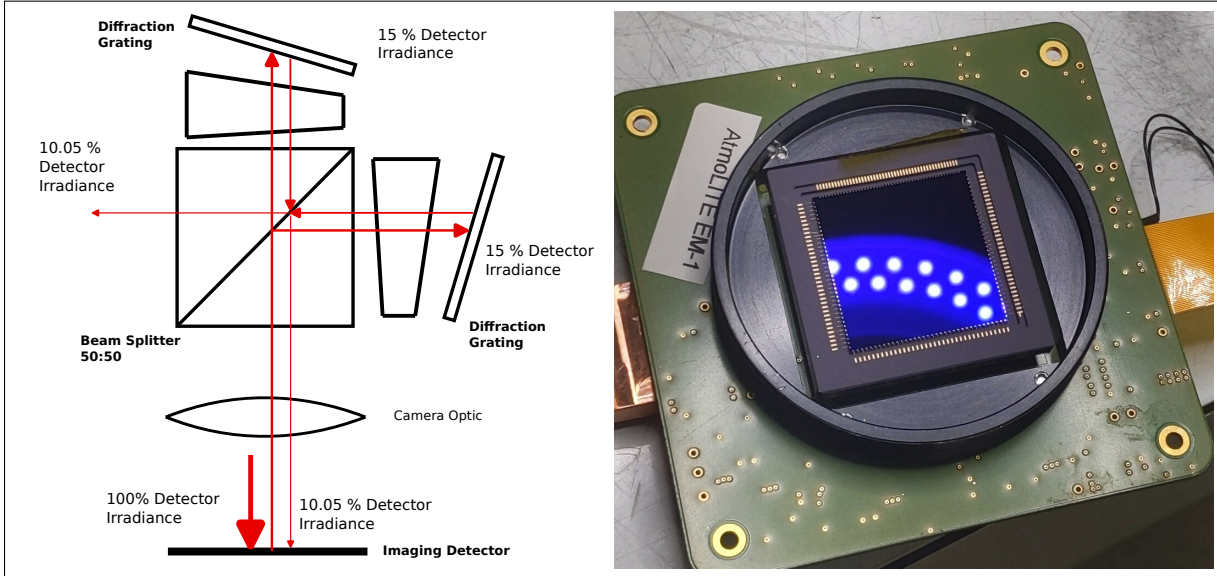


**Figure 3.15:** Left: The analytical model of the ghost artifact can be derived by simply ray tracing the irradiance of the detector reflected back into the instrument. Right: Blue LEDs of a laboratory lamp show a specular reflection on the detector surface.

$$EQE + R = 1 \quad (3.30)$$

$$GSL_{1^{th} Ghost} = \frac{E_{1^{th} Ghost}}{E_{detector}} = \frac{E_{detector} \cdot R \cdot BR \cdot \eta}{E_{detector}} = R \cdot BR \cdot \eta = 10.5\% \quad (3.31)$$

If we assume that 30% of the incidence power is reflected back, then this power hits the diffraction grating in equal proportions after the beam splitter. Due to the diffraction efficiency  $\eta$ , 70% is reflected back. Of this, 50% leaves the instrument on the return path due to the beamsplitter ratio  $BR$ , the other 50% results in a 10.5% irradiance of the ghost relative to the nominal detector irradiance. The difference between numerical simulation and algebraic estimation can be explained by the absence of EQE modelling for the algebraic signal estimation. The same equation for the second order ghost gives a GSL of 1.1%, while the numerical simulation with ASAP gives a value of 0.4%. Figure 3.14 shows the ghost irradiance up to order 5<sup>th</sup> for a field angle of 0.6 deg vertical and 0.6 deg horizontal.

Studies have shown that, depending on the wavelength, the detector behaves like a diffraction grating and reflects power in different directions based on the incidence angle and grating order.<sup>97</sup> Small experiments confirmed the detector's inhomogeneous and angle-dependent behaviour. How-

ever, methods and experimental setups to precisely quantify this behaviour are lacking. Figure 3.15 illustrates how blue LEDs are specularly reflected on the detector, resulting in a sharp image of the light sources. The assumption that the diffraction gratings reflect only in certain orders is also an oversimplification. A study of various diffraction gratings, including the ruled gratings from the same manufacturer used in the ISHI, shows the amount of stray light compared to other lithographic or holographic types.<sup>98</sup> While holographic gratings typically have lower stray light than early ruled gratings, modern control systems and improved master coatings have made it possible to produce ruled gratings with replicas that have as little stray light as holographic gratings.<sup>99</sup> For this reason, special low-level stray light gratings are used in earth observation applications such as TROPOMI<sup>100</sup>, which are available from several manufacturers.

Assuming a particle concentration of 300 ppm, ASAP simulations show that under these conditions up to 0.7% of the nominal light ends up as in-field stray light due to scattering on particles. Out-of-field stray light simulations were also conducted. However, due to the significantly longer baffle for the SHIPAS mission, the ray tracing simulations are no longer comparable with the measured instrument stray light characteristics. For this reason, analytical model runs similar to those performed for the AtmoSHINE mission were done, but with new parameters for the baffle length. Equation 3.32 provides the function for determining the PST dependence on incident angle as can be seen in 3.16. This function takes into account the shadow function  $SF$ , estimated scattering characteristics from the bandpass filter surface roughness  $BPDF_{roughness\ filter}$  assuming a typical surface RMS roughness value of 10 Angstroms, and bandpass filter contamination  $BPDF_{contamination\ filter}$  based on a cleanliness level of 500 and a percent area coverage of 0.316%. Using the Harvey model for contamination and the Harvey-Shack model for surface roughness gives the BSDF respectively.<sup>157</sup>

$$PST_{(\theta_{source})} = SF \cdot (BPDF_{roughness\ filter} + BPDF_{contamination\ filter}) \quad (3.32)$$

As mentioned in chapter 3.8, the modulation of incoming stray light is crucial in its effect on the measurement signal. Figure 3.17 illustrates the two simulations. The first is a radiative transfer simulation of the sunlight spectrum scattered at various angles relative to the LOS of the limb sounding

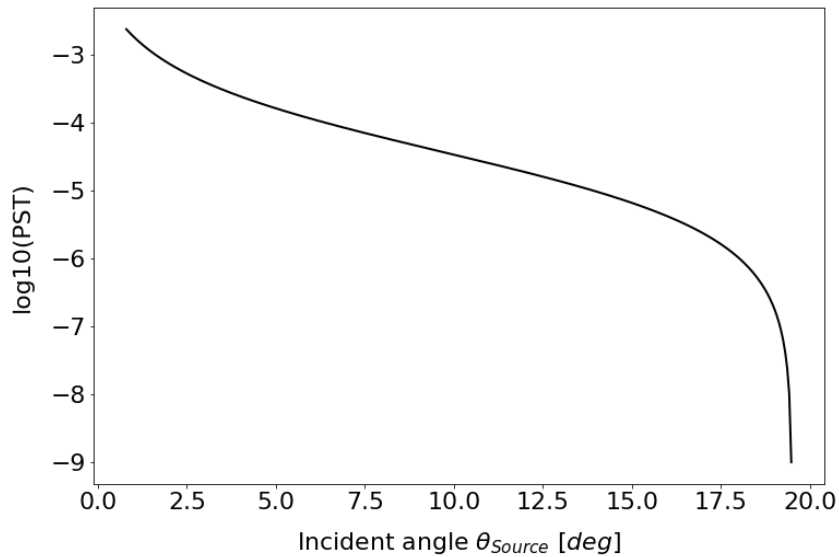


**Figure 3.16:** The PST (Point Source Transmittance) calculation is based on the shadow function and surface scattering at the bandpass filter. Out-of-field stray light near the FOV is primarily caused by the scattering of the first optical element. For higher incident angle the shadow function determines the PST progression until the sun exclusion half cone angle  $\theta_{sun}/2 = 19.5 \text{ deg}$  is reached. For larger angles, only reflections at the baffle vanes will reach the bandpass filter.

instrument. The second is the normalized emission spectrum targeted by the instrument. Light scattered towards the instrument from lower altitudes shows strong modulation and radiance starting at about 1.4 deg with the beginning of the troposphere. Sunlight scattered at the atmosphere at an angle of 1.0 degree relative to the LOS is still low in terms of irradiance and modulation. A comparison of the radiative transfer spectrum with the emission spectrum shows that the two spectra are almost inversely related, as would be expected. If this inversely modulated out-of-field scattered light from lower altitudes causes an interferogram, it will reduce the modulation of the O<sub>2</sub> A-band signal and thus directly affect the measurement signal. ”Therefore, the observed daytime emission spectrum is actually sitting in an absorption well, and simply subtracting a linear background would distort the A-band emission spectrum and so underestimate the intensity of the true dayglow emission.”<sup>18</sup> For the MIGHTI instrument only very simplified stray light simulations have been published without mentioning the ghost between the detector and the gratings. Simulations only cover out-of-field stray light, which is specified as < 10% of the average daytime oxygen red line emission signal peak at 630 nm. In-field stray light or the effect of parasitic interference is not mentioned for any MIGHTI band.<sup>43</sup>

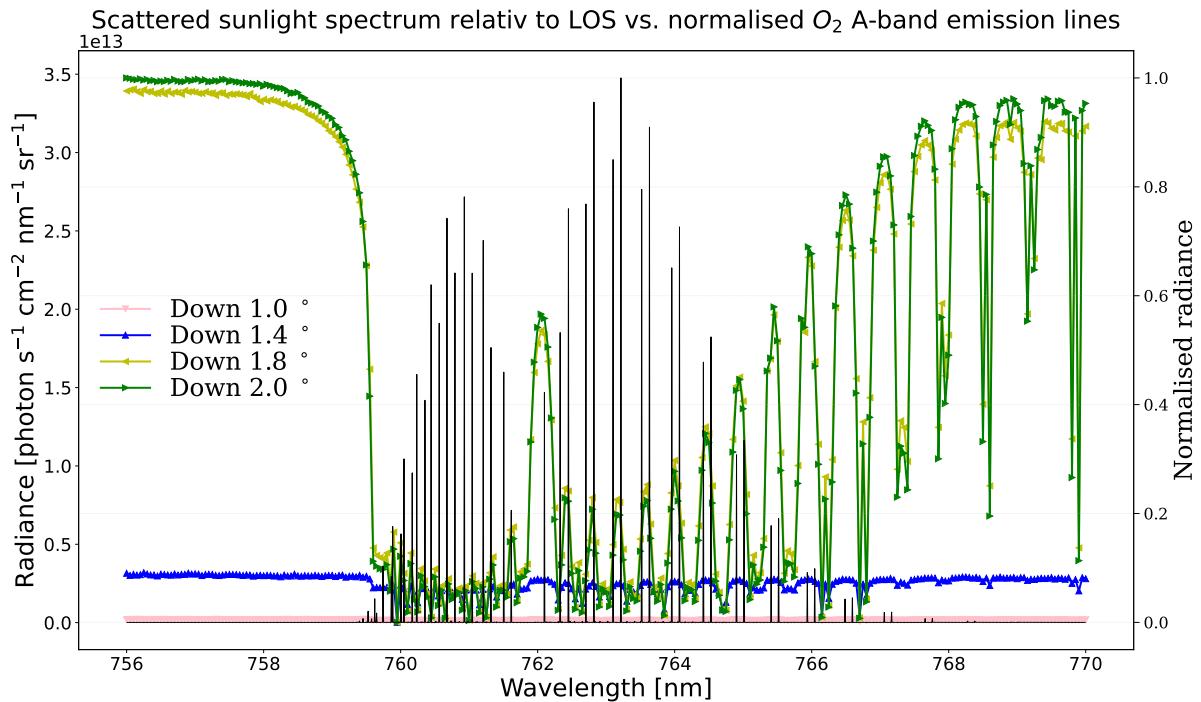


**Figure 3.17:** The modulation of out-of-field stray light scattered at the lower atmosphere increases toward lower altitudes from the perspective of the limb sounder. The absorption lines have the inverse spectrum of the  $O_2$  A-band emission lines. Radiative transfer simulation are performed with libradtran<sup>101</sup> and configured by Qiuyu Chen.  $O_2$  A-band emission are simulated with Radis<sup>21</sup>

### 3.11 IN-ORBIT VALIDATION

”Test as You Fly, Fly as You Test, and Demonstrate Margin”. This principle requires that ground tests and simulations accurately reflect the planned mission profile, including margin, appropriate off-design parameters and environmental conditions like vacuum and temperature profiles.<sup>102</sup> It also reflects the central role of tests within the developments process. Without the ability to continuously test system requirements as part of the design process and operation, the quality of derived measurement data cannot be validated. For the development of laboratory calibration experiments, this means that only parameters that can be replicated in orbit can also be validated in-orbit. Otherwise, there is a risk that launch-induced impact to the instruments, as well as space conditions that have not been replicated in the laboratory, will affect the performance of the instrument in unknown ways. As the instrument operates, the ground test bench will be continuously improved to reduce the gap between hardware replicas, instrument simulations and in-orbit measurements.<sup>103</sup> In order to detect long-term decay and drift effects of the instrument in-orbit, the validation measurements are repeated

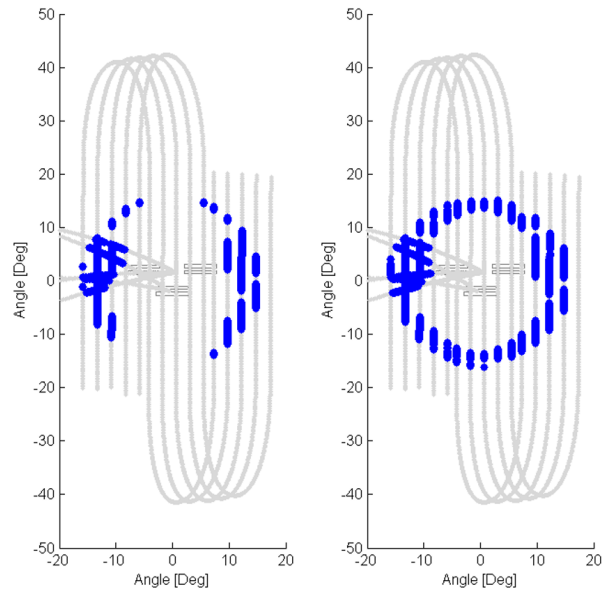


**Figure 3.18:** Illustration of the moon position relative to the Landsat Thermal Infrared Sensor during the special lunar scans and Earth-to-Moon slews. Moon positions where ghost are detected are highlighted in blue for Band 10 (left) and Band 11 (right).<sup>108</sup>  
 Author: Matthew Montanaro Image License: CC BY 3.0 DEED

continuously. These include radiometric calibration and stability, which is regularly validated using on-board calibration lamps<sup>104</sup>, sunlight scattering diffusers<sup>105</sup> or the Moon<sup>106</sup> as a calibration target. For MIGHTI spectral calibration in orbit, a neon and a krypton lamp are installed on the satellite.<sup>107</sup> As the aim of the SHIPAS mission and the INSPIRESat missions is to test highly miniaturised SHI, no on-board calibration lamps or solar diffusers are available. As no absolute radiometric calibration is required for the measurement method used, this simplifies the in-orbit validation.

In addition to the radiometric and spectral characteristics, the spatial and stray light instrument characteristics must be validated in orbit. The lack of an atmosphere and the long-term stability of the moon surface make it an ideal target for calibration and cross-referencing between different satellite instruments. Sunlight scattered on the moon surface provides sufficient irradiance over a broad spectrum to obtain a sufficient signal-to-noise ratio with sufficiently short integration time. Especially for the validation and analysis of stray light artefacts, moon observations offer ideal conditions for the analysis of in-field and out-of-field stray light properties as well as ghosts.<sup>108</sup> Figure 3.18 outlines a moon scan manoeuvre performed by the Landsat 8 thermal infrared sensor relative to the instrument's LOS and the ghost artefacts identified for several out-of-field angles.

The moon disc is frequently employed to ascertain the spatial resolution of telescope optics. In the absence of an atmosphere, the limb of the surface exhibits a high contrast to deep space. This measurement is referred to as the Lunar Limb Knife-Edge<sup>109</sup>. It is analogous to the standardised MTF Knife-Edge measurement, which is employed for a multitude of optical systems.<sup>110</sup> It can be readily replicated in a laboratory setting. For this reason, several satellite instruments use the moon limb as a method of validating the MTF of a satellite instrument in orbit.<sup>111 112 113 114 115 116</sup> Particularly for imaging limb sounding instruments, this provides an alternative to ground-based MTF targets that are regularly overflowed by nadir-viewing instruments.

### 3.12 SIMULATION OF ORBITS AND LINE-OF-SIGHT

In addition to spatial resolution, the precise alignment of the instrument LOS (Line-of-Sight) and the associated validation strategy are required to transform the data to an Earth-fixed coordinate system. As there are no visible ground control points for a limb sounding instruments, only stellar objects can be used to validate and correct the LOS. Moon observation has proven to be particularly suitable here.<sup>117</sup> To prepare for observations with the given narrow FOV, it is necessary to estimate the LOS with  $\pm 0.7$  deg within the Satellite Attitude Control. To provide a reference for optical integration of the instrument a cubic mirror mounted on the instrument housing is referenced to the LOS as part of the instrument calibration.<sup>6</sup> This mirror is used to provide the transformation matrix between the star tracker LOS and the instrument LOS. The instrument data can now be transformed into the attitude control coordinate system of the satellite. The LVLH (Local Vertical, Local Horizontal) is the default reference frame for many spacecraft simulations. It is a rotating reference frame that is described by the vector between the center of gravity pointing to earth center  $Z_{LVLH}$  and the negative orbit normal vector  $Y_{LVLH}$ . Taking the cross product between both vector gives  $X_{LVLH}$ . Knowing the LOS orientation and the satellite's position in LVLH over time allows for a statistical determination of the impact of the Sun and Moon on the out-of-field stray light throughout the mission.

Figure 3.19 sketched the different coordinate systems and the transformations between them. The star tracker references the satellite's attitude to stars that have been measured by astronomers to

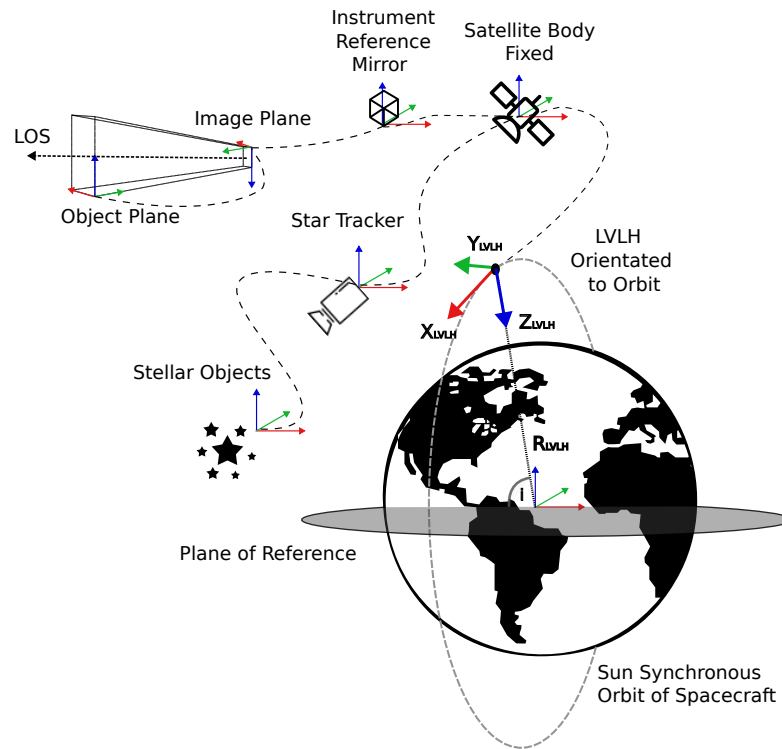


**Figure 3.19:** Describes the coordinate systems relevant to the limb sounder measurement, the interdependencies between them, and their relationship to sun-synchronous orbit. The orbit inclination is given by the angle between the orbit plane and the Earth's plane of reference given by the cross section of the equator. The LVLH (Local Vertical, Local Horizontal) coordinate system connects the satellite body frame with respect to the Earth fixed coordinate system. Without accurate and precise knowledge of the transformation between each coordinate system, measurement data cannot be transformed to Earth coordinates.

a high degree of accuracy. To validate and subsequently correct the LOS vector with respect to the LVLH coordinate system, it is necessary to simulate the orbit data and coordinate systems shown here in advance and plan the instrument alignment with the satellite operator based on these estimated values. The Python library Skyfield<sup>68</sup> provides interfaces to SPICE, the Observation Geometry Information System to help NASA's scientists plan and interpret scientific observations from space-based instruments on board robotic planetary spacecrafts.<sup>118</sup> Skyfield gives access to all Earth satellites Two-line element sets (TLE), a data format encoding a list of orbital elements published by [CelesTrak](#) based on observation data released by the North American Aerospace Defense Command for most unclassified satellites.

# 4

## Experimental Setup

Experience from previous studies and satellite missions has shown that the stray light behaviour of limb sounders, including ISHI, is critical to mission success. Initial simulations provided insight into the stray light performance assuming an incoherent light source, a simplified detector model and ideal grating characteristics. However, these simulations did not consider interferences and spectral stray light, so extensive measurement setups are necessary for evaluation. In addition, to ensure metrological traceability, it is necessary to measure stray light-induced measurement uncertainties against known standards. While simulations can aid in early design decisions and identifying the cause of stray light, they cannot replace actual measurements. It has been found that there is a lack of standardization in stray light measurements and published best practices. Therefore, a multi-method

approach is used, followed by cross-validation between different experiments as an evaluation strategy. These experiments are performed end-to-end, meaning that the stray light of the entire system is measured, rather than that of individual components. In particular, experiments that were made for instruments such as TROPOMI<sup>64,72</sup>, MetOp-SG 3MI<sup>119,81</sup>, EnMAP<sup>58</sup> and AtmoLITE<sup>6</sup> have provided useful insights for the development of such a stray light test bench.

#### 4.1 MODULAR ATMOX CALIBRATION UNIT

As part of the InspireSAT4 mission, the ACU (AtmoX Calibration Unit) was developed as a calibration light source to reproduce the in-orbit airglow illumination of the instrument for pre-launch calibration of the spectral performance and for the visibility optimisation. As the optical design of the ACU has proven its validity in terms of collimation quality, wavefront quality and homogeneous aperture illumination requirements, key elements have been adopted in the development of the modular AtmoX Calibration Unit (mACU). Since the ACU is not further modified for repeatability purpose, the behavior of the ACU can be further investigated using the mACU without risking modification of the ACU. More details about the requirements and the optical design can be found in the thesis about the construction of the original ACU.<sup>6</sup> Figure 4.1 shows the first iteration steps to redesign of the mACU. The collimation optics provides imaging of the object plane by the ISHI, whose focal plane is at infinity. The distance and the type of lenses are taken from the ACU. However, all lenses in the improved design are mounted on manual stages to compensate for misalignment and associated imaging errors. The collimating optics are installed on a single optical rail to provide a common reference for the optical axis. An enlarged integrating sphere was chosen to provide a much larger exit aperture and thus reduce vignetting. In further iterations, the rotating diffuser used for speckle suppression was placed not in the object plane as in previous configurations, but at the laser entrance aperture of the integrating sphere. In this way, speckle was still avoided without introducing uncertainties in the object plane due to the dynamic imbalance of the rotating diffuser. In a later step, a standardized height for the optical axis of 180 mm relative to the optical bench was defined, which drastically simplified the integration into various experimental setups.

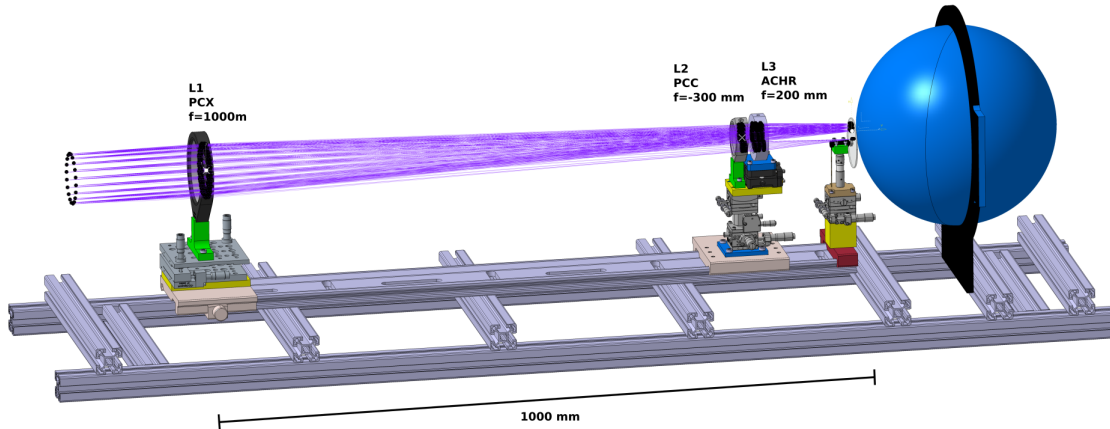


**Figure 4.1:** CAD model of the very first mACU, still using several unstable aluminium profiles instead of a stable solid rail profile as a substructure between the light source and the lenses. The mACU uses the collimating optics of the ACU, but with improved optomechanics and an integrating sphere to allow modularity for a variety of experiments.

#### 4.2 mACU ALIGNMENT AND POINT SOURCE CONFIGURATION

To ensure modularity for a large number of experiments and to maintain a defined alignment of the optics, a process was developed to reproducibly rebuild the entire mACU. Initial experiments showed that the lenses required significant adjustments to optimize aberrations compared to the simulated nominal lens positions. In addition, with a wavefront error Peak-to-Valley (PV) value of over  $2 \lambda$ , significantly higher values were obtained compared to the ACU with a corresponding value of  $0.8 \lambda$ . Therefore, a method was sought to place and align all the lenses as accurately as possible on one optical axis, so that only minimal adjustment of the manual stages was required for subsequent optimization of the aberrations. The point source configuration of the mACU turned out to be ideal basic configuration for the alignment of all optical components and optomechanics. A collimated laser is used to define the optical axis and align all lenses concentric to it. The following steps have been identified to ensure that the entire system is set up correctly the first time:

1. Set all stages to the nominal rotational position and a height of 180 mm relative to the rail contact surface.
2. Align the laser collimator optics with the diaphragm by adjusting the cage kinematic mount.

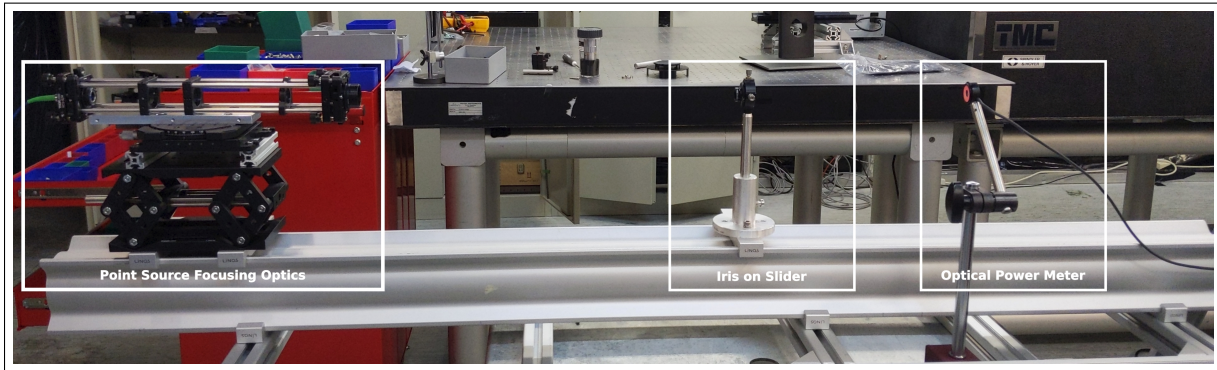


**Figure 4.2:** Final alignment of the mACU optical axis parallel to the optical rail. A hollow cylindrical aluminium optical rail with four lateral ribs, which reinforce the system and also support the brackets, was chosen to increase rigidity and achieve the standard height of 180 mm. The underlying aluminium profile construction connects the mACU with a scissor table to adjust the whole system to a variety of experiments heights.

Measure the maximum adjustable power behind the diaphragm using a power meter.

3. To install the Point Source Focusing Optics (PSFO) focal point, place the last lens ( $L_1$ ) at the end of the rail. Then, adjust the stages holding the cage and the fiber-optic stage to find the highest power passing through the diaphragm. Note that the microscope objective is not mounted in this configuration, so a collimated laser beam defines the optical axis. (See figure 4.2)
4. Place the mACU in front of the autocollimating telescope using a 3D printed pinhole mask to align both optical axes concentrically. To compensate for rotations between the two systems, adjust the three legs of the scissor table of the mACU until both systems are correctly aligned. Use the autocollimator to image the laser beam in the center of the detector.
5. Place lens  $L_1$  on the rail, covering the aperture with the pinhole mask. Align the  $L_1$  lens with the manual stage so that the laser spot is realigned with the optical axis of the autocollimator. Repeat this procedure for  $L_2$  and  $L_3$ .
6. Position the mACU in front of the Zygo Interferometer and install the mounted reference flat. Place the curved mirror surface in the focal plane of the system and align it so that all reflections are directed back to the interferometer. Adjust the position of the mirror along the optical axis

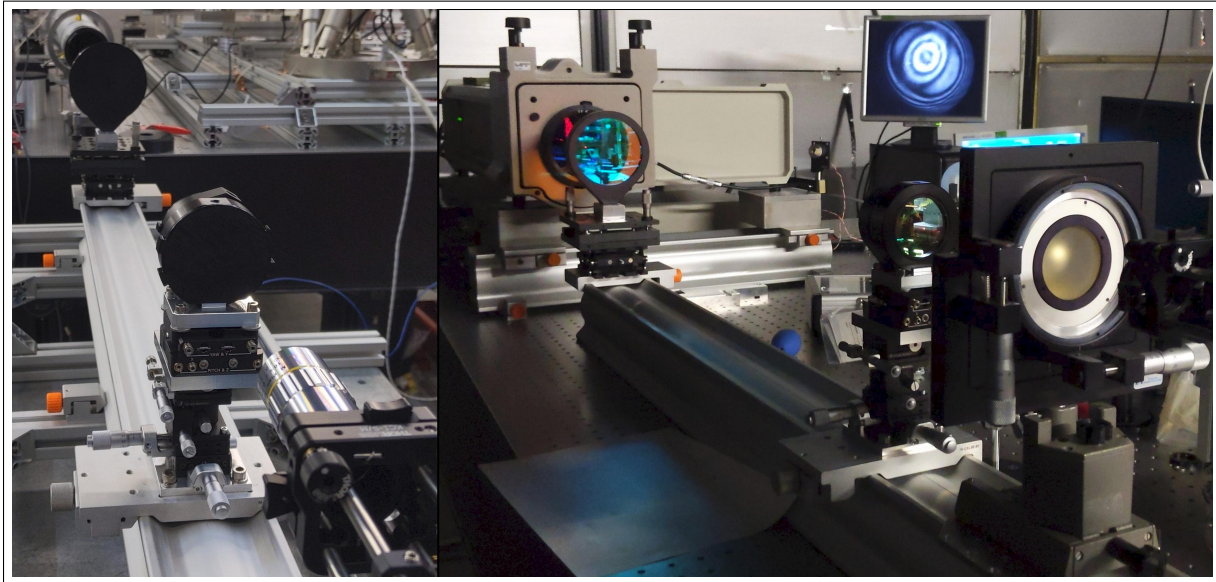


**Figure 4.3: Left:** The final steps of mACU alignment with the autocollimator at the rear end. All apertures are covered with 1mm aperture pinhole masks. The microscope objective has been installed to measure the distance of the lenses to the focal point of the PSFO. **Right:** The mACU is placed in front of the ZYGO Mark GPI-XPS Interferometer to measure the wavefront.

to reduce the fringe frequency and ensure that all interferences are concentric. Lock all stages when the results meet the requirements.

7. Realign the autocollimator telescope optics with the reference flat mirror and band-pass filtered LED illumination by using the slanted edge target.
8. Align the mACU in front of the autocollimator. Install the PSFO with the microscope objective on the rail. Roughly move the PSFO focal point along the optical axis to match the focal point of the mACU. Scan the PSFO over this estimated value in  $100\ \mu\text{m}$  increments and use the position with the highest amplitude as the optimum position.

Previous configurations used a  $25\ \mu\text{m}$  pinhole at the focal point for spatial filtering, but this has been shown in several experiments to increase diffraction and stray light without significantly improving beam quality. Minor shocks, temperature fluctuations, or misalignment of the fiber optic port can cause the focal point of the laser to shift relative to the pinhole aperture. To overcome this issue, the free beam waist of the focused laser is used as a point source without the spatial filtering of a pinhole.

### 4.3 WAVEFRONT AND COLLIMATION

Visibility and spectral stray light are directly dependent on the quality of the incident wavefront, as demonstrated by ZEMAX simulations<sup>6</sup> and experiences from Michelson interferometers.<sup>87</sup> For the ACU, PV and RMS values of 480 nm and 63.28 nm were selected as requirements, corresponding to a perfect point source located over 1 km away from the instrument's entrance aperture.<sup>6</sup> No significant change in visibility is observed in the simulations beyond this distance between the source and the instrument.<sup>6</sup> The previous aberrations and wavefront measurements for ACU were based on a Zygo interferometer at  $\lambda = 632.8$  nm, where the aberration measurement was distorted by a ghost artefact from L<sub>2</sub> causing a strong reflection at the interferometer wavelength. The ACU achieved a PV of 253.12 nm and an RMS of 44.296 nm including an interferogram scaling factor of 0.5 due to the double path measurement. As illustrated in figure 4.3, these wavefront measurements were repeated for the mACU. Through comprehensive alignment of L<sub>2</sub> and L<sub>3</sub> the PV could be reduced down to 456 nm PV and 61 nm RMS. The wavefront errors for the mACU are higher compared to the ACU, but still within the requirements. However, it is unclear from previous ACU measurements which region of interest was used for the evaluation. This greatly influenced the results, as aberrations are strongly increased at higher field angles.

To further validate the performance of the mACU point source configuration, another experimental setup was developed that allows the PSF to be measured with a reference telescope focused to infinity. In the first iteration, a hobbyist astronomy telescope was evaluated with a Bahtinov mask set to infinity on a star target. Although this solution is theoretically feasible, the traceability of this method to a reference standard could not be provided. Therefore, an AKR 1100/105 autocollimator telescope from Möller-Wedel Optical GmbH with a free aperture of 78 mm was identified and configured as a traceable reference. The telescope was equipped with a hobby astronomy camera using the SONY IMX290 CMOS RGB sensor and several Thorlabs LED760L NIR LEDs with a peak wavelength of 760 nm as light source. For self-reference of the autocollimation telescope, the LED spectrum is filtered by the same bandpass filter used for the ISHI. In a collimated beam path

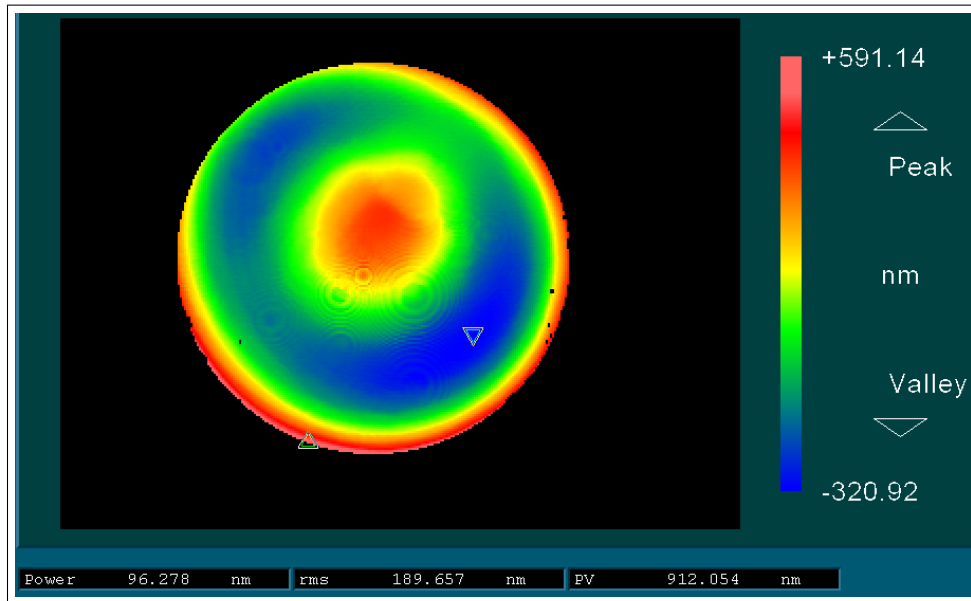


**Figure 4.4:** The mACU wavefront measurement data generated by the Zygo interferometer exhibits a correlation with the intensity distribution. At the outer aperture, the wavefront exhibits a notable decline.

extending to infinity, the autocollimator images a slanted edge target. A mirror in the optical path reflects the beam back into the autocollimator, generating the autocollimation image.<sup>120</sup> During the final acceptance test at the manufacturer, the telescope was referenced with the filtered spectrum to a master collimator, which was calibrated against a measurement angle standard from the Physikalisch-Technische Bundesanstalt. The mirror used for the autocollimation in the laboratory showed a PV value of  $\lambda = 58$  nm and a rms of  $\lambda = 10.4$  nm. Figure A.19 shows the slanted edge target image that was used to manually set the telescope collimation position.

Once the autocollimator has successfully self-referenced, the mACU is aligned with the autocollimator by manually setting the edge extension of the imaged target to minimum. First, the PSFO is manually moved along the optical axis until the highest pixel value is measured on the telescope. The autocollimator was supplied with an RGB image sensor instead of a monochromatic one, which meant that only one third of the pixels were available for amplitude-based optimization. Due to the monochromatic illumination and the small image of the PSF on the detector, the air circulation in the laboratory caused significant fluctuations in the maximum depending on which pixel was imaged by the PSF. For this reason, the average energy in a 10-pixel region around the maximum was used

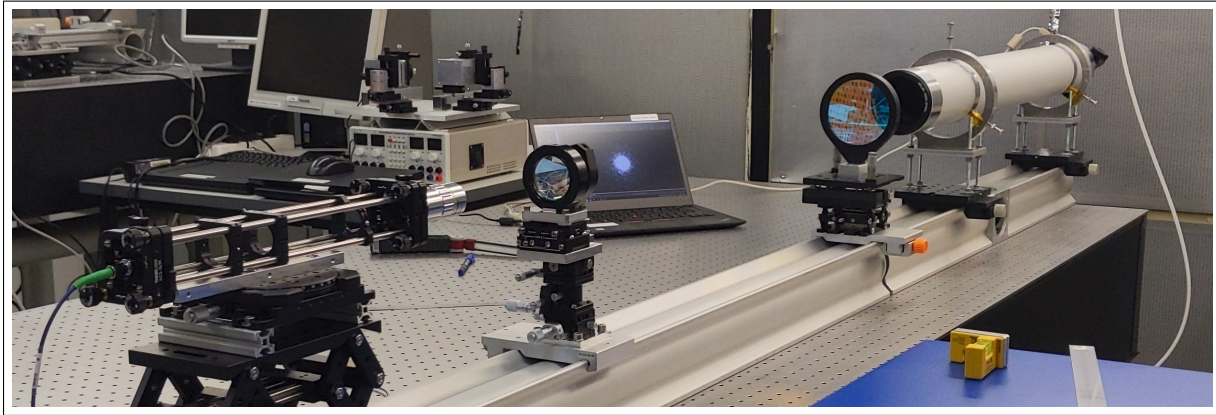


**Figure 4.5:** The mACU is aligned with the autocollimator in order to align the focal point of the PSFO with the focal point of the mACU.

for optimisation rather than the maximum itself. Figure 4.5 shows the final alignment of the mACU in the point source configuration.

#### 4.4 POINT SOURCE ASSESSMENT

The quality of the point light source has a significant impact on subsequent assessments. In the previous test setup, it was not possible to assess the quality of the point light source independent from the ISHI. This made it difficult to evaluate the entire system, which includes both the light source and the instrument. Aberrations or stray light in the light source cannot be distinguished from inherent characteristics of the instrument. The autocollimation telescope allows for comparison with other imaging systems that have simpler optical properties. However, it also has limitations in its evaluation. While the collimation characteristics can be referenced to a standard, the stray light characteristics and PSF cannot. Although the MTF measurements show minimal stray light and high spatial resolution, they only allow for qualitative statements. Three setups were measured with the autocollimator to evaluate different point light configurations:

- i. The microscope objective focuses the free laser waist into the object plane of the collimator, as shown by the image of the experimental setup in figure 4.5. To determine if the telescope and mACU system is diffraction-limited, the PSF is compared to the ideal airy disk. The concentric rings around the peak amplitude of the free laser waist are symmetric, indicating its high

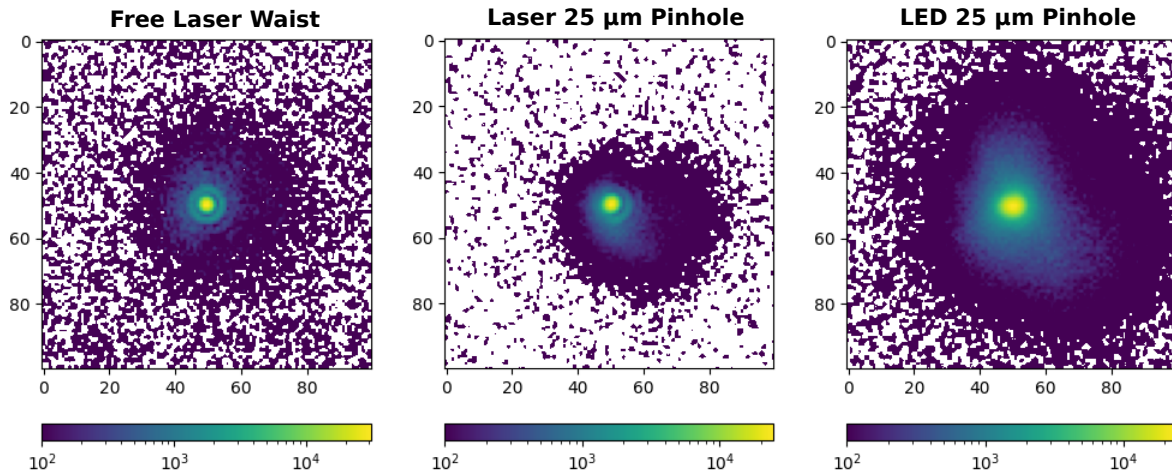


**Figure 4.6:** The autocollimator imaged three point source configurations. Due to the logarithmic scale, stray light below zero is indicated with white color.

quality. The same concentric rings are also symmetric around the tip amplitude. The peak and position of the rings were best fitted using a median radius of 3.4 pixels. However, the amplitude of the first order ring deviates from the ideal diffraction limited airy disc. Additionally, stray light is uniformly distributed around the PSF.

2. The laser beam, when focused on a pinhole with a diameter of 25  $\mu\text{m}$ , produces an asymmetric airy disk ring with a peak radius of 3.9 pixels compared to the free laser beam. The stray light distribution is inhomogeneous, with a strong distribution on one side of the image. However, the stray light decreases significantly as the distance from the peak increases compared to the free laser waist. This suggests that the light source scatters before passing through the pinhole.
3. A high-power NIR LED with the LED dome in direct contact with the 25  $\mu\text{m}$  pinhole exhibits a Gaussian distribution with a peak radius of 7.1 pixels. There are no diffraction patterns in the form of rings, and there is inhomogeneous stray light of high magnitude around the peak.

Table 4.1 shows the stray light level for different configurations as defined by equation 3.25. Despite the lower stray light level of the 25  $\mu\text{m}$  laser pinhole configuration, the free laser waist was chosen. The pinhole configuration proved to be unstable in the laboratory. The slightest adjustment of the fiber or raising and lowering the mACU to a different position caused the laser waist to be mis-

**Table 4.1:** The ratio of stray light to signal is determined by comparing the intensity of a 15 to 50 pixel area surrounding the point spread function to that of a 30x30 pixel area centered on the PSF.

Point Source Configuration	Stray Light 15 Pixel Distance
Free Laser Waist	12.9%
Laser 25 $\mu\text{m}$ Pinhole	9.1%
LED 25 $\mu\text{m}$ Pinhole	30.2 %

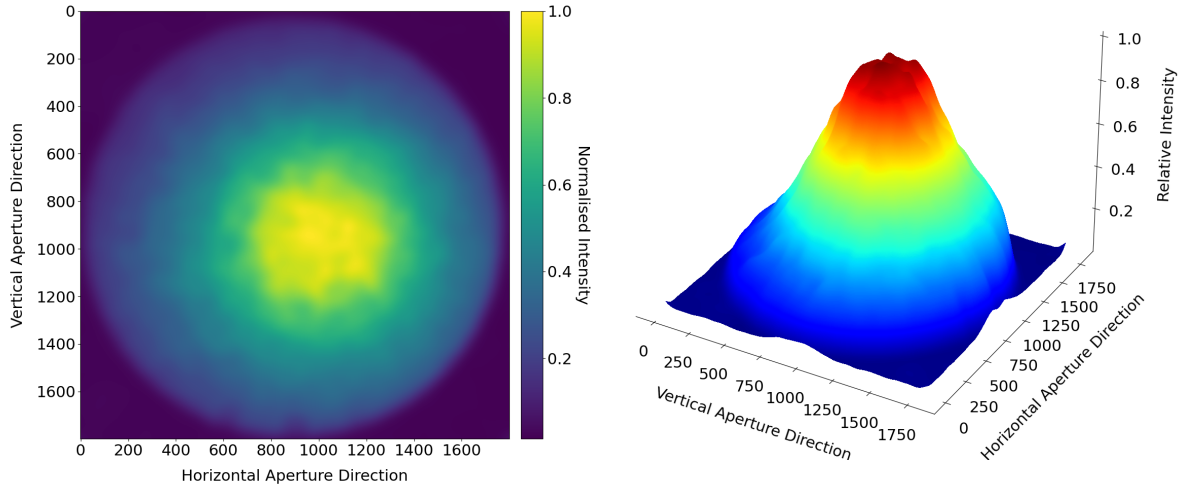


**Figure 4.7:** Left: Median filtered red channel of the collimated mACU beam scattered on a diffuser screen. Right: Gaussian intensity distribution visualized in 3D space.

aligned relative to the pinhole. A significant limitation of a point source laser is the inhomogeneous aperture illumination of the instrument. Imaging the waist of a focused laser results in a Gaussian flux distribution across the instrument aperture. This leads to an underestimation of the stray light in the outer region of the instrument aperture and an overestimation in the inner region. Figure 4.7 is the image of a diffuser screen placed on the collimated wavefront behind lens L2, imaged by an RGB camera placed on the optical axis. The image has been filtered with a median kernel to remove random interference caused by the laser light source. The intensities follow a Gaussian distribution, but the maximum is not exactly at the center of the aperture. For future calibrations, it is necessary to correct or remove such effects by precisely measuring the angular and lateral dependence of the aperture illumination, as was done for the original ACU.

Considering a Gaussian beam with a wavelength of  $\lambda = 763 \text{ nm}$  in air focused by the microscope objective with an numerical aperture (NA) of 0.28 the beam diameter  $d_w$  of  $17.35 \mu\text{m}$  at the focal

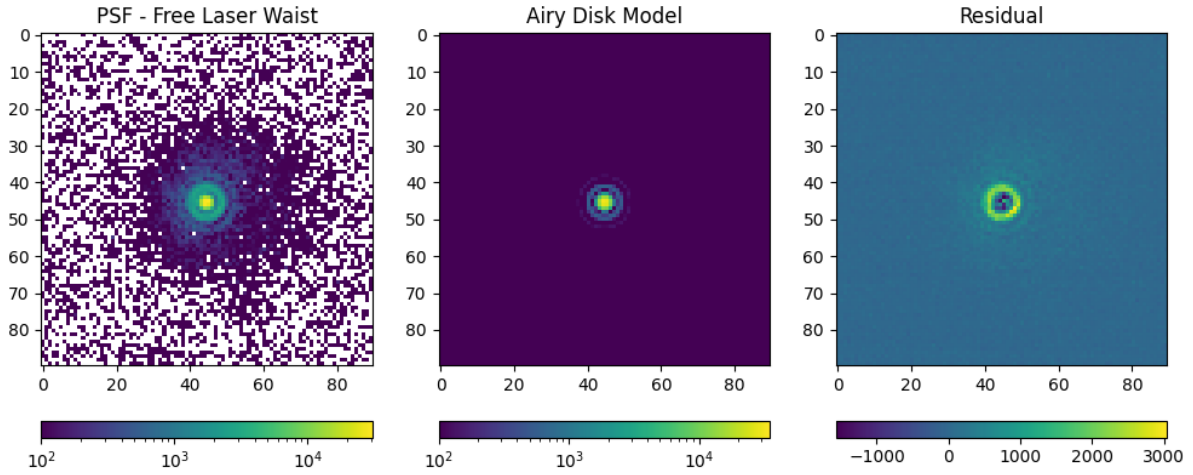


**Figure 4.8:** The PSF images of the free laser waist measured with the autocollimation telescope are fitted with an airy disk model using the AstroPy<sup>75</sup> software package.

point is given by equation 4.1<sup>121</sup> and 4.2:

$$w_0 = \frac{\lambda}{n\pi\Theta} = \frac{d_w}{2} \quad (4.1)$$

$$NA = n \sin\left(\frac{\Theta}{2}\right) \quad (4.2)$$

The detector's pixel resolution is reduced by one third when using only the red channel. This results in spatial resolution of 8.75  $\mu\text{m}$  per pixel, as determined by a fixed frequency grid distortion target measurement. Thus, the point light source resulting from the diameter of the beam waist is in the order of magnitude of the spatial resolution of the optical system. Taking into account the diffraction limits, which only arise in relation to the NA of the ACU of 0.0484<sup>6</sup>, a maximum resolution of 7.88  $\mu\text{m}$  is possible under consideration of equation 4.3. Within the image, however, the free beam waist has a diameter of 6.8 pixels, or 59.5  $\mu\text{m}$ . This means that the entire optical system of the autocollimator and mACU cannot be considered as diffraction limited.

$$d = \frac{\lambda}{2 NA} \quad (4.3)$$

However, when the PSF is compared with an airy disk model, there is a slight residual from the

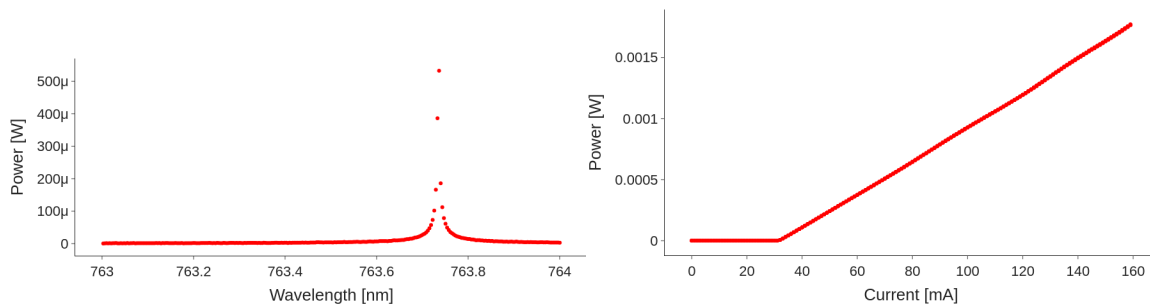


**Figure 4.9:** **Left:** The laser spectrum measured with spectrum analyser. **Right:** The relationship between laser power and laser current is under examination. The gradient is significantly increased at the laser threshold between 31 and 32 mA.

ideal PSF, with the first and second rings visible in the measurements. Figure 4.8 displays the measured PSF and its fit to an Airy disc model. The stray light components surrounding the PSF are challenging to differentiate from the second-order coaxial ring due to their similar order of magnitude.

#### 4.5 LASER LIGHT SOURCE

To study spectral stray light, a narrowband light source is required that can be tuned in wavelength over the entire spectrum of the instrument's bandpass filter. The TOPTICA DL pro tunable diode laser was used as a calibration light source for various ISHI experiments in the laboratory and was chosen for stray light calibration because of its narrow bandwidth and automation capabilities. The Bristol 771 Laser Spectrum Analyzer measures the spectrum with a spectral resolution of 0.0035 nm using a Single Mode Fused Fiber Optic Coupler. An optical power meter, the Thorlabs SI20C/PM101U, was integrated with another fibre optic coupler to record the power output of the laser. The spectrum tuned to a peak wavelength of  $\lambda=763.73$  nm and FWHM=0.0082 nm. The emitted radiative flux dependence on the diode current of the laser light source are shown in figure 4.9.

At a laser current of 32 mA, the laser threshold is indicated by a sudden change in gradient. Above the threshold, the linewidth of the laser emission is significantly narrower than below it. Below the laser threshold, the spectrum of the laser cannot be determined with the given measuring instruments. The light source operates below the laser threshold in Amplified Spontaneous Emission (ASE) mode, producing a broadband spectrum. Initial PSF experiments showed that the spectrum

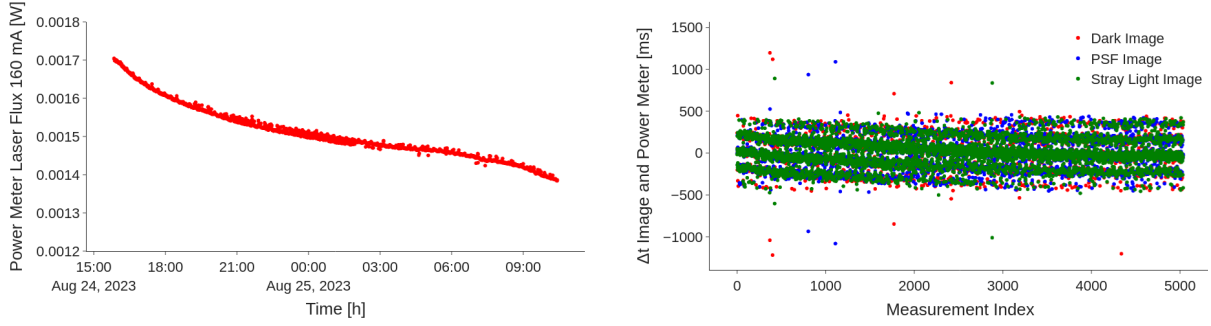


**Figure 4.10:** **Left:** The laser power decreases constantly over a point source mapping (PSM) measurement, therefore it is necessary to normalize all measurements over the power measurements. **Right:** To verify that the laser was off during the dark images, the time difference  $\delta t$  between the power meter timestamp and the dark image timestamp is checked.

analyser's own laser is coupled back into the fibre, making it impossible to continuously monitor the laser spectrum in subsequent experiments unless a bandpass filter is installed on the instrument. In order to match the laser power output to the detector sensitivity and integration time at 200 ms, and to avoid saturation of the detector, the laser power was split using a measured ratio of 241.75 through multiple fibre couplers. This provided approximately 4.55  $\mu\text{W}$  to the mACU and 1.1 mW to the power meter at a maximum diode current of 160 mA. To avoid any damage to the detector, a worst case assessment was made. Assuming full nominal laser power of 40 mW coupled into the mACU system, this could theoretically be focused onto a single pixel:

$$E_{max \text{ per pixel}} = \frac{P_{laser}}{A_{pixel}} = \frac{40mW}{11\mu m \times 11\mu m} = 330.57 \frac{MW}{m^2} \quad (4.4)$$

$$E_{damage \text{ threshold } 10 \text{ s}} = 490 \frac{MW}{m^2} \quad (4.5)$$

Even in the worst-case scenario, the threshold value cannot be reached within 10 s. It is unlikely that the laser power will reach such high levels in practice, as the stray light experiments used less than 2 mW power, which was further reduced by the fiber coupler. Note that these values apply only to an integration time of 10 seconds. Continuous high irradiance can cause damage even at lower power levels. However, no study has provided threshold values for long-term irradiance. Consequently, safety functions are incorporated into the automation control and calibration process to ensure that

the laser current is consistently set to zero in the event of a failure in the experimental control system.

The use of out-of-field stray light artifacts is a common way to find the initial alignment of the mACU relative to the instrument manually. This requires very high power configurations, so special care must be taken to deactivate the laser after successful alignment.

#### 4.6 INSTRUMENT STAGE

Initial calibrations for INSPIRESat 4 were performed using a manual instrument stage to align the LOS and aperture with the optical axis of the ACU. Several manual stages were combined to allow the instrument to move in five degrees of freedom. However, this construction had significant limitations, hazards, and uncertainties:

1. Over time, the manual stages became deformed, making linear movement impossible and posing a risk of damage to the instrument if any of the stages were to fail.
2. The pivot point, also known as the centre of rotation, was fixed to a point in space, which proved to be impractical, especially for stray light measurements, as PST measurements require rotation around the centre of the baffle aperture.
3. The manual stages were lubricated with grease that is not compatible with vacuum, posing a contamination risk for the entire calibration setup in the vacuum chamber. Degreasing and re-lubricating with vacuum compatible grease proved impractical as some parts, such as bearings, could not be completely disassembled.
4. When external forces were applied to the instrument through mounted heat exchangers and cooling tubes for thermal cycling, the manual stages were not rigid in all directions. Especially for the rotation around the vertical axis, there are no manually adjustable stages that can be precisely adjusted and at the same time allow high torques.
5. A lack of automation meant that the instrument could not be adjusted in vacuum and PSF

measurements were limited to a few field angles under ambient conditions to maintain reasonable measurement times.

Based on this experience and the requirements with regard to stray light measurements, a vacuum-capable hexapod was chosen as an instrument platform for the stray light experiments:

**Table 4.2:** Specification under ideal conditions of the hexapod used as an instrument table.

H-850.V Vacuum-Compatible 6-Axis Hexapod	
Travel range X and Y	$\pm 50$ mm
Travel range Z	$\pm 25$ mm
Rotation around X and Y	$\pm 15$ deg
Rotation around Z	$\pm 30$ deg
Repeatability	$\pm 0.2$ $\mu$ m
Load capacity in Z	80 kg

Table 4.2 specifies the maximum load and range of motion when the hexapod’s pivot point is at its center. In order to perform a PST measurement, it is necessary that the center of gravity of the instrument is situated outside the center of the hexapod, in order to permit rotation around the center of the first baffle aperture. Positioning the first baffle opening exactly at hexapod’s center is not possible because the hexapod table would block the mACU light cone during rotation. Excessive torque load also limits the hexapod’s range of motion. The manufacturer’s simulation software was used to calculate the maximum allowable rotations of  $\pm 4$  degrees in the vertical and horizontal directions at the given pivot point and load condition. The location of the hexapod’s pivot point was measured relative to the nominal center of rotation through the use of a ruler, due to the lack of CAD data and the necessity of utilizing handmade adapter plates. To verify the center of rotation of the hexapod, a needle was placed at the intersection of the theoretical axis of rotation with the baffle body. During rotation of the instrument around this axis, the needle should not move laterally with respect to the housing. This was confirmed for rotations around both the horizontal and vertical image directions. Rotations around the LOS were not conducted during this measurement campaign. Only the angle between the horizontal axis of the image and the hexapod horizontal axis was compensated using the three legs of the mACU table.

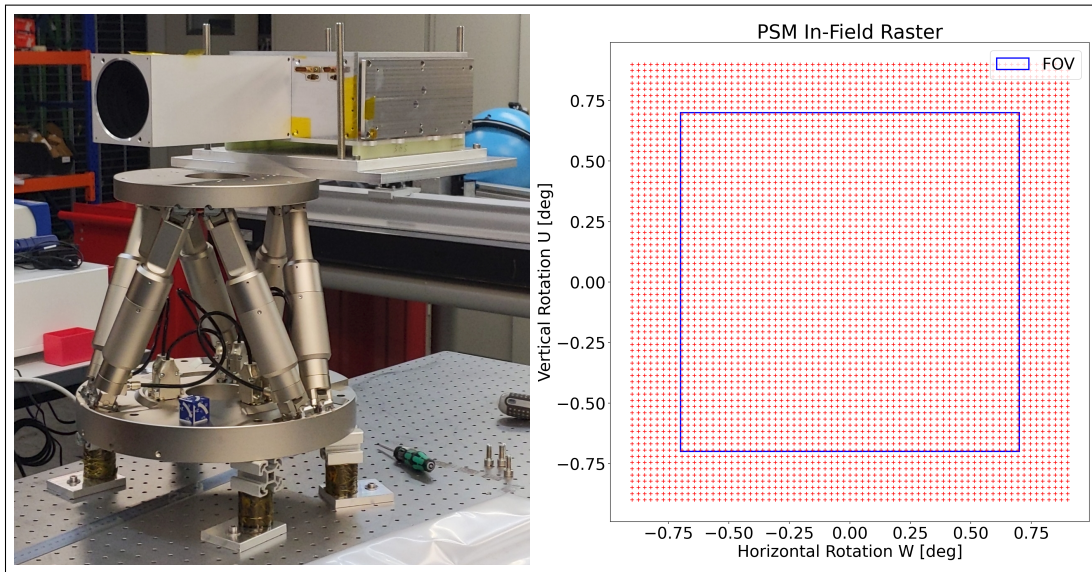


**Figure 4.11:** **Left:** The hexapod is equipped with the QM instrument. Vibrations from the optical bench caused by the clean room ventilation were visible when the interference patterns are adjusted. Therefore the whole system is mounted on vibration dampers. **Right:** The 71x71 in-field PSM raster configured for the movements of the hexapod.

Figure 4.11 reveals the SHIPAS QM instrument installed on the hexapod. During operation, the instrument is mounted on the stage with its upper side facing the ground, corresponding to the positive  $Z$  axis of the hexapod. The LOS is aligned with the positive  $Y$  direction of the hexapod. A positive horizontal rotation  $U$  around the  $X$  axis results in a rotation of the LOS away from the earth surface. A positive vertical rotation  $W$  moves the LOS to the right along the local horizon.

#### 4.7 CALIBRATION TARGETS FOR MACU

The mACU has a unique improvements with respect to the ACU: it can provide different imaging characteristics for different targets and illumination without sacrificing reproducibility. This is achieved by removing the diffuser disc from the object plane of the mACU. Despeckling of the laser light source is performed at the input port of the integrating sphere rather than at the output port. As a result, various targets can be placed in the object plane. During small-scale experiments conducted as part of the INSPIRESat 4 mission, suitable targets and light sources were identified for later validation in orbit:

1. A point source is created by using a LED or laser light source. This method enables the mea-

surement of the PSF and spatial scattering of stray light. To reduce light source scattering before the object plane, a pinhole can be installed in the object plane.

2. A custom designed slit with two opposing straight knife edges at a distance of 2 mm is illuminated by the integrating sphere using laser light, NIR LEDs or white LEDs as shown in figure 4.12. This target allows simultaneous measurement of Modulation Transfer Function (MTF), visibility, and stray light for a limited detector area. Placing the slit horizontally in the center of the image also provides illumination similar to the airglow peak intensity in orbit, as can be seen in the AtmoSHINE data shown in figure 2.4.
3. The grid distortion target is used to measure the combined distortion of the front optic, camera optic and mACU. The target is illuminated by a white or NIR LED scattered by the integrating sphere.
4. The use of a Ronchi rule target with an SHS instrument has not yet been published. It offers similar advantages to the use of slit targets for the simultaneous measurement of stray light, MTF and visibility. Unlike the slit target, it assesses the entire FOV without requiring vertical or horizontal scanning. The only Ronchi ruling targets available were those with chromium-plated reflective strips, as shown in the figure 4.12. Ideally, a highly absorbent black coating should be applied to the Ronchi ruling strips for MTF and stray light measurements. The selected target provides 1.016 lines/mm and thus divides the FOV into 20 signal stripes and 20 associated shadow stripes, which approximates the height resolutions to be achieved in orbit after binning.
5. To replicate lunar observations in the laboratory, the semiconductor surface of a high-power LED can be placed at the object plane of the mACU. This surface resembles the lunar surface because it is a broadband light source with recognizable structures. In addition, it can generate unmodulated out-of-field stray light measurements, such as those from direct Sun and Moon illumination in space.

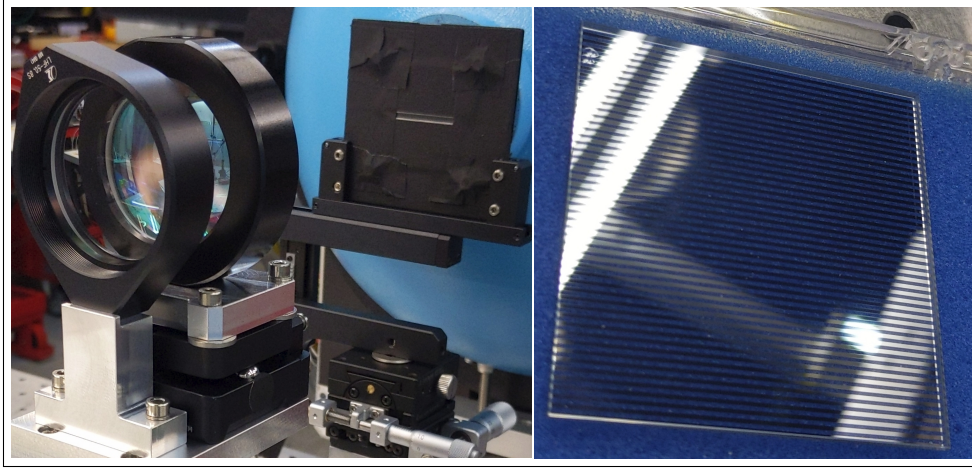


**Figure 4.12:** Left: The slit target is positioned at the exit of the integrating sphere. It can be adjusted using a series of manual stages, giving a total of five degrees of freedom. The same stage is used for the grid distortion target, diffuser target and Ronchi ruling. Right: The installed Ronchi ruling with 25 lines per inch and a total size of 1 inch x 1 inch.

6. A diffuser target was placed at the object plane to provide uniform illumination, similar to the ACU but without the rotating disc. This enables further investigation and improvement of the ACU design without interference from the rotating disc.

All targets are placed on manual stages with 5 degrees of freedom to align the entire target surface with the focal plane. Because the magnification of the autocollimation telescope is greater than that of the instrument, targets must be scanned laterally across the FOV to correct for rotational misalignment. To image the mACU object plane with the autocollimation telescope, laser light at the ISHI band pass middle wavelength of 763 nm must be used to adjust all targets. This is because there is no bandpass filter available for this purpose and the focal length is dependent on the wavelength. To prevent any out-of-field stray light from entering the FOV beyond the in-field boundaries, all extended targets are placed in 3D printed masks that match the FOV measured with the grid distortion target. The masks are covered with highly absorbent black material to prevent relapsing light from being reflected back from the mACU reentering the nominal path of the instrument.

#### 4.8 POINT SOURCE MAPPING

State of the art stray light measurement setups are limited to automated out-of-field stray light measurements or in-field measurements that do not fully investigate the spatial in-field stray light behav-

ior. Astronomical observatories and satellite instruments however regularly use stellar point source targets to measure the PSF over the entire FOV, but so far no detailed experimental setup can be found in the literature that is capable of measuring in-field stray light, out-of-field stray light, and PSF in a single experimental configuration end-to-end under laboratory conditions. For this purpose, a new method of stray light measurement called Point Source Mapping (PSM) has been developed similar to the PSF Microscanning methods used for the James Webb Telescope<sup>122</sup> and PLATO mission.<sup>123</sup> It allows to measure the PSF and the stray light distribution matrix  $D$  (see equation 3.17<sup>79</sup>) over the entire FOV and simultaneously measure the out-of-field stray light behavior. Furthermore, this experimental setup corresponds to the end-to-end simulation in ZEMAX, where the entire interferogram was reproduced using a point source scanned over the entire FOV.<sup>6</sup> Thus, the overall optical performance can be studied and compared by converging experimental and simulation results. Figure 4.13 gives an overview of all components used in the experiment and the automation.

#### 4.9 EXPERIMENTAL PROCEDURE

The stray light experiments to evaluate the SHIPAS QM were carried out in two phases. Preliminary results from Ronchi ruling measurements indicated an unexpected stray light level during the second phase of the SHIPAS QM construction. Several hands-on experiments showed that the amount of stray light increased by a factor of up to three depending on the adjustment of the novel front optics. To investigate this issue, the novel stray light measurements were applied for the first time. In May 2023, the first phase of experiments was conducted using an interferometer from the previous INSPIRESat 4 mission preparation. The objective was to become familiar with the new optomechanics and alignment features of the front and camera optics. This phase only included Ronchi ruling and PSF measurements, as the PSM automation was not yet complete. Measurements were made in-field without the bandpass filter and baffle. The instrument enclosure was open to align the gratings. All measurements were made at a single wavelength of 763 nm in ambient conditions without a vacuum chamber window between the mACU and the instrument.

The main phase of the stray light measurement was performed in August 2023 under ambient

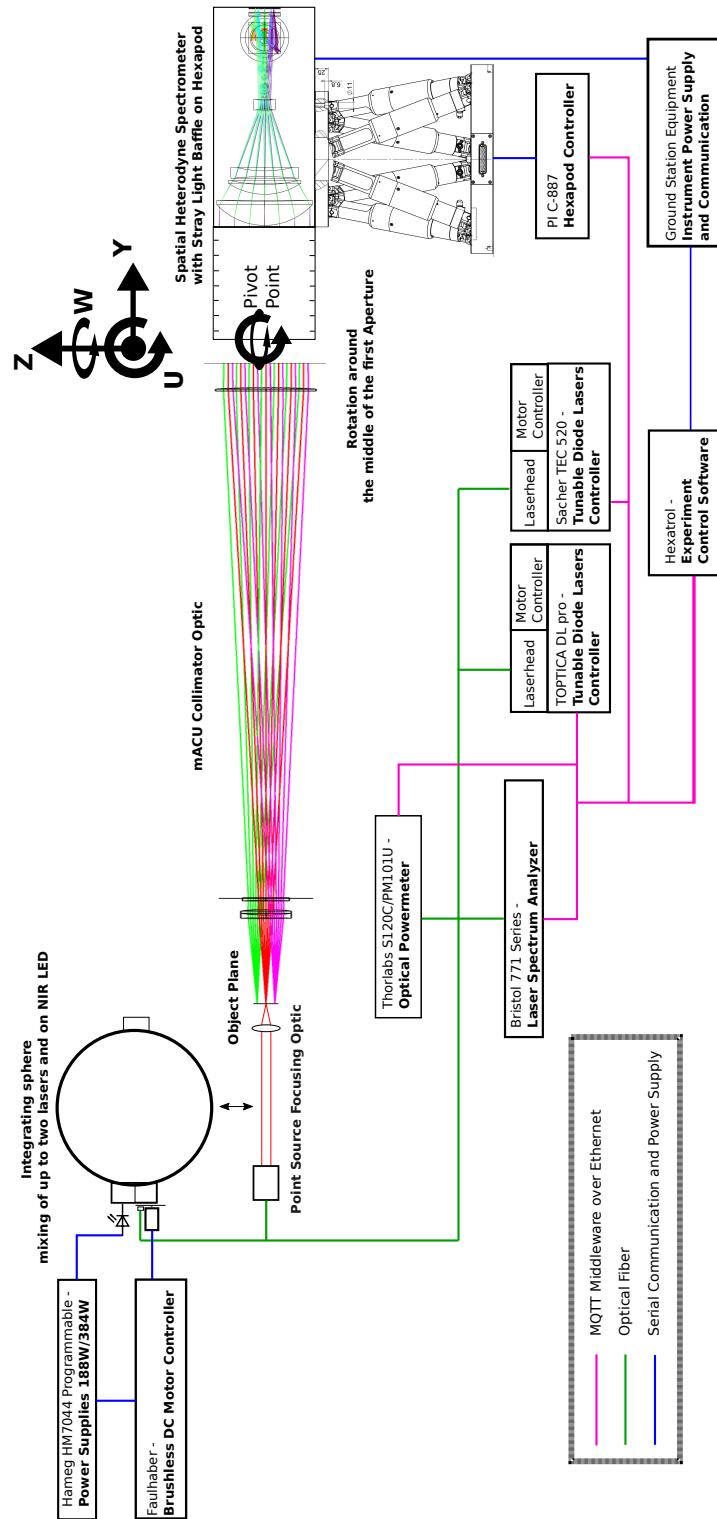


**Figure 4.13:** Setup of the Point Source Mapping (PSM), Ronchi Stray Light (RSL), and Slit Stray Light (SSL). The laser power, wavelength tuning and instruments movement on the hexapod can be controlled via the MQTT middleware by Hexatrol control software. The Point Source Focusing Optic (PSFO) can be replaced by the integrating sphere to enable measurements with extended targets such as the Ronchi ruling.

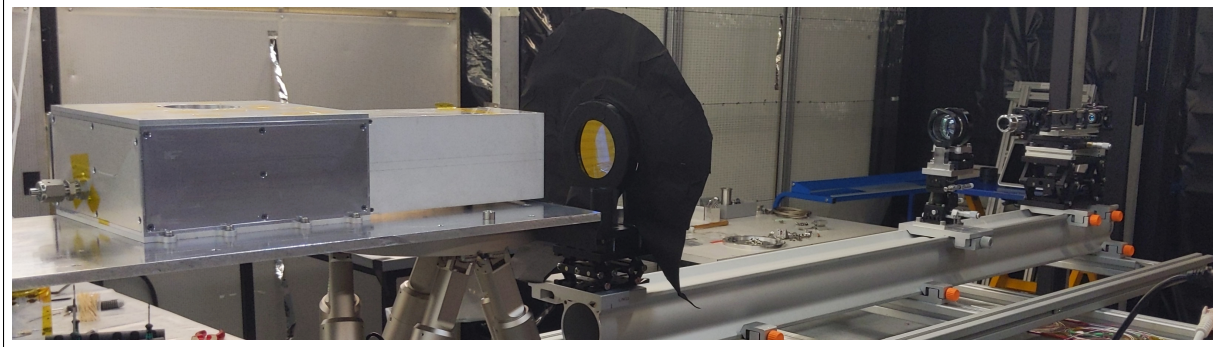


**Figure 4.14:** Stray light measurement performed for Configuration C in-field and out-of-field using the PSM (Point Source Mapping) experimental setup sketched in figure 4.13.

conditions at a wavelength of 763 nm with an integrated baffle and bandpass filter. The point source was positioned at the optical center of the image for angle alignment. To prevent any other light source from entering the instrument, the outer area of L2 was blocked by a 3D printed shield. This was necessary because 50% of the light power entering the instrument is reflected back out of the instrument. The laboratory was darkened and only the mACU provided illumination. A photograph of the experimental setup is shown in figure 4.14. The distance between the first instrument baffle surface and the lens holder surface was set to 12.5 cm. To align the baffle aperture and LOS with the mACU, the symmetry between the baffle housing and the L2 lens holder was measured with a ruler. To align the angle between the LOS and the optical axis, the point source was placed in the center of the image, which was considered the optical center. Rough adjustments were made by moving the mACU's scissor table, specifically the three individually height-adjustable legs. Fine adjustments were made using the hexapod kinematics. Once in the final position, a coordinate system was set in the aligned state to define the zero coordinates and angles in the hexapod software for the following experiments.

Initially, individual stray light measurements were taken at a maximum angle of incidence of 4 deg. At full laser power ( $4.5 \mu\text{W}@160\text{mA}$ ) and 200 ms exposure time, a stray light to noise ratio of over 300 was measured after dark image subtractions for the PST value. Stray light measurements were taken in-field using a current of 30mA to produce a high stray light signal but without saturating the ghost artifacts. For the PSF measurements, a current of 10 mA was used, resulting in a broadband

ASE light source since the laser is operating below the laser threshold. As a result, the two wavefronts from the gratings did not produce any interfering patterns in the imaged PSF. The peak values for the middle detector area were approx. 3500 counts. To ensure sufficient signal over the entire FOV, several sample images were taken manually to confirm that the peak was at least 500 counts and below the saturation value of 4095. To measure stray light both in-field and out-of-field, a sequence of dark images, PSF images, and stray light images was configured in the PSM control software. This allowed the exact position, shape, and dark image of the PSF to be determined for each measured field angle.

After conducting several preliminary tests, the control of the hexapod, the image acquisition, power meter measurements and the laser control were optimised to perform measurements every 5 s. To ensure proper attribution between the different measurement devices, it is necessary to keep sufficient waiting times. This is because the system does not provide real-time and the measurements are not synchronized in their sampling rates. By monitoring the time stamps, overlap between the dark image, PSF and stray light measurements can be avoided. Initial measurements have shown that the PSM can operate error-free for 24 hours using 9 automated instruments and 6 laptops. Based on this experience, a  $71 \times 71$  grid was selected for in-field and out-of-field measurements. One PSM measurement set took around 21 hours and produced 14,700 images. The maximum allowed grid size of  $\pm 4$  deg  $\times$   $\pm 4$  deg, limited by the hexapod capability, was chosen for out-of-field measurements resulting in a resolution of 0.1142 deg. To acquire the complete FOV boundaries and measure near-field stray light, a  $\pm 1.0$  deg  $\times$   $\pm 1.0$  deg grid with a resolution of 0.028 deg has been selected. The in-field and out-of-field PSM grid can be seen in figure 4.11 and A.9.

# 5

## Data Processing and Methodology

Data processing was done in Jupyter Notebook using efficient Python image processing libraries such as Numpy, scikit-image and Astropy. Plotting the intermediate images and results in the Jupyter Notebook enabled manual validation of the data processing. In this way, stray light images were first viewed manually, which provided the first important insights for later data processing. This ensures reproducibility and efficiency in image processing. The experimental metadata was handled using Pandas. The data processing was kept as simple as possible in a single Jupyter Notebook file for each dataset, so that the complete data processing with all variables and the resulting plots could be stored in Git version control system. Depending on the analysis, data processing took from 20 minutes to 8 hours on a standard laptop, as no parallel processing is implemented so far. To store data between

sessions, the Python package Dill<sup>124</sup> was used to serialize and store all variables between sessions on the local disk. Unless otherwise noted, the stray light-intensive instrument front optic configuration C is examined when using the PSM method.

## 5.1 PRE-PROCESSING AND TIMING

Timing issues are critical to data consistency, so the first test performed on all datasets is to measure the offset between the power meter timestamp and the image timestamp. All measurements with delays exceeding  $\pm 2$  s were set to None and are therefore excluded from further processing. Figure 4.10 shows a typical distribution of the time stamp variations, which range within  $\pm 500$  ms with only a few outliers. By comparing the length of the dataset, it is also possible to check that the total number of power meter measurements matches the total number of images. The long duration of the experiment and the strong temperature fluctuations within the laboratory of approx.  $5$  °C over the entire experiment led to a drift of dark current. For this reason, a median dark image  $N_{median\ n}$  of the last  $n = 40$  measurements was used for stray light evaluation. This median dark images was also sufficient enough to compensate for discharging lag noise. All images were also corrected for defect pixels. This was achieved by configuring a PSF with a peak at 600 counts. A series of 100 images was subsequently taken. Any pixel other than the PSF peak that exceeded the 600 count threshold was set to zero for all subsequent measurements.

Figure 5.1 presents the temperature drift of the out-of-field PSM measurement. As the angles are approached in the horizontal direction, the total dark current count decreases in the vertical rotation U throughout the measurement period as the temperature decreases during the night. The high laser power causes discharge lag noise when the FOV is directly illuminated, leaving charges in the dark images. The histogram of two subtracted dark images shows that the remaining noise pattern is Gaussian distributed with a mean of zero. For this reason, negative values in the corrected image need to be preserved when subtracting dark images. Since stray light evaluation requires the sum of entire detector regions, all other noise effects should ideally add up to zero as it is the case for Gaussian profile with a zero mean.

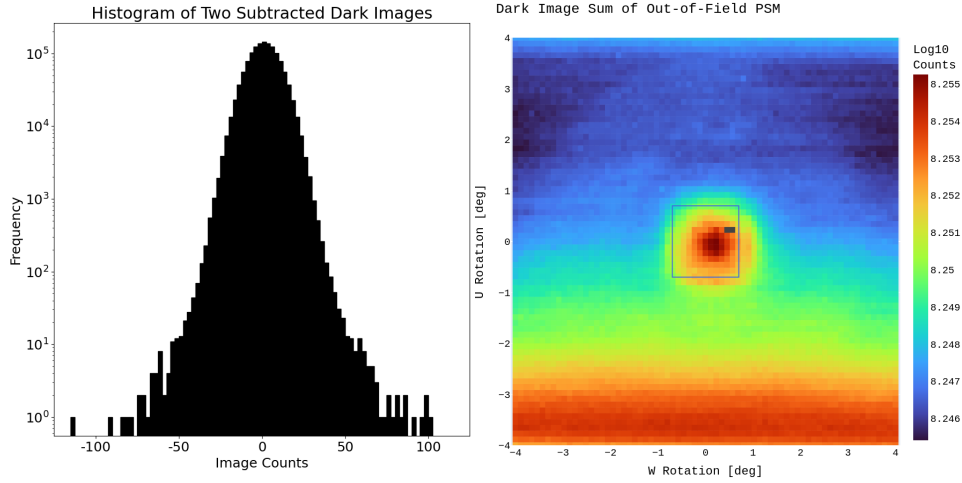


**Figure 5.1:** **Left:** The histogram of two subtracted dark images shows a Gaussian distribution with the mean at zero. **Right:** The sum of the dark image counts shows the discharge lag noise and temperature drift over the entire 21-hour experiment. Mapping starts at -4 degrees vertically and -4 degrees horizontally and proceeds horizontally.

## 5.2 POINT SPREAD FUNCTION

The optical resolution at the optical axis was first evaluated by fitting the instrument’s PSF to an airy disk model. Since the diffraction ring of the PSF could not be resolved, the 2D Gaussian model implemented in Astropy was used instead, as it provides a good approximation of the inner spot.<sup>124</sup>

$$f(x, y) = Ae^{-0.5(\vec{x}-\vec{x}_0)^T\Sigma^{-1}(\vec{x}-\vec{x}_0)} \quad (5.1)$$

$\vec{x} = [x, y]$ ,  $\vec{x}_0 = [x_0, y_0]$ ,  $A$  corresponds to the peak value and  $\Sigma$  is the covariance matrix.  $\rho$  is the correlation between  $x$  and  $y$ , which should be between -1 and +1. Positive correlation corresponds to a theta in the range 0 to 90 degrees.

$$\Sigma = \begin{pmatrix} \sigma_x^2 & \rho\sigma_x\sigma_y \\ \rho\sigma_x\sigma_y & \sigma_y^2 \end{pmatrix} \quad (5.2)$$

The 2D Gaussian, unlike the airy disc, can by definition be asymmetric, accounting for asymmetries caused by image distortion at higher field angles. Figure 5.2 illustrates the high spatial resolution

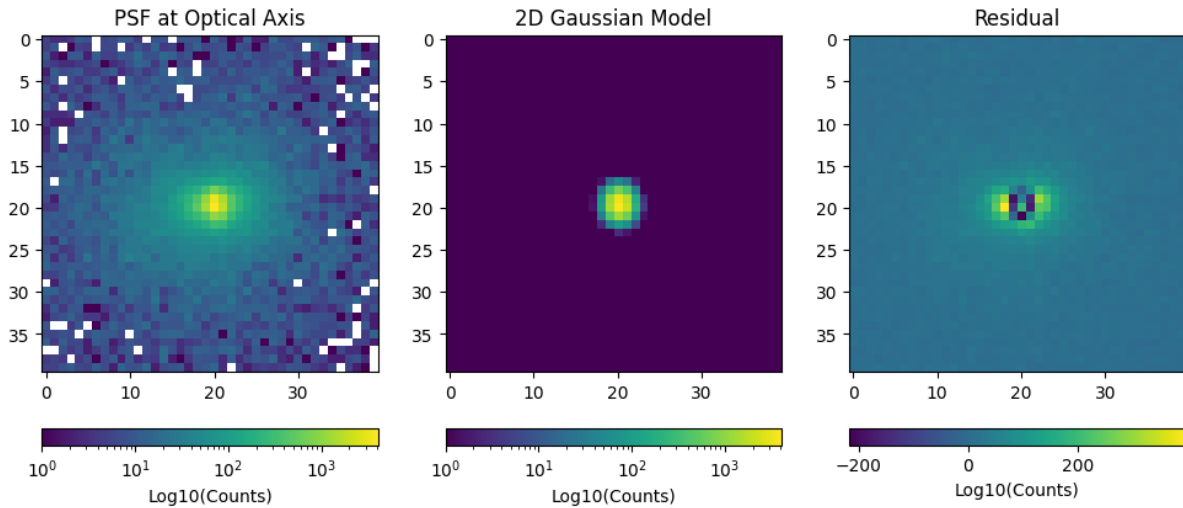
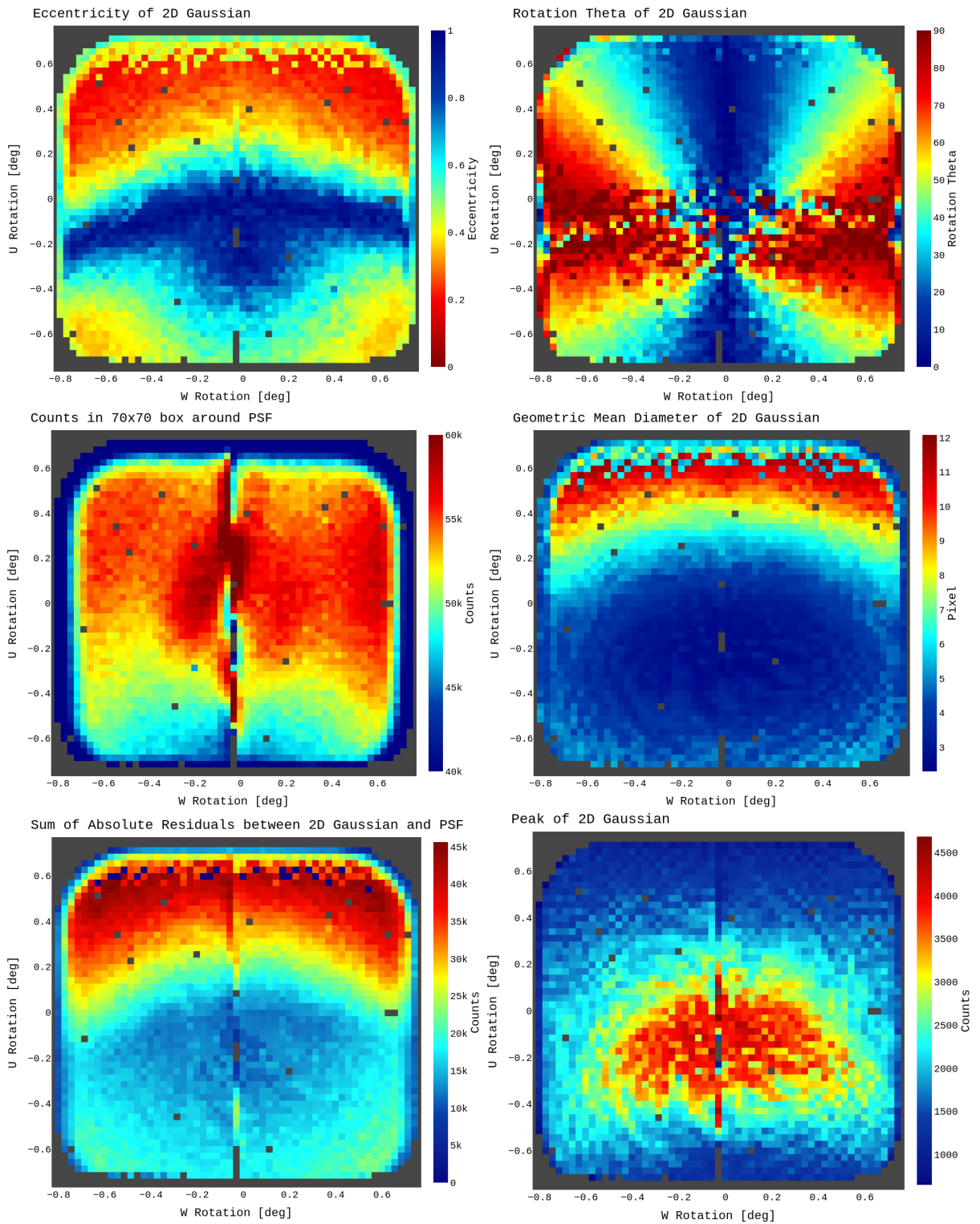


Figure 5.2: The fit of the SHIPAS QM instrument PSF on the optical axis shows low residual to an 2D Gaussian model.

that could be achieved in the image center with  $FHWM_x = 1.85$  Pixel and  $FHWM_y = 2.08$  Pixel. The FOV is limited at horizontal middle axis  $w$  at  $-0.799$  deg and  $+0.742$  deg. The horizontal vertical axis  $u$  is limited at  $-0.71$  deg and  $+0.71$  deg.

The sum of all PSF images is shown in Figure A.10, which illustrates the infield grid and the precise FOV boundaries. To evaluate the spatial characterization of the entire FOV, the PSF measurements of all field angles are fitted to a 2D Gaussian model. Figure 5.3 shows the variation of the 2D Gaussian parameters. At about  $W = 0$  deg the Barber pole is visible in all evaluations, showing the superposition of the broadband interference patterns caused by the point source. For this reason, data from this region is not included in further analysis. In the upper part of the image, two overlapping Gaussian shapes are visible, resulting in two peaks up to 12 pixels apart and thus a much larger 2D Gaussian diameter fit. This is also visible by the increased residual between the model and measurement data in the upper part of the image. Another strong indicator for misalignment in the upper part of the image is that the eccentricities proceed asymmetrical with respect to the image axis. Similarly, the rotation of the 2D Gaussian fit reveals an optical centre that differs from the image centre. In regions where the eccentricity is almost one, the Gaussian fit cannot accurately determine the rotation  $\theta$ , resulting in high uncertainties. The amplitudes in the optical center are unevenly distributed, with some exceeding the detector threshold of 4095 counts. This is due to the fitting



**Figure 5.3:** Fitting the PSF with a 2D Gaussian from the AstroPy<sup>75</sup> provides various insights into the optical properties of the ISHI system. The counts within the 70x70 box used for fitting the PSF indicate higher stray light levels at the lower end of the image.

of two pixels near the saturated pixel value. However, as the residual in this region is very low, these patterns are not measurement artefacts. This could be explained by irregularities in the beam profile, which are known to occur in Amplified spontaneous Emission (ASE) operation of a laser.<sup>125</sup> The sum of the 71x71 pixels, used to fit the 2D Gaussian coefficient, decreases sharply towards the bottom of the image. One way of explaining this pattern is stray light, since in this region the energy exceeds the boundaries of the 71x71 pixel windows due to scattering within the instrument. The power meter's PSF measurement resolution was not sufficient to resolve the laser drift. Therefore, the data was normalized by the stray light power drift, assuming that the system drifts equally in both power configurations.

### 5.3 IN-FIELD STRAY LIGHT

#### 5.3.1 BACKGROUND STRAY LIGHT

To limit detector noise uncertainties in the stray light measurements the Background Stray Light (BSL) method (see equation 3.18) has been chosen to estimate in-field stray light with the point source. To achieve a sufficient stray light to noise ratio for a large part of the detector, the laser power was automatically adjusted since the detector integration time could not be controlled remotely. In order to extrapolate the saturated pixels in the stray light image, it was planned to extrapolate the PSF images based on the two power measurements. To measure the linearity of the detector in this power range, the current was increased from 0 to 160 mA in 1 mA steps for each image quadrant. The laser power used for the experiments was only about 10% of the expected power due to temperature sensitive coupling into the fibre port combined with a sudden increase in temperature in the laboratory. As a result, the PSF power could only be measured close to the resolution of the power meter, making it impractical for the extrapolation. Therefore, only pixels that were not saturated near the peak in both images were used for power scaling. For all in-field straylight measurements, an average power gain ratio between PSF and straylight image of 85.27 was achieved with a standard derivation of 2.823 for 2702 in-field measurements. Using the images captured in parallel to the laser characterization seen in figure 4.9 the linearity could be confirmed for unsaturated pixels above the

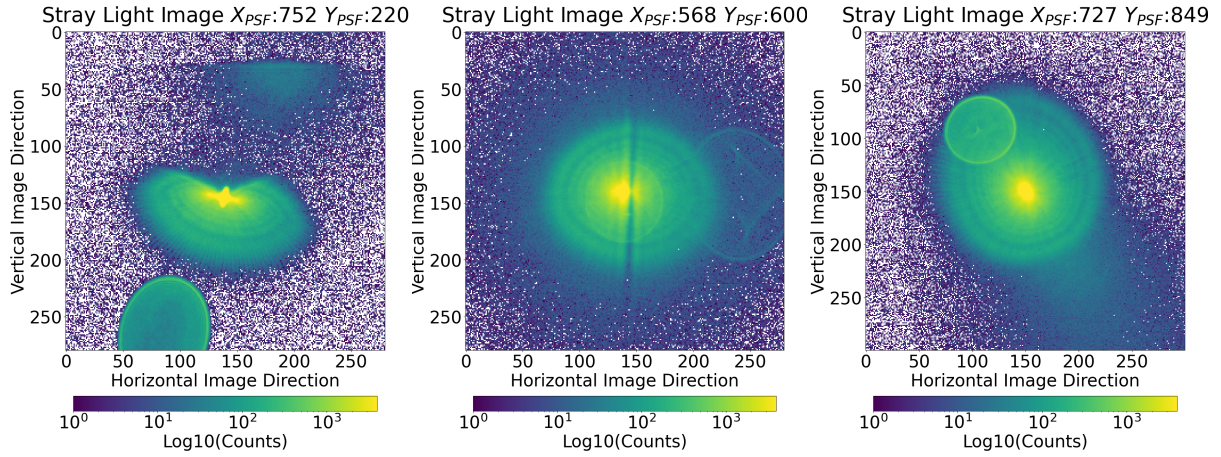


**Figure 5.4:** Typical stray light artefacts measured across the FOV. **Left:** The strong stray light artefact around the PSF becomes asymmetric in the upper edges of the image. **Middle:** The ghost overlaps the PSF and a higher order ghost becomes visible with the barber pole strongly modulated. **Right:** Strong stray light artefacts surrounding the PSF overlap with ghost artefact.

laser threshold. As a result, saturated pixels in the stray light images were linearly extrapolated based on the PSF values and power gain.

Figure 5.4 shows typical stray light artifacts for three different point source positions. A strong stray light artifact with a diameter of about 150 pixels surrounding the PSF is visible for all positions. All in-field measurements show a strong elliptical ghost pointing towards the center of the image. The ghost shows no diffuse stray light beyond its boundaries. The highest energy of the ghost is located at its edges, with a sharp decrease in irradiance beyond the edges to almost zero. As the distance of the PSF from the center of the image increases, so does the distance of the ghost to the PSF. At the center of the image, the first-order ghost overlaps with the PSF, and another ghost becomes visible. The vertical stripe indicates the barber's pole. All images show a diffuse stray light pointing against the image center direction. The parameters for the BSL evaluation are based on a first qualitative stray light estimation. The background parameter  $a_{background} = 150$  pixels was chosen to include all visible stray light artifacts. A signal area of  $a_{signal} = 40$  pixels was chosen based on the spatial resolution requirements of the mission. Figure 5.5 shows the results of the BSL evaluation of all in-field angles. Measurements that could not be evaluated are indicated with grey pixels.

At the lower end of the image, the stray light increases significantly and shows two high intensity areas with up to 40% stray light. The average BSL for the entire FOV is 23.61%. The smooth

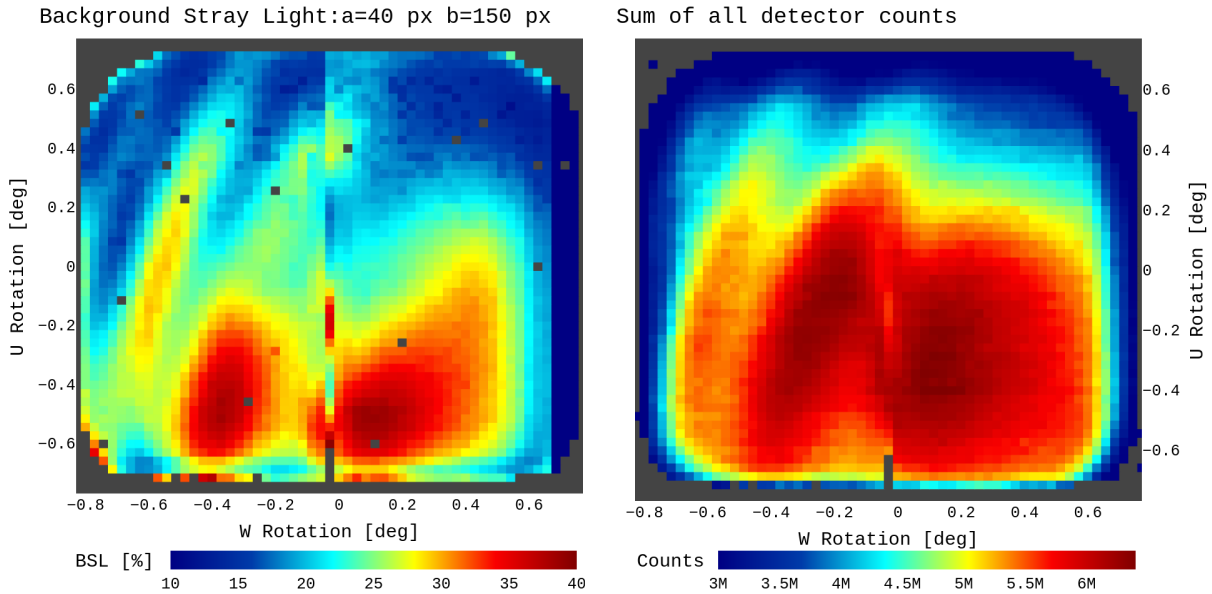


**Figure 5.5:** **Left:** Background Stray Light (BSL) provides stray light sources with a high spatial resolution across the detector. There are two regions in the lower image area with high BSL values. **Right:** The sum of all detector counts suggests that light in the upper image area is scattered in the instrument and therefore does not reach the detector.

transitions are an indicator of the high spatial resolution of the evaluation method and measurement setup developed. Comparing the BSL values with the sum of all detector pixels across different field angles reveals a clear relationship. In the upper area, less scattered light reaches the detector due to the stray light kernel becoming shadowed and asymmetric. In particular, the slotted lens mounts, which were tested for the first time in these experiments, are suspected of producing a non-round aperture and thus leading to increased diffraction. A simple diffraction simulation has shown that similar stray light artefacts around the signal can be produced by slotted apertures. The median stray light kernels across the FOV for the vertical and horizontal image directions are shown in figure A.17, demonstrating the low decay of stray light levels.

### 5.3.2 FIRST ORDER GHOST

To distinguish the main ghost from the remaining stray light artefacts, these were segmented using conventional image processing techniques. As the ghost has a high gradient to the background, a gradient image of the background section was first created and all values below an iteratively chosen threshold of 175 were set to zero, as these values gave the best results for segmenting the ghost arte-

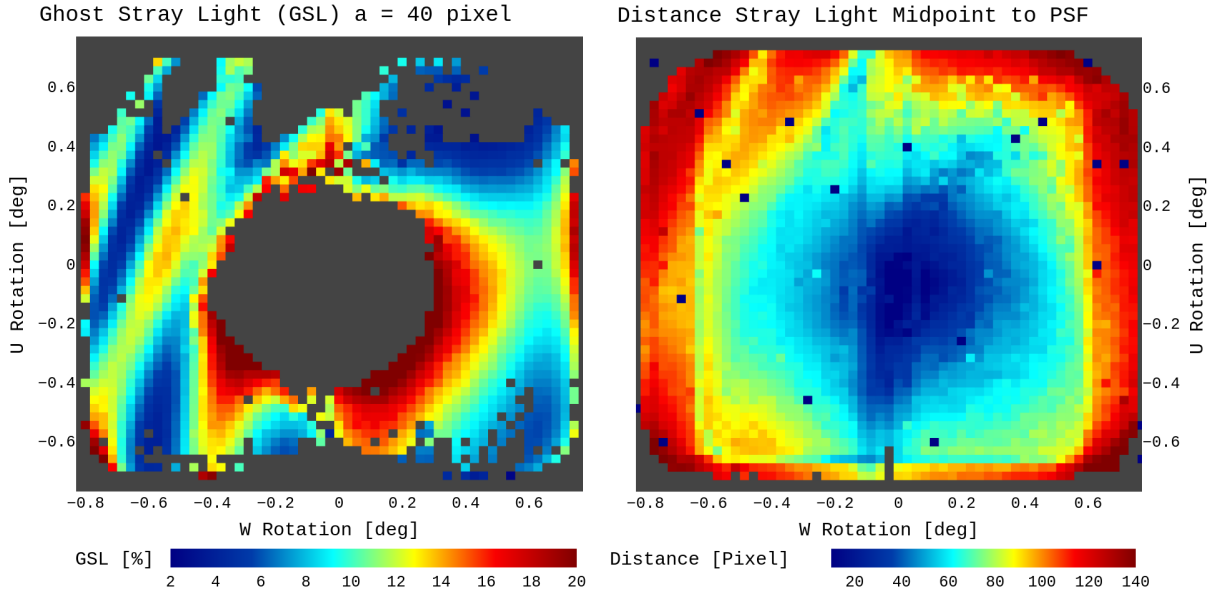


**Figure 5.6:** **Left:** The GSL distribution shows the high variation of the ghost artefact across the FOV. **Right:** The distance between the midpoint of stray light counts relative to the PSF decreases toward the image center. The sudden step in the distance can be explained by a sudden increase of stray light at the edge of the detector, which moves the center of the stray light counts.

facts. The new centre of gravity for all gradients was then sought within this new gradient image. A canny edge detection was then applied to this image section in order to capture contiguous edges within the image. This was then used to fit a 2D ellipse to the ghost and thus isolate the ghost from further stray light artefacts. As the ghost in the centre of the image overlaps with the signal, both cannot be separated using the described evaluation.

Figure 5.6 reveals ghost ratio in relation to the signal area used in the previous BSL evaluation. As with many other imaging systems with round apertures, ghosts from point sources appear as circular artefacts with the energy shifted to the boundaries. The ghost are filtered for distances  $d_{Ghost}$  to the signal larger than 60 pixel to avoid the overlap between the stray light surrounding the signal. The distribution correlations with the BSL evaluation by stripe patterns on the left side of the image. The median Ghost Stray Light (GSL) is 9.98% in relation to  $a_{signal} = 40$  as defined by equation 5.3. Due to the high variability of the ghost shape and GSL between 4% to 20%, it was not possible to determine a parameter set that could isolate the artefact at each field angle. As a result, there is no evaluation of the upper part of the image, even if a ghost image is visible in the image data. The distance of the stray light midpoint to the signal shows an increase from the center of the image to the edges up to

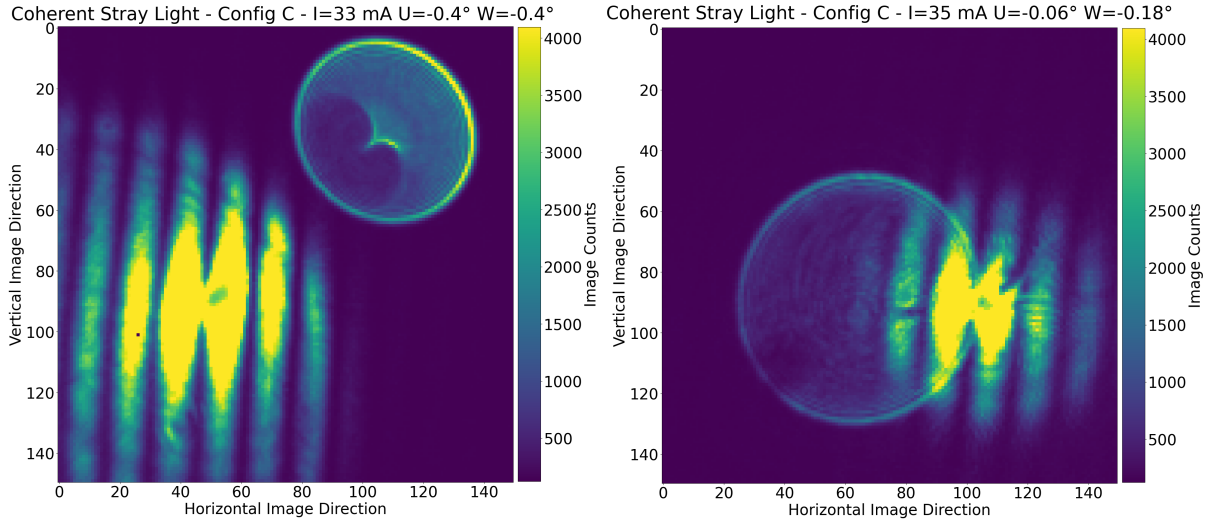


**Figure 5.7:** **Left:** The ghost artefact shows a high variation in intensity. **Right:** The ghost distance to the signal peak decreases toward the image center. Ghost detection next to the barber's pole shows processing artefacts.

a value of 140 pixels. The distribution is almost symmetrical around the image center. At an angle of approximately  $\pm 0.6$  degrees, the right, left, and lower sides of the image exhibit a sudden change in distance. This can be explained by a sudden increase in stray light at the edge of the detector and a deformation of the ghost artifact that shifts the center of the stray light counts, making the ghost less dominant.

$$GSL_{FirstOrder}(a_{Signal}, d_{Ghost}, a_{Ghost}) = \frac{\sum_0^{a_{ghost}} J}{\sum_0^{a_{Signal}} i} \quad (5.3)$$

The ghost artifact's symmetrical shape and strong descent of scattering across ring shaped boundaries indicate low diffuse scattering and aperture diffractions between the diffraction gratings, beam splitter, camera optics, and detector. Contrary to what is expected from the equation 3.20, the two ghosts reflected by the gratings cannot be spatially separated and appear as a single ghost across the FOV. Figure 5.7 shows ghosts for two different field angles of the coherent illumination just above the laser threshold. The figure demonstrates interferences of the stray light artefact surrounding the PSF but no interferences of the ghost is visible. To simplify ghost detection, the analysis is performed just below the laser threshold. Figure A.13 shows the complexity of higher order ghost artifacts and stray light interference at 43 and 44 mA laser current.

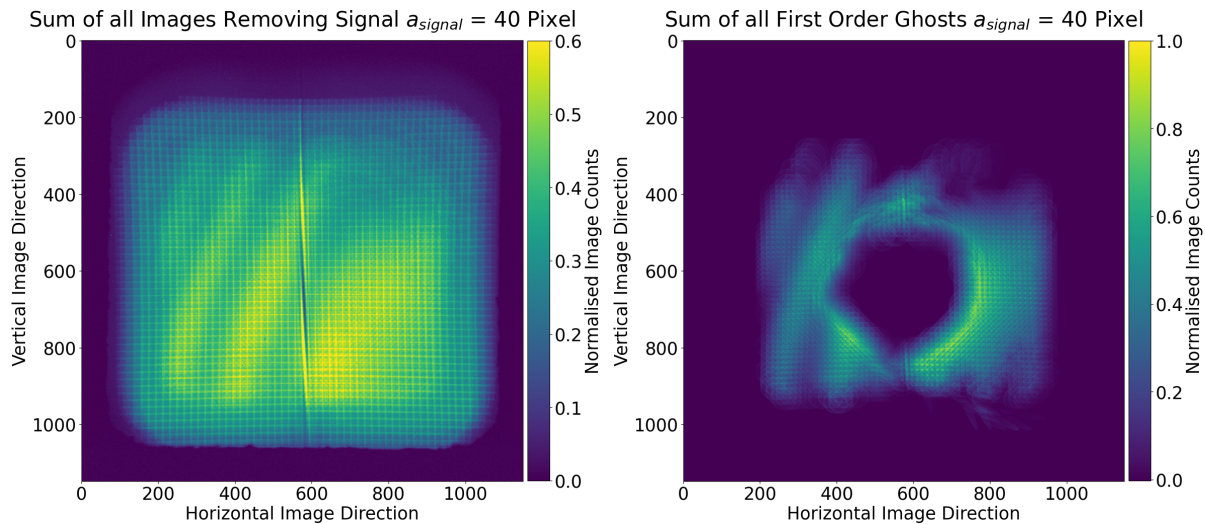


**Figure 5.8:** **Left:** The summation of all images, excluding the signal area utilized for BSL estimation, reveals the profound impact of ghosting on the overall in-field stray light. **Right:** The second-order image can be generated by the sum of the isolated ghost images, which correlates with the visibility distributions.

### 5.3.3 STRAY LIGHT IRRADIANCE DISTRIBUTION

In order to obtain an overall picture of the stray light sinks, the resulting distribution of the stray light irradiance was determined on the basis of BSL measurements. Figure 5.8 shows the normalised sum of all stray light images, with the signal area set to zero for each measurement.

Combining only the segmented ghost artifacts from each stray light image shows that the modulation is mainly caused by the first-order ghosts. The reconstructed images clearly show that the strong stray light modulation visible in the BSL data results in an approximately 70% narrowed second image concentrated in the center, overlapping the first order image. A comparison with the visibility heatmap suggests a correlation in the distribution. Figure A.3 shows that the overall visibility increases, but the distribution remains consistent across wavelengths. The modulation of the visibility is correlated with the irradiance of the ghost artifact, which is the image of the GSL distribution. Further validation of this hypothesis is required because experiments with variable wavelength were not performed and the laser light source was operated just below the laser threshold at 30.0 mA with an ASE spectrum. However, since the stray light experiments were performed with a broadband light source, temporal coherence leading to the distribution can be ruled out.

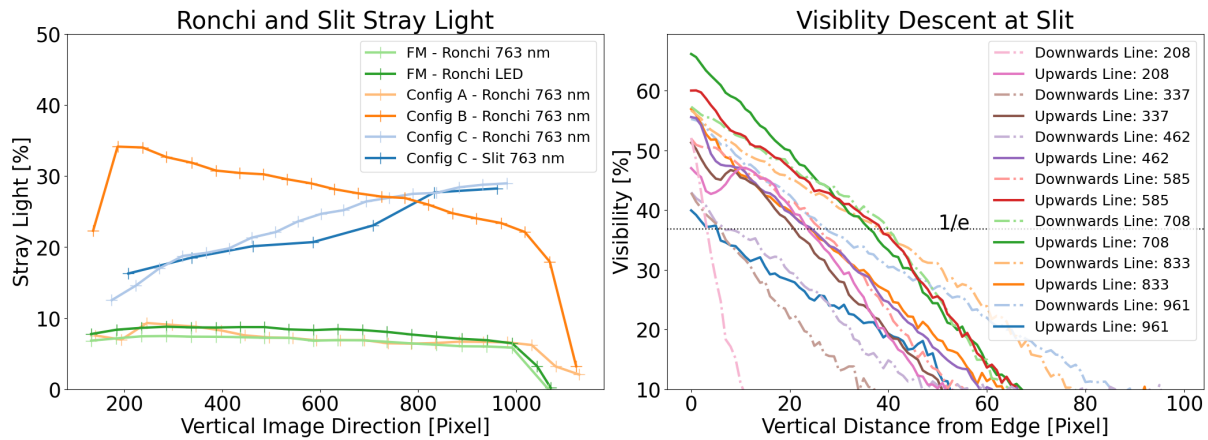


**Figure 5.9:** Left: Ronchi Stray Light and Slit Stray Light values in vertical direction compared for various instrument configurations. Right: Visibility Descent at the slit for configuration C. The length of temporal coherence is defined as the point where visibility reaches  $1/e$ .

### 5.3.4 RONCHI RULING AND SLIT

To measure the integrated stray light over the entire FOV, the Ronchi ruling was imaged in the horizontal direction. Unlike the Point Source Mapping (PSM) experiments, data are available for different front optic settings and for the flight model. The processing and measurement of Ronchi ruling data is much simpler than PSM. By averaging the image in the horizontal direction, the minimum shadowed and maximum illuminated lines can be detected automatically using peak detection with a fixed peak spacing given by the number of visible Ronchi stripes. The total number of counts in the detected shadow line relative to the two surrounding illuminated maximum lines provides the Ronchi Stray Light (RSL) for that region of the image. Figure A.5 shows several Ronchi ruling images measured with the SHIPAS QM and FM instrument. Figure 5.9 gives an overview of the derived RSL values.

The RSL varies significantly depending on the configuration of the front optics. While for Configuration A a RSL between 3.2% to 9.32% and a mean of 6.89% can be determined, Configuration B leads to a RSL from 3.2% to 34.13% and a mean of 26.47%. The Configuration C that was used for the PSM experiments, reveals a RSL ranging from 12.52% to 28.96% and a mean of 22.96%. The first Ronchi experiments 2 months before the main stray light experiments show similar values to configuration A. The FM shows the best mean RSL with 6.5 % at 763 nm and 7.4 % with the NIR

LED. The LED measurements reveal a constant offset of about 1% to the Laser measurements. To investigate the stray light wavelength dependence, 6 Ronchi ruling measurements were performed using 760 to 765 nm and the NIR LED. As can be seen in Figure 5.11, the RSL remains almost constant for the different wavelengths in the vertical direction. The comparison between Slit Stray Light and Ronchi Stray Light for Config C shows a similar trend with the largest deviations of up to 4% in the center of the image. This is to be expected as the ghost falls back on the slit and cannot be measured as stray light for the center of the image. The slit signal region is separated from the stray light region at the highest edge gradients. Simultaneously, the Ronchi ruling NIR LED data provides an ideal target for estimating the MTF in the vertical direction of the entire FOV as can be seen in figure 5.10. As already determined in the PSM measurements in Figure A, the spatial resolution decreases significantly towards the upper image area. The highest spatial resolution is located below the image center at line 700 with a slight drop towards the lower imager. It should be noted that this is the overall system MTF, including the instrument to be calibrated and the mACU. To determine the effect on visibility, the isolated MTF of the camera optics resolving the interferogram is required. In comparison, the MTF measurements with the final FM in figure A.4 show the high spatial resolution that can be achieved over the entire FOV.

Since the Ronchi pattern preserves spectral information in the horizontal direction, the visibility of the shadowed stripes is an integral measure of the modulation of stray light. The higher the modulation of the stray light, the greater its effect on the spectral stray light. The descent of visibility at the different edge positions presented in Figure A.7 indicates an almost constant gradient for all edge positions and sides, with a mean descent of about -1% per pixel for Config C. The images for the various slit position can be found in figure 6.1. Figure 5.11 indicates that the descent in visibility towards the shadowed lines decline towards higher wavelengths. The signal visibility and shadowed increases towards higher wavelengths and with less variability across the vertical direction. The interferogram starts to rotate near the Littrow wavelength at 765 nm, so the data is no longer representative.

Figure 5.11 represents the visibility in the illuminated and shadowed regions for various instruments and configurations. The stray light intensive configuration C shows a minor reduction in

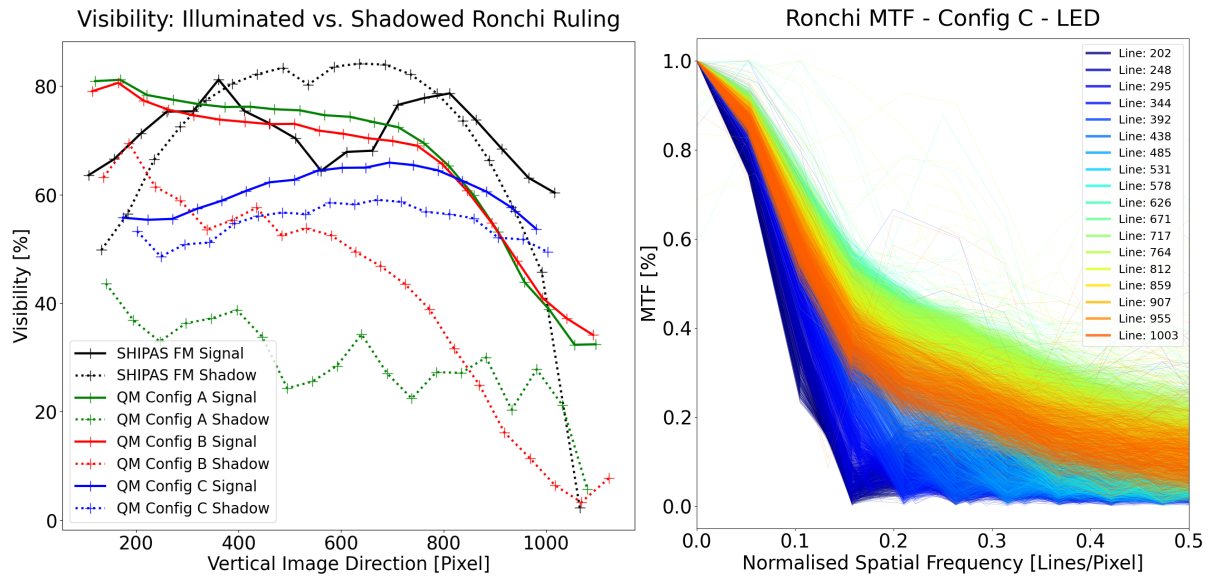


**Figure 5.10: Left:** The ratio of visibility in the illuminated and shadowed regions is highly dependent on the instrument configuration. Configuration A shows the lowest stray light visibility. **Right:** The MTF measurements for each edge and vertical cross section are plotted on top of each other without any filtering.

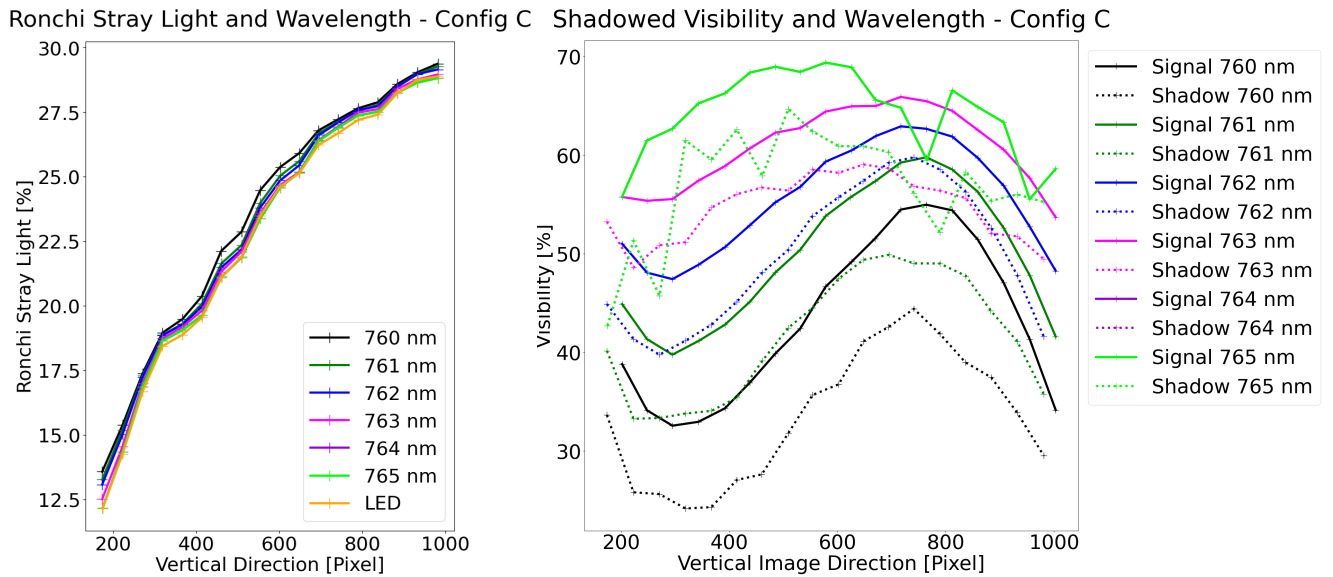


**Figure 5.11: Left:** For configuration C the stray light distribution in vertical direction is almost constant for different wavelengths. **Right:** The visibility descent is reduced towards higher wavelengths.

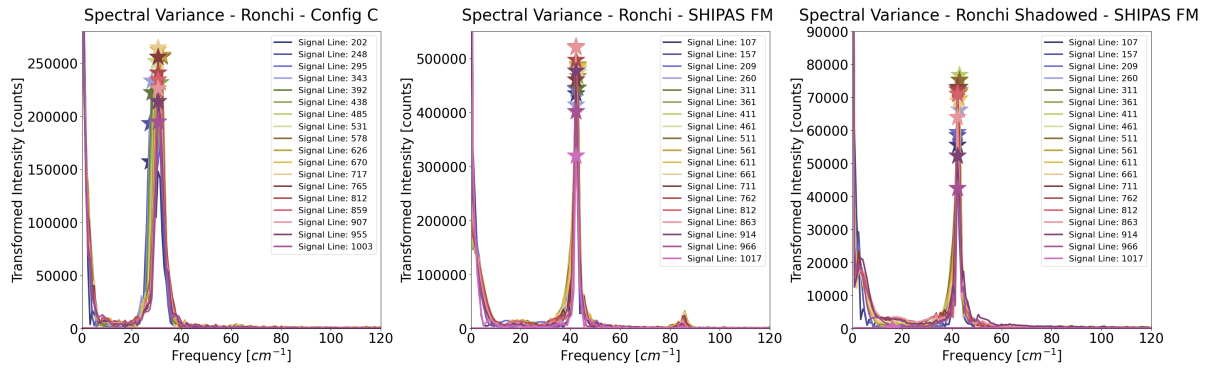


**Figure 5.12:** The spectral variance of the FM is lower compared to Config C, but the harmonic frequencies are visible in the illuminated area of the Ronchi ruling. The shadowed areas do not show these harmonics.

visibility in the shadowed stripes. Stray light is therefore largely included in the spectral information. The low stray light configuration A shows a significant reduction in mean visibility of 38.14% at the shadowed regions. Although the FM provides the highest visibility, the shadowed visibility is significantly higher compared to Config A. The slit measurements done for Config A also reveal a rapid visibility descent as can be seen in figure 5.9. The shadowed visibility of the FM is prominent, as it is higher than the signal visibility, particularly in the middle of the image. A direct examination of the raw data shows that the minimum stray light is not located in the center of the shadow stripes, but is directed to the upper part of the shadow stripes. The comparison between the FM Ronchi spectral variance to previous instruments can be seen in figure A.6. The variance drops from  $2.2470$  to  $0.1730 \text{ cm}^{-1}$  between Config C and FM. The mean FWHM decreases from  $5.209$  to  $0.842 \text{ cm}^{-1}$ . However, the spectrum shows spectral stray light of about 7% peak ratio at exactly twice the main peak frequency as can be seen in figure 5.12. Such an artefact has never been observed with previous instruments and configurations. However, this artifact cannot be observed in the shadowed areas.

The Ronchi ruling measurement has also been used to test various deconvolution measurements by using a single PSF to deconvolve the entire image. Therefore, the Richard Lucy deconvolution and the unsupervised and supervised Wiener deconvolution provided by the scikit-image<sup>73</sup> package were tested on the central part of the image. Figure A.16 illustrates the spectrum of the superimposed interferogram of 762 and 759.5 nm before and after the unsupervised Wiener deconvolution. The peak relation between both signal amplitudes could not be preserved after the deconvolution and the

amplitudes are increased in the shadowed and illuminated regions. Also the noise in the spectrum is slightly increased as it is expected by the deconvolution. No further investigations were carried out to further analyse this hypothesis. Using a PSF kernel larger than the shortest interferogram period of 10 pixels will cause harmonic frequency artifacts in the spectrum at higher frequencies. Such behavior is to be expected, as a literature research has shown, since the PSF is defined only for incoherent light. Since the PSF is measured below the laser threshold, it is measured incoherently in time, unlike the Ronchi images. The coherent transfer function is unknown for these measurements, so no deconvolution can be performed for the coherent case. However, initial experiments with a stronger attenuation of the laser power have shown that a coherent PSF can be resolved, which includes the modulation of the interferogram.

## 5.4 OUT-OF-FIELD STRAY LIGHT

### 5.4.1 POINT SOURCE TRANSMITTANCE

To measure the Point Source Transmittance (PST), the total irradiance of the light source must be estimated when the LOS is directed at the center of the source. Since there is no radiometric calibration of the instruments for the flux at a laser power of 160 mA, the total image counts are extrapolated based on the images taken when the laser power is stepped at 1 mA. Because of the switch from the ASE spectrum to the laser spectrum at the laser threshold, the counts do not follow the power gradient linearly. It was therefore necessary to analyse the image background to determine the power increase at the laser threshold. A power gain factor of 1.35 was observed between the power meter reading and the power increase in the image background when transitioning from 31 to 32 mA. Above the laser threshold, the entire spectrum passes through the instrument's bandpass filter. The image background and power meter readings behaved linearly to each other above and below this point. The gradient above the laser threshold was therefore determined with  $18.53 \cdot 10^{12}$  image counts per watt in relation to the power meter measurements. This allows the total number of counts provided by the laser light source imaged in-field to be estimated at 160 mA.

The PST measurement is displayed in figure 5.13. The dataset was filtered for field angles that

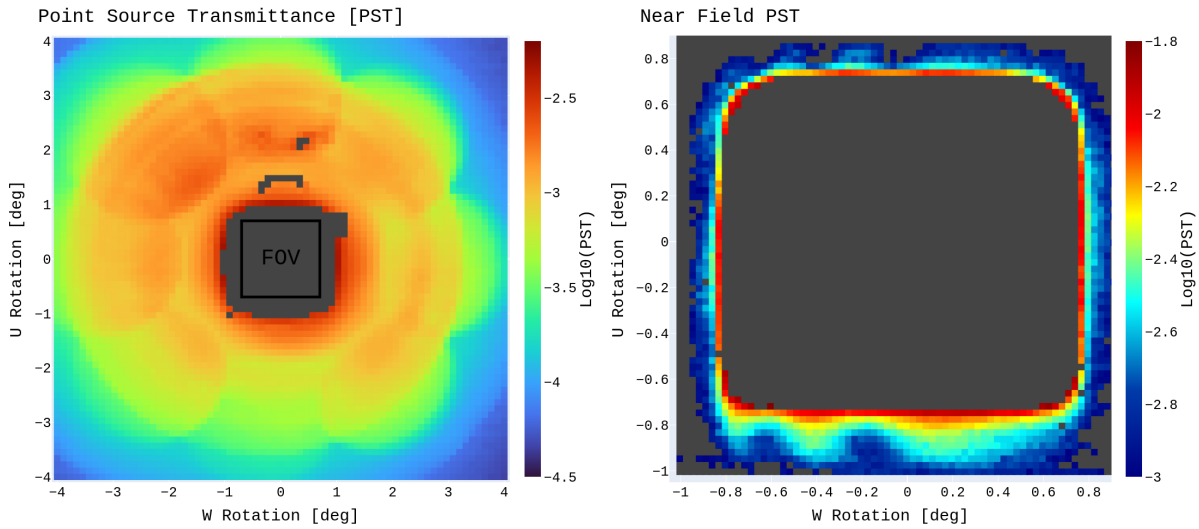


**Figure 5.13:** **Left:** Out-of-field stray light evaluated using Point Source Transmittance (PST). Since the measurements were taken at full laser power, the stray light image next to the FOV shows saturated pixels and cannot be processed. **Right:** The PST measurement shows a sudden drop in near-field stray light, except in the lower part of the image.

exhibited saturated stray light images near the FOV and in two hotspots at  $U = 1.3$  deg and  $U = 2.0$  deg. At  $W = -4.0$  deg and  $U = 0.0$  deg the PST value dropped to  $-3.77$ . This corresponds to the order of magnitude of the analytical estimates in figure 3.17. In addition to a circular stray light distribution symmetrical around the FOV, 8 circular areas show increased stray light values that do not correspond to the constant decrease in stray light predicted by the analytical model. The centers of the circles are symmetrical at an angle of approx. 3 deg and show a radius of approx. 1 deg. At positive angles  $U$  the PST values are significantly higher than at negative angles. The side facing the surface will therefore have less out-of-field suppression than the side facing space. Validation with out-of-field slit measurements is not possible due to the high power losses in the integration sphere and the resulting insufficient irradiance combined with the short integration time of 200 ms.

Since the instrument reflects approx. 50% of the incident power back to the mACU, it is necessary to assess whether the returning power is causing further scattering at the mACU that is reflected back into the instrument. To investigate this, the mACU was moved from 12.5 cm to 20.9 cm between the first aperture surface of the baffle and the first mACU aperture surface of the lens holder. It can be assumed that backscattered stray light distributions from surfaces that are not plane-parallel to the optical axis are visible by a spatial shift. As a result, stray light bias caused by mACU backscatter is

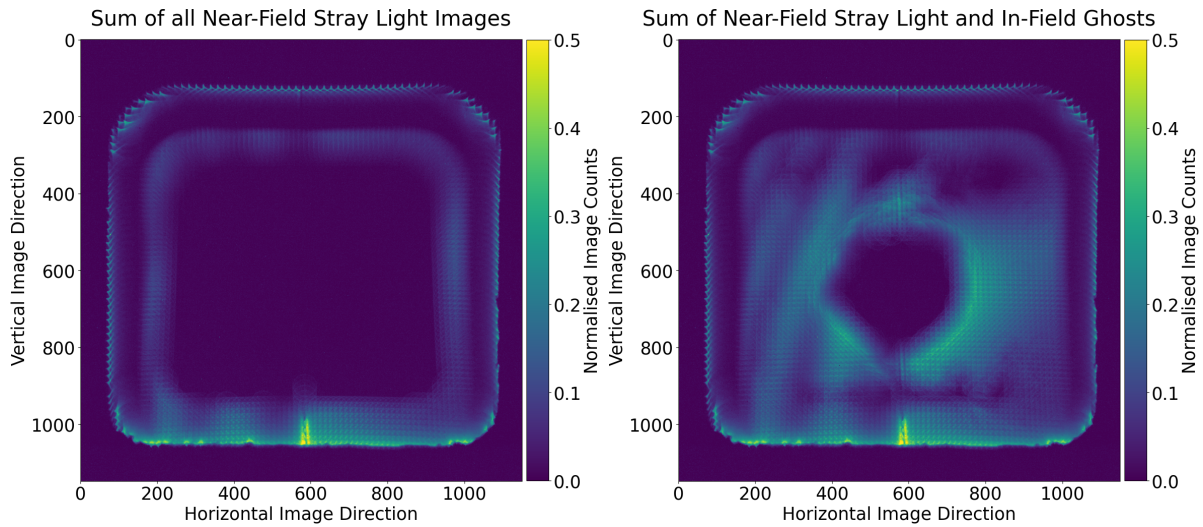


**Figure 5.14:** **Left:** The sum of all near-field stray light images. The elevated radiation levels at the lower end of the detector have a minimal impact, as they are concentrated at the detector's edge. However, the in-field ghost shows a transition into the near-field region. **Right:** Combining the far-field and near-field ghosts yields the extent of the entire second-order image.

a function of distance relative to the instrument. Figure A.8 shows that opening and closing of the rail carrier causes angular misalignment of the mACU. Although a quantitative comparison is not possible due to changes in several parameters of the experimental setup, the overall PST distribution appears to be similar.

In order to evaluate the near field stray light, the in-field stray light data exceeding the FOV was evaluated as shown in the figure 5.13. Apart from the lower side of the image, there is a sharp decrease in PST beyond the FOV, consistently overlapping with the out-of-field measurement with a PSF of approximately -2.9 at an angle of about 1 deg. The bottom side exhibits an elevated PST of -2.5 at a field angle  $U$  of -0.91 deg compared to the other sides. The sum of all near-field stray light images is presented in figure 5.14, which illustrates that the highest near-field stray light irradiance occurs predominantly at the very bottom edge of the detector. The first-order ghost artifact, which has already been observed in the field, can still be detected in the near-field range. In particular, in the lower part of the image, the ghost is clearly visible reaching far into the near-field region, which causes the low decrease in PST.

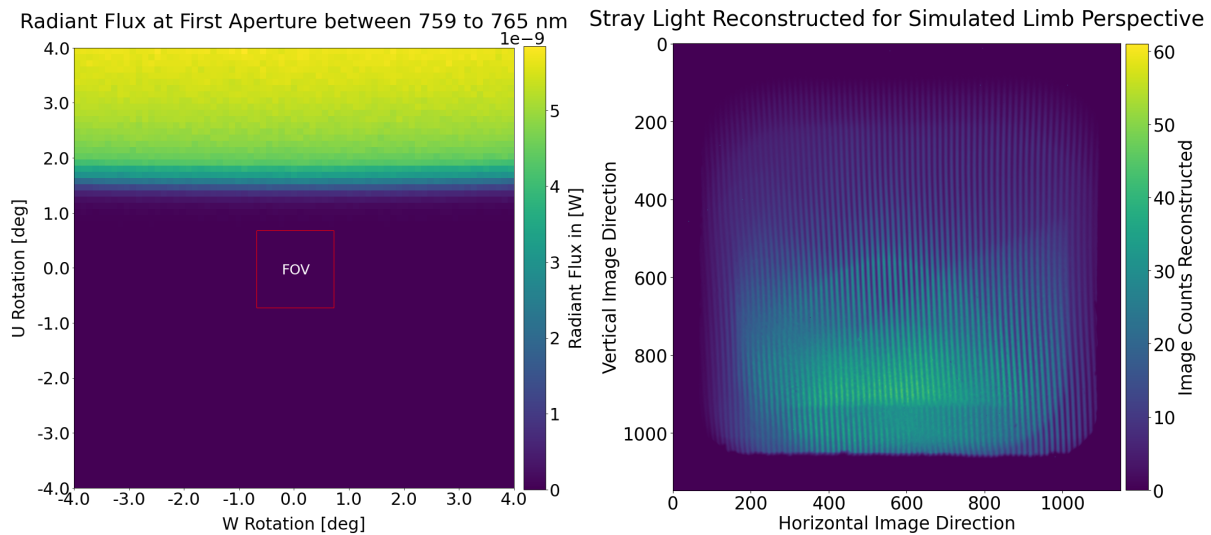


**Figure 5.15:** **Left:** A radiative transfer simulation was conducted using Eradiate with the same grid size as the PST measurements. The LOS was oriented at an altitude of 90 km with the sun at zenith. **Right:** The reconstructed out-of-field stray light image was scaled by the power used for the PST measurement and the radiance from different directions at the baffle aperture, which was obtained through radiative transfer simulation.

#### 5.4.2 IN-ORBIT OUT-OF-FIELD STRAY LIGHT

PST measurements can be combined with irradiance estimates from radiative transfer models to derive out-of-field stray light for different orbital geometries and positions of the Sun and Moon. As the Earth’s reflectivity is highly dependent on the cloud distribution, the 3D radiative transfer model Eradiate<sup>126</sup> was used for its ability to simulate complex 3D scenarios for Earth observation applications. To illustrate the use of PST measurements for orbital stray light estimation, a simple case with the Sun at zenith and a homogeneous Earth albedo of 0.3 is simulated using a cloud-free standard atmosphere AFGL’s 1986<sup>127</sup> from 0-120 km, including absorption and scattering but without  $O_2$  emissions. For the simulated perspective parameter defined in the table 3.2, the simulated radiance is used to estimate the irradiance by the equation 3.27 for the same grid size as the PST measurements. The simulation has been performed from 759 nm to 765 nm with a resolution of 1 nm. The radiative transfer simulation is run for each grid cell, producing a 2D image of the incoming irradiance from the Earth. Direct sunlight is not been covered by this simulation.

Figure 5.15 shows the simulated radiance at the extended perspective used for the PST evaluation, relative to the inner FOV. The estimated in-orbit radiant power at the baffle aperture can be related

to the power meter readings from the PST measurements and the fiber split ratio to scale each individual stray light image according to the atmospheric irradiance. The stray light images in figure 5.15 show the reconstructed in-orbit out-of-field stray light image. Although the interferogram does not correspond to the absorption spectrum as shown in Figure 3.17, the laser light sources can be used to estimate the distribution of the detector stray light irradiance and visibility. The reconstructed image clearly shows the lower edge of the 2<sup>nd</sup> order image created by the ghost artefact. Visibility and the mean counts per line in the vertical direction are compared in figure 5.16. The counts are scaled linearly from the 200 ms integration time used for the PST measurements to an expected in-orbit integration time of 1 s for daytime airglow observations. The mean counts per second integration time over the entire FOV is 56.27 with a mean visibility of 38.14%. Assuming an average signal level of 3000 counts and a reduction of the signal level by the mean visibility, an out-of-field stray light of about 0.7% can be expected. The mean horizontal stray counts and the stray light visibility are inversely distributed. Although the mean stray light counts increase at higher altitudes, the visibility is only in the range of 20%. Therefore, stray light limits the possible dynamic range at higher altitudes, but the spectral information is only affected by about 20% visibility. At line 800, there is a drop in visibility of about 7%, as expected from in-field stray measurements, since the second-order image caused by the ghost ends here. The spectrum of the in-field compared to the out-of-field illumination can be seen in figure A.6. The data does not demonstrate any significant shifts in comparison to slit or Ronchi ruling measurements, with a variance of  $1.37 \text{ cm}^1$  and a mean FWHM of  $2.92 \text{ cm}^1$ .

To estimate the contribution of direct sunlight and moonlight to the in-orbit stray light, the violation of the  $\theta_{sun \text{ exclusion angle}} = 39.0 \text{ deg}$  is evaluated over a mission period of 1 year using the simulation described in section 5.5.1. The angle  $\theta_{sun}$  relative to the LOS is shown in figure 5.17 for orbital perspectives when the Earth does not block direct sunlight. In total, 5.31 % of the simulated perspectives show a violation, with 2.94 % attributable to the moon and 2.59 % to the sun. For 34 cases with a step size of 60 seconds, parts of the sun will be visible directly within the FOV.

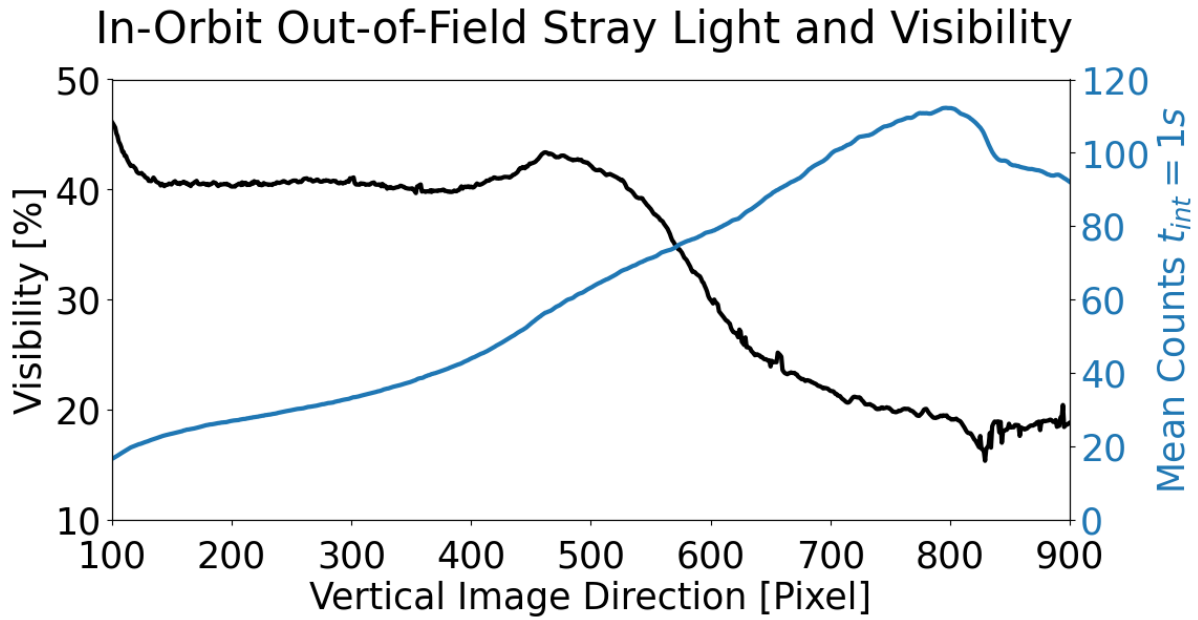


**Figure 5.16:** The out-of-field stray light image was reconstructed using PST measurements and a radiative transfer simulation for the sun at the Zenith. The plot shows the progress of stray light visibility and energy on different vertical regions.

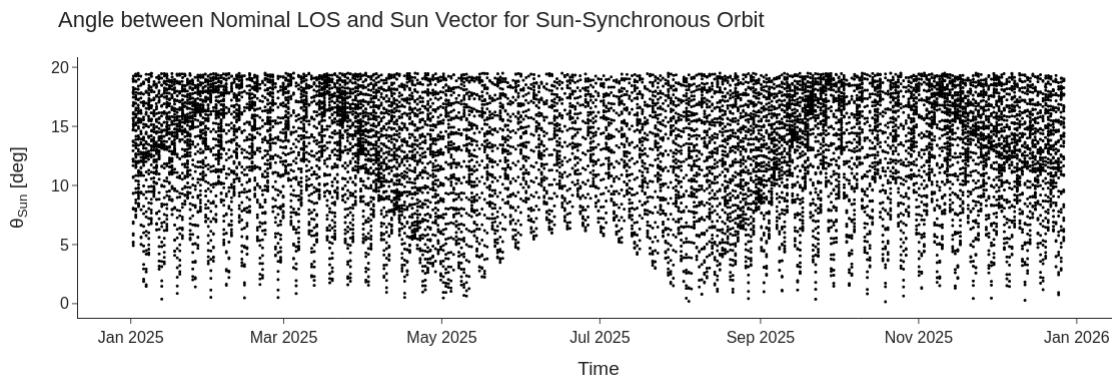


**Figure 5.17:** Angle between the LOS and the sun when it is not blocked by the Earth. The sun is regularly visible within the FOV.

### 5.4.3 STRAY LIGHT MEASUREMENT UNCERTAINTY AND ERROR

The measurement methods presented here are implemented for the first time and represent an innovative iteration process. It is therefore not possible to guarantee continuous traceability and reproducibility of the quantities presented. Despite extensive planning, it was not possible to quantify all relevant sources of measurement uncertainty and error in the execution and setup of measurements. However, on the given results, discussions within the instrument development team as well as literature research, the experiments provide the fundamental experience to increase traceability and reproducibility for future instruments. Despite an intensive literature search for publications, no methodology could be identified that could be applied to existing experimental setups. Even well-known literature on stray light provides very limited information on measurement errors. The lack of standardisation of stray light measurements themselves may be the underlying reason for this. The only industrial standard that could be found for the stray light measurement of spectral resolving instruments is defined for spectrophotometers.<sup>35</sup>

The Noise-equivalent power (NEP) is one detector characteristic that is stated relevant for error estimations of stray light.<sup>57</sup> It is defined as the signal power that gives a signal-to-noise ratio of one in a one hertz output bandwidth.<sup>128</sup> As previously discussed in Chapter 3.4, the dimensions of the detector, its inherent noise, and the number of pixels have a considerable impact on the uncertainty associated with stray light measurements, particularly when a point source is employed to ascertain the spatial distribution of stray light. If the NEP and stray light area is too large, the energy scattered onto the detector from a single point source cannot be detected when it is distributed over to many pixels. Accordingly, the BSL (see equation 3.18) was used instead of the TIFSL (see equation 3.19) to restrict the evaluated detector area to the background of the PSF peak. In order to evaluate the influence of uncertainties associated with detector noise on stray light measurements, the Stray Light to Noise Ratio (SLNR) is introduced. This is defined as the ratio of the stray light signal  $J$ , to the difference between the corresponding detector noise image  $N$ , and the median detector noise  $N_{median}$ <sup>40</sup>, as defined in equation 5.4:

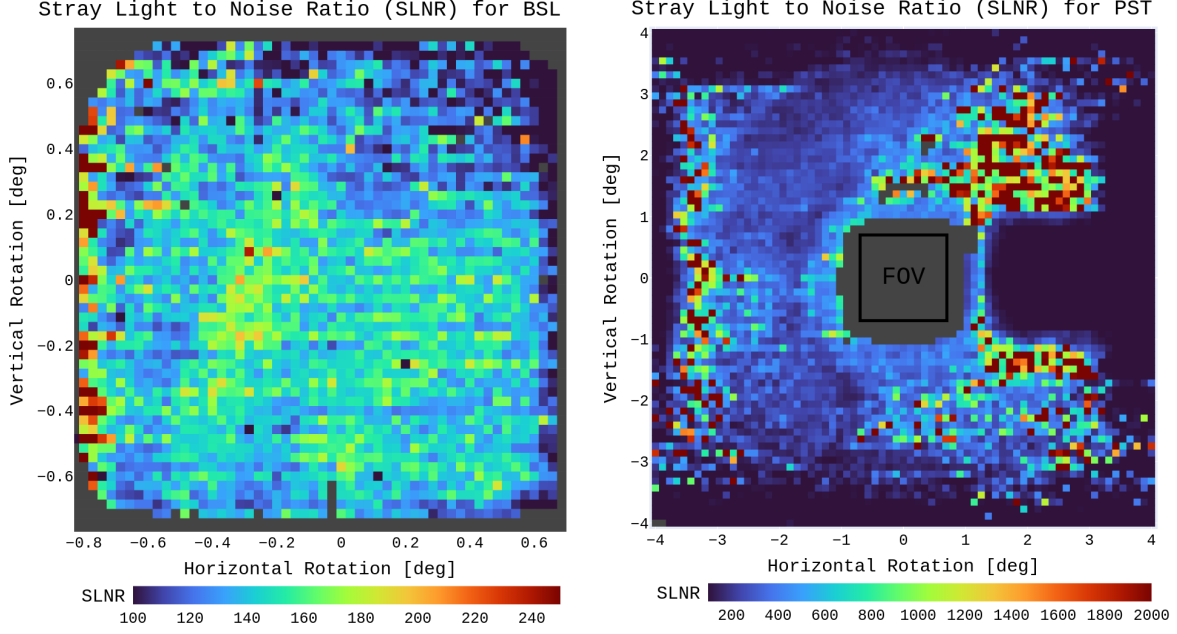


**Figure 5.18:** **Left:** The SLNR for the BSL demonstrates an even distribution around 150, with elevated values reaching up to 240 on the left side and a decline to 100 on the right side. **Right:** The SLNR for the PST measurements show a high correlation with total dark image energy illustrated in figure 5.1. One potential explanation for the elevated SLNR at the specified location and the accompanying artefact in the designated FOV is the median dark image employed for assessment, which is susceptible to the influence of discharge lag noise from preceding measurements.

$$SLNR(a_{Signal}, a_{Background}) = \frac{\sum_{a_{Signal}}^{a_{Background}} J - \sum_{a_{Signal}}^{a_{Background}} N_{median\ n}}{\left| \sum_{a_{Signal}}^{a_{Background}} N - \sum_{a_{Signal}}^{a_{Background}} N_{median\ n} \right|} \quad (5.4)$$

As median dark image of the last  $n = 40$  images is used for the BSL (Background Stray Light) and PST (Point Source Transmittance) noise subtraction, it is possible to determine the extent to which the stray light level fluctuates with respect to a single dark image taken shortly before the stray light measurement. Figure 5.18 illustrates the SLNR distribution for all Point Source Mapping (PSM) measurements. As expected, the SLNR decreases with higher angles relative to the FOV as the stray light signal decreases.

However, it becomes also clear that the discharging lag noise has a significant effect on the SLNR, as can be seen for positive horizontal rotations next to the FOV. When the hexapod moves back from +4 degrees to -4 degrees, the laser is turned off for more than 1 minute. This also affects the median noise level in relation to the current noise level. Notwithstanding the considerable influence of dis-

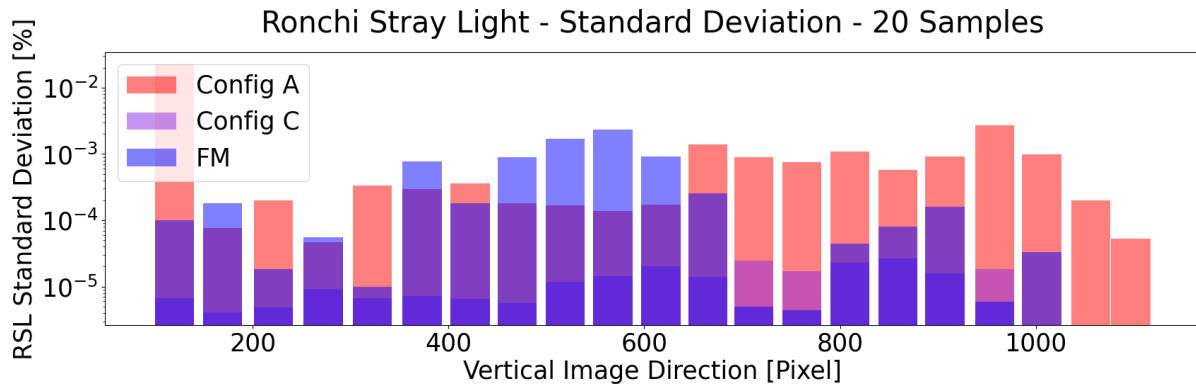


Figure 5.19: The standard deviation of the individual Ronchi Ruling images demonstrates accurate measurement behaviour.

charging lag noise, the median SLNR for the PST measurement is observed to be 226.3. Only at the outer regions the SLNR drops to a minimum of 20. In contrast, the SLNR of the BSL measurements exhibit no discernible pattern in their distribution, with a median SLNR value of 147.11 and a minimum SLNR of 13.4.

In the Ronchi Stray Light experiment, each measurement was evaluated using a median of 20 consecutive images, with the parameters of the experimental setup remaining unchanged. Consequently, it is possible to evaluate the standard deviation as a value for the uncertainty by evaluating each individual image with the same data processing. As can be seen in Figure 5.19, the standard deviation between all measurements remains very low. Apart from a single outlier, the RSL standard deviation remains below 0.003 %. The outlier of the first visible Ronchi stripe with a standard deviation of 0.0149 % is caused by peak detection, as low signal levels reduce the robustness of the peak detection used to identify signal and shadowed lines. As the signal and shadow lines for evaluation are evaluated independently for every image, a shift in peak detection will cause a shift in the stray light levels.

In the absence of a sink or source with known stray light quantities traceable to the International System of Units (SI), it is not possible to evaluate any systematic errors in the measurements. Only the residual to the simulation can be evaluated. Table 6.1 presents the varying stray light levels from the simulation and the measurements. The first order ghost was evaluated by the simple analytical model with 9.98 % GSL and by the measurement with 10.05 % showing a residual of 0.07 %. Also, Ronchi

Ruling measurements and Slit measurements for the same instrument condition are less than 1% apart. However, the stray light measurements presented always include measurements of the overall system consisting of the mACU and the instrument. Scattering that originates at the optics of the mACU or from the point light source itself can only be compared to the reference telescope, but cannot be quantified absolutely to a SI traceable standard. The only way to validate such stray light measurements is therefore to observe astronomical targets after launch, as the optical conditions of light sources like the moon are known with high precision and accuracy.

## 5.5 IN-ORBIT VALIDATION AND RECALIBRATION METHODS

In order to validate the laboratory experiments for the characterization of the stray light and the spatial resolution in orbit, additional simulations as well as practical experiments were developed. The methods and values presented are only exemplary, as detailed orbital parameters are not known at the time of writing. The use of stars or planets as validation light sources is challenging due to the reduction in light intensity caused by the narrow band filter. Without an accurate knowledge of the instrument's LOS relative to the satellite's coordinate system, it is not possible to accurately point at any star target. Correcting the LOS is therefore the first step required for all subsequent validation methods. However, it must also be assumed that the error in the LOS (Line of Sight) calibration is greater than the FOV, so any target that the instrument is pointing at may not be visible. The use of a low irradiance target for the initial LOS correction would be associated with high uncertainties due to the unknown region of space observed and the significantly longer exposure times required. Therefore, a broadband light source with high irradiance is required that can still be imaged directly without saturating large portions of the image. The only light source visible from an Earth orbit that provides this is the lunar surface. With an angular extent of about 0.5 deg, parts of the lunar surface should still be visible in the FOV in a range of about  $\pm 1$  deg under full moon conditions. Even if the lunar disk is not imaged directly, the near-field stray light should be detectable to roughly estimate the position of the moon. Another unique advantage offered by the moon are rotational features to determine the roll angle of the instrument around the LOS. Correcting the roll angle of the instrument

relative to the horizontal image direction is critical. Without this correction, vertical or horizontal motions relative to the estimated LOS do not correspond to vertical or horizontal motions relative to the image axes. To reduce the bandwidth required for data transmission from the satellite to the ground station, the horizontal rows of the image are binned in the vertical image direction. Therefore, without LOS roll correction, there would be a blending of vertical spatial information and horizontal spectral information in the raw data received on the ground.

### 5.5.1 MOON OBSERVATION MANEUVER

To forecast possible lunar observations, the SHIPAS satellite mission was simulated using SENTINEL-5P as an example, since both missions use similar sun-synchronised orbits with an inclination of 98.7 deg and an orbital period of 101.4 min. The orientation of the instrument is estimated using the parameters of table 3.2. The LOS points at an altitude of 90 km with an angle of 208.9 deg rotated around  $Y_{LVLH}$  relative to  $X_{LVLH}$ . The instrument is therefore aligned against the direction of the flight vector and pitched 26.1 degrees towards the earth. This perspective has been simulated using Skyfield, which combines the Simplified Perturbation Model SGP4, SPICE and the latest TLE data from CelesTrak. Using simulation time steps of 60s for each orbital position, a new LVLHs coordinate system and associated LOS have been estimated. Consequently, the angle between the LOS and any stellar target can be determined. This enables the calculation of the angle  $\theta_{source}$  between the LOS vector and any celestial light source. Due to the orientation of the satellite's solar panel and star tracker, there is a limit to the maximum rotation angle of the LOS for lunar observations. This value is dependent on the respective satellite mission and the operation of the satellite. It is assumed to be  $\theta_{max} = 45 \text{ deg}$  for further consideration. To determine the orientation of the crescent, the illumination of the moon surface is limited to a range between 20% and 80%. The target should also not be blocked by the earth. Assuming a one year satellite mission starting in January 2025, the angle between LOS and  $\theta_{Lunar}$  behaves as shown in figure 5.20.

With the given instrument perspective and a sun-synchronous orbit, moon observations are possible every month for a period of two weeks, within the specified limits. For 7 orbital situations, the

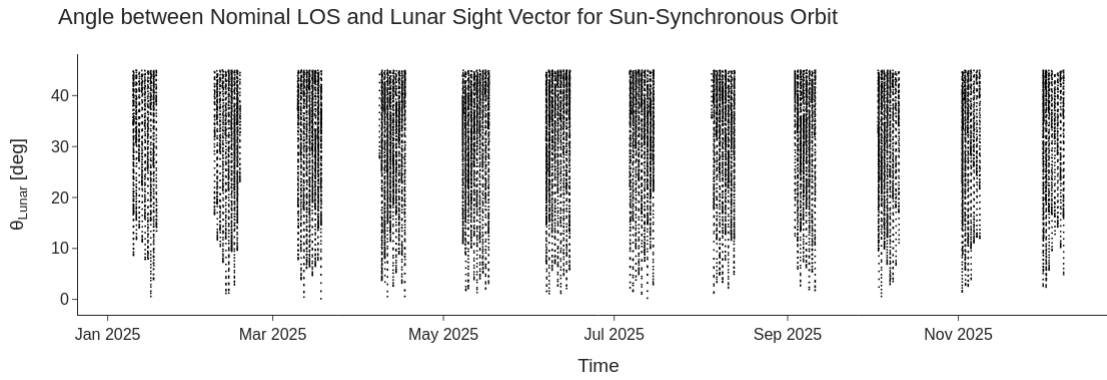


**Figure 5.20:** Angle between the LOS and the moon sight vector. Every 2 weeks the moon disk is visible near to the LOS of instrument without being blocked by the earth and illuminated between 20% and 80% to measure the tilt of the crescent.

simulated moon position was even visible within the FOV without changing the satellite attitude. Such moon transits allow drifts in instrument characteristics, such as LOS or spatial resolution, to be measured over the duration of the mission.

For precise determination of the moon vector relative to the LOS, the instrument is first aligned directly to the center of the celestial body. The LOS is then shifted four times so that one respective quadrant overlaps with the first image. This ensures that the moon surface is captured completely in at least one image over an angular range of  $\pm 2.8$  vertical and horizontal as can be seen in figure A.18. Initial ground-based moon observation experiments with the INSPIRESat 4 flight model have shown that 400 ms seconds of integration time provide up to 4000 counts in low gain mode for a moon phase of about 180 deg. Taking into account a lunar irradiance model like LIME<sup>129</sup> or MT2009<sup>130</sup> and the atmospheric absorption within instrument bandpass filter, the integration time for the in-orbit observation of different phases can be estimated via previous ground-based measurement. To accurately determine the orientation of the crescent, the detector is configured for full resolution using all detector pixels. The tilt angle corresponds to a rotation of the image around the LOS. This makes it possible to determine the tilt of the detector in relation to the earth's horizon.<sup>131</sup> The progression of the tilt angle over a period of 2 days is exemplary shown in Figure 5.21. Within one orbit the crescent turns by 360 deg relative to the local horizon of the satellite.

After correcting the LOS pitch, yaw and roll angles relative to the satellite coordinate system using the offset values derived from the moon images, the target is imaged a second time at the LOS

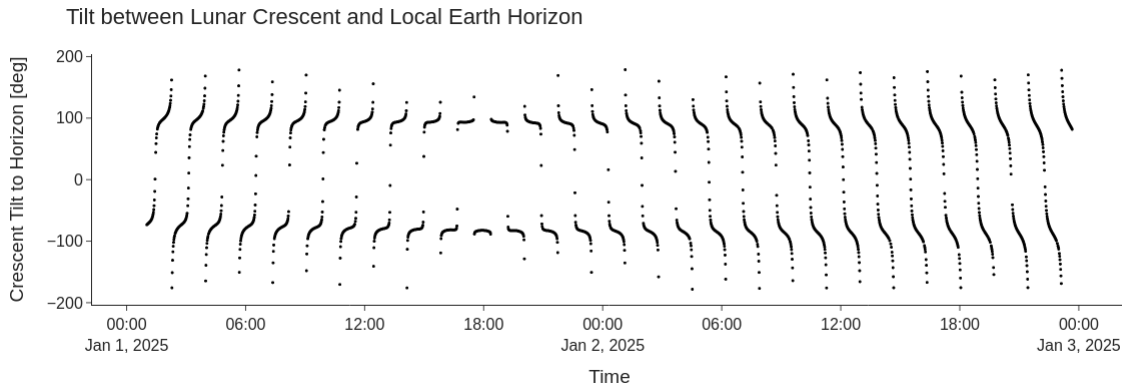


**Figure 5.21:** The tilt of the lunar crescent relative to local horizon changes according to the latitude of the satellite.

to validate the correction. To validate the corrected LOS, the moon disc is imaged along the corrected vertical and horizontal axes. Since these images can be used to derive the MTF/PSF and in-field stray light, the lunar disk should be off the operational LOS by half the sun exclusion angle to avoid airglow affecting the observation. Under ideal conditions, this image should be taken at an orbital position where the satellite itself is not in sunlight, which accounts for 48.52% of the possible observations.

After successful LOS calibration, the instrument is pointed at a dark region of deep space where the Sun's exclusion angle is not violated by the Earth's atmosphere, the Sun or the Moon. Under these conditions, dark images are taken for the expected operational integration times and the moon calibration integration times. Due to the high pitch angle required for satellite manoeuvring, which affects power supply from the solar panels, the number of possible dark images is limited. However, the images should ideally include all expected thermal conditions and detector configurations used for future measurements. To validate PST measurements in orbit, the moon disc is used as a light source. To ensure that the measurements are not affected by stray light from other sources, the moon vector should be displaced from the operational LOS by at least half the Sun Exclusion Angle and satellite should not be in sunlit. In the first step, the moon surface is mapped directly on the LOS. Then the moon surface is mapped with a  $\theta_{lunar}$  of  $\pm 4$  deg pitch and  $\pm 4$  deg yaw with a step size of 0.5 deg. To compare the lunar observations with a broadband extended light source in the laboratory, the semiconductor surface of a high power NIR LED was directly imaged as shown in figure A.14. Due to strong power fluctuations of the LED observed in unsaturated images, the lack of relative power

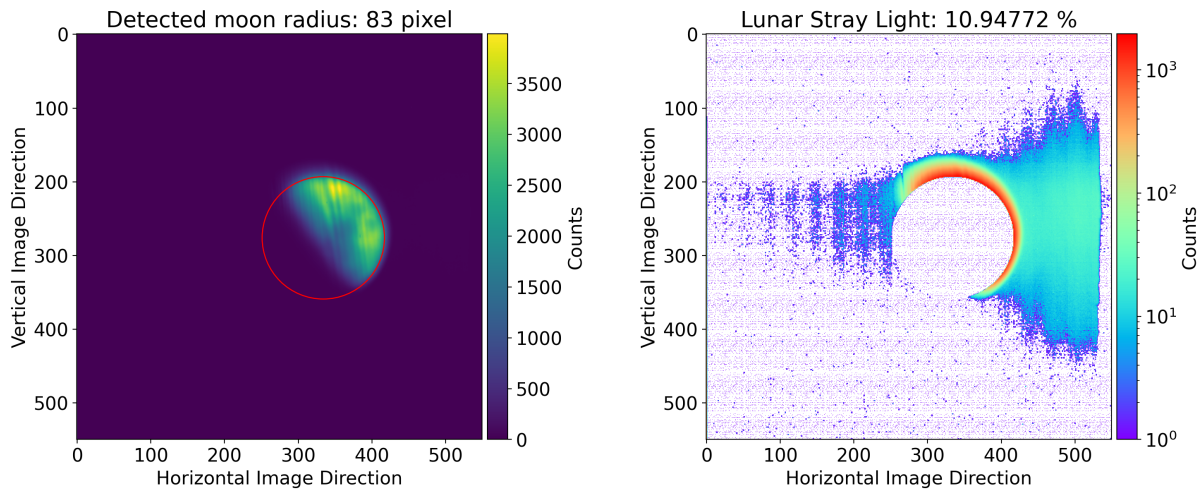


**Figure 5.22:** **Left:** The raw Moon image overlaid with the detected lunar circle. The  $O_2$  A-band absorption spectrum produces an interferogram in the form of stripes that appear on the moon image. **Right:** The Lunar Stray Light image reveal higher stray light values at the upper crescent compared to the right side.

measurements and the inability to switch off the LED for dark images, these measurements could not be analysed quantitatively. Despite a viewing angle limiting aperture, which was installed in front of the high power LED, scattering is clearly visible in the immediate vicinity of the LED, which prevents the light source being separated from the surrounding background.

### 5.5.2 LUNAR STRAY LIGHT AND SPATIAL RESOLUTION

Based on the first preliminary ground-based observation of the moon with the InspireSat 4 instrument, the groundwork for data processing can already be discussed. Figure 5.22 shows a moon measurement and the modulations superimposed due to atmospheric absorption presented in 3.17. Lunar Stray Light (LSL) is defined using the method known from previous targets. The signal area is defined by the full moon disc and all signals from external detector pixels are considered as stray light. The boundary is defined similarly to the slit measurements at the highest gradient of the disk edge. For this purpose, a circle is fitted to the gradient image using circular Hough transforms.<sup>73</sup> Since no dark images were taken for the given detector settings and temperatures, an averaged dark image had to be estimated based on the median of obscured pixels at the edge of the detector. After performing the dark image subtraction, a noticeable amount of noise, up to 5 counts, remained visible throughout the detector. Therefore, any pixel with a value below 5 was set to zero, leaving only stray light

artifacts that showed high irradiance on the detector. For the observed horizontal moon transits, a mean LSL of 12.147% and a standard deviation of 0.68% could be derived. Even if the images are taken in a clear night sky, ice crystals and aerosols along the LOS can cause atmospheric scattering, leading to an unknown uncertainty in the stray light evaluation. Future measurements of this type will therefore require measuring the water vapor and aerosols content for the LOS<sup>132</sup> or modulating it based on reanalysis data. Another unknown uncertainty in this measurement is motion blur caused by a lack of stable instrument mounting.

The high contrast at the edge of the moon body to the deep space background makes it an ideal target to perform MTF measurements similar to slant edge experiments in the laboratory. An example of such an evaluation is shown in Figure 5.23 for an MTF evaluation in the vertical and horizontal image direction. The edge function is first determined via the edge cross-section. The line spread function is obtained from the derivative of this. The MTF results from the Fourier transform of the line spread function. This is usually plotted up to a frequency of 0.5 lines/pixel, which is the highest frequency that can be determined based on the Nyquist theorem. These measurements correspond to the MTF measurements carried out in the laboratory for this instrument.<sup>6</sup> Theoretically, the PSF can also be determined from a full moon and the resulting line spread functions in all image directions<sup>133 134</sup>, although no practical application at the moon edge could be found in the literature. The lower MTF values in the Y direction compared to the X direction can be explained by the stray light artifact blurring the upper edge of the crescent.

Another option for measuring the PSF directly is to use Venus as a stellar target, since it is the brightest planet in the solar system as seen from Earth. Although the Venus spectrum shows a high intensity within the instrument bandpass filter, the Venus intensity varies considerably with distance and Venus phase. Setting the appropriate integration time becomes much more difficult when compared to the lunar disk, as no accurate Venus irradiance model has yet been identified used for in-orbit validation. However, Skyfield has implemented a model that allows the apparent magnitude to be calculated taking into account the distance and phase of Venus.<sup>135</sup> Another limitation for Venus observations is its proximity to the sun. This allows observations only just before sunrise or just after

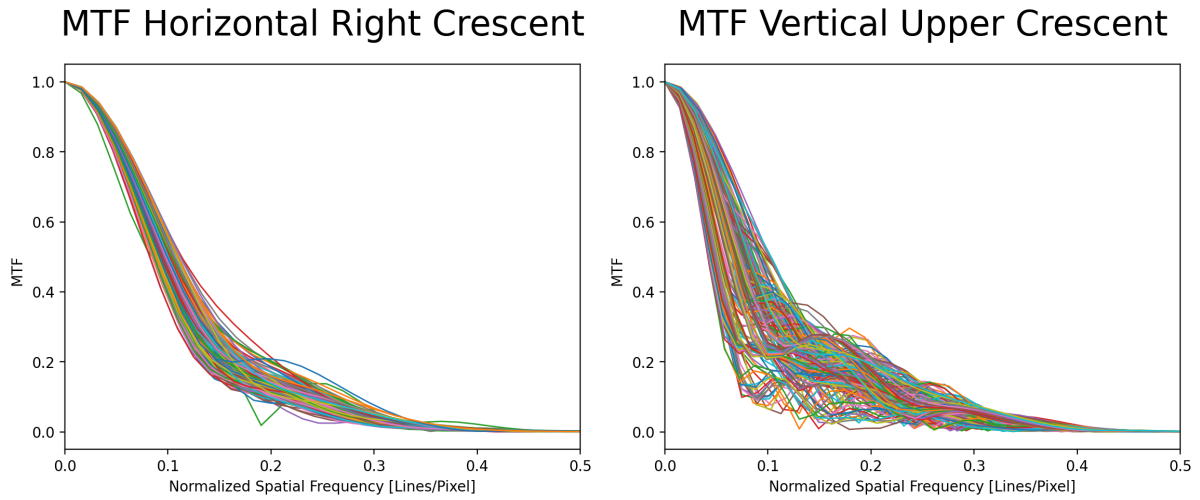


**Figure 5.23:** The MTF measurement for a horizontal lunar transit shows better spatial resolution at the right edge of the crescent compared to the upper edge of the crescent for multiple positions of the stellar target.

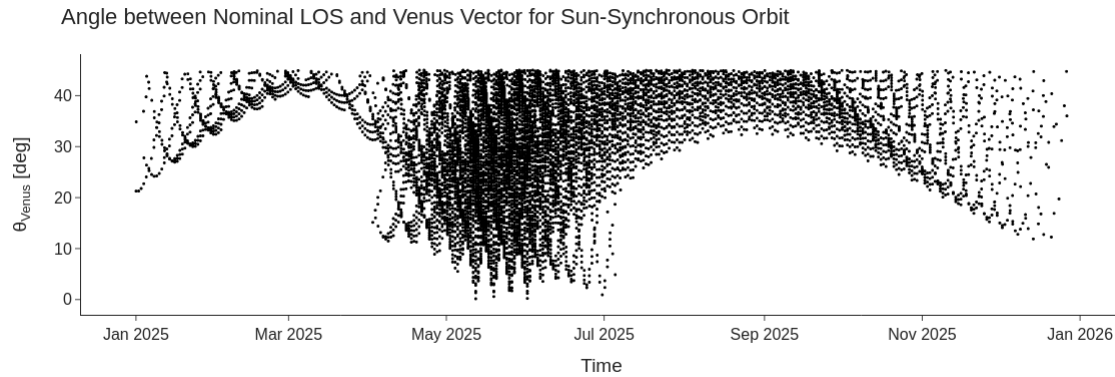


**Figure 5.24:** The proximity of Venus to the Sun allows only one time period in May for observations with low rotation of the satellite, as Venus is otherwise blocked by the Earth or the satellite is in direct sunlight.

sunset, because otherwise the Sun is in the Sun Exclusion Angle or Venus is blocked by the Earth. However, simulations of the angle  $\theta_{venus}$  between the LOS and the Venus vector show that it is possible to observe Venus very close or even within the FOV, as can be seen in the figure 5.24. For the month of May, there are a total of 3 simulated perspectives from which Venus can be observed directly without changing the LOS orientation.

### 5.5.3 LIMB SCAN MANEUVER

Instead of modelling the interferogram caused by atmospheric out-of-field stray light with respect to PST measurements and radiative transfer models, it is also possible to measure it directly when the

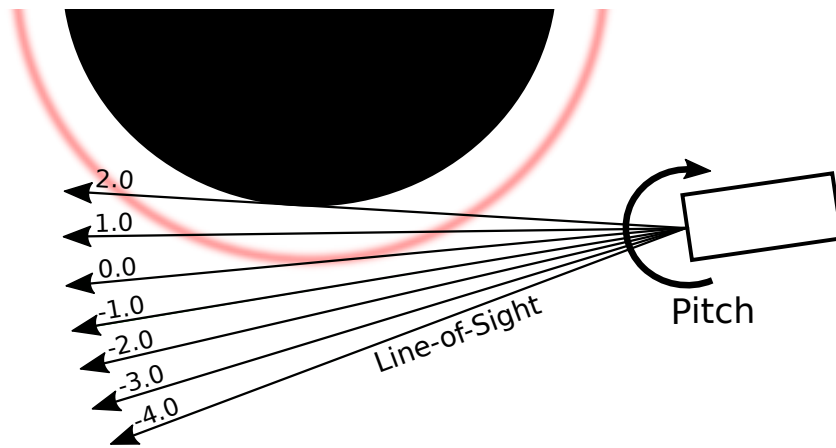


**Figure 5.25:** By scanning the LOS relative to the airglow, the airglow can be used as an out-of-field stray light source. This allows measurement of the absorption spectrum in the interferogram, which can be compared to the interferogram scaled by PST measurements and radiative transfer models.

instrument is deployed in-orbit. To do this, the pitch angle of the instrument is scanned along the limb, as shown in figure 5.25. At a pitch of -4 to -1 deg, the airglow signal can be used as an out-of-field stray light source. Using a radiative transfer model that includes the airglow emission, the integration time can be estimated similarly to figure 5.15 or based on the previous orbit measurements. The LOS is now scanned in 1 degree steps down to +2 degrees tangent to the Earth's surface, revealing the atmospheric absorption spectrum in the interferogram. Since negative tilt angles result in high in-field irradiance, the exposure time and gain factor must be significantly reduced depending on the sun's position. Since such long integrating measurements react very sensitively to other out-of-field stray light sources, the Sun and moon should be as far away from the LOS as possible.

# 6

## Conclusion and Recommendations

The methods presented for stray light measurement and in-orbit validation for atmospheric limb sounders have proven to be suitable for estimating the effects of stray light and optimizing the instrument for future missions. Unlike solely simulation-based stray light evaluations, the measurement methods presented here are capable of monitoring the construction and calibration of the instrument for spectral stray light sources. Continuous monitoring of stray light is necessary to prevent strongly deviating performance values during the manual alignment of the instrument. Even an apparently well-adjusted instrument with good visibility and a narrow PSF can show significant reduction in spatial and spectral resolution because of stray light. The alignment procedure used on previous missions, which sequentially uses a point source for spatial resolution and a diffuser disk for visibility,

does not reveal stray light artifacts spread over large areas of the detector. The PSM measurements demonstrate the precision required to correctly align the three images produced in the instrument. Even if large parts of the image appear to be in focus, the two PSFs of the two gratings may diverge in other parts of the image. The MTF and PSF evaluations between the different experimental setups show a consistent distribution across the FOV. The MTF measurements of the Flight Model demonstrates that a constant high spatial resolution can be achieved over the entire FOV.

Even if the final stray light evaluations of the SHIPAS mission and its in-orbit validation do not fall as planned within the time frame of this thesis, the necessary methods could be developed in cooperation with the SHIPAS team. The use of the Ronchi ruling for fast and integrated measurement methods in combination with PSM as a slower but spatially precise resolution method complement each other. Very early in the design of the instrument, a correlation was found between the adjustment of the front optics and a significant increase of in-field stray light. At the same time, the PSM measurements provide a comprehensive understanding of the spatial and spectral characteristics of the entire FOV, which forms the basis for future correction algorithms and instrument design enhancements. Although the stray light readings vary widely between instruments, the use of Ronchi ruling, slit, and PSM measurements provides comparable distributions as well as mean values for the same instrument state. Unlike any stray light simulation applications, the developed methodology can determine the stray light visibility for different image areas using slit and Ronchi ruling measurements. Furthermore, based on Point Source Transmittance (PST) measurements and radiation transfer simulations, stray light images outside the FOV and their visibility for different perspectives in orbit and the resulting radiation intensities can be determined from Earth. The reconstruction of the out-of-field interferogram spectrum based on the existing data processing chain has already been demonstrated.<sup>96</sup> By reconstructing the visibility and intensity distribution from the angle-resolved PST measurements on the basis of a 3D radiative transfer simulation, the out-of-field stray light interferogram as it occurs in orbit can be reconstructed for the occurring 3-dimensional measurement perspective and Earth scenario. Thus the developed in-field and out-of-field stray light measurement methods provide a foundation for future evaluation of the instrument's temperature measurement

**Table 6.1:** Overview of all in-field stray light measurements and simulations without considering the stray light visibility.

<b>Instrument</b>	<b>In-Field Stray Light Method</b>	<b>Mean Value [%]</b>
SHIPAS QM Config A	Slit @ 763 nm	7.52
SHIPAS QM Config A	Ronchi Stray Light @ 763 nm	6.83
SHIPAS QM Config B	Ronchi Stray Light @ 763 nm	26.47
SHIPAS QM Config C	Ronchi Stray Light @ 763 nm	22.96
SHIPAS QM Config C	Slit @ 763 nm	22.08
SHIPAS QM Config C	Background Stray Light PSM @ 763 nm	23.61
SHIPAS QM Config C	Ghost Stray Light PSM @ 763 nm	9.98
SHIPAS FM	Ronchi Stray Light @ 763 nm	7.44
SHIPAS FM	Ronchi Stray Light @ NIR LED	7.44
AtmoLITE ZEMAX in ASAP	First Order Ghost	6.88
AtmoLITE ZEMAX in ASAP	All Ghosts	8.6
AtmoLITE ZEMAX in ASAP	Total In-Field Stray Light	9.37
Simple Analytical Model	First Order Ghost	10.5
InspireSAT 4 FM	Lunar Stray Light	12.14

uncertainty.

## 6.1 ASSESSMENT OF STRAY LIGHT AND SPATIAL RESOLUTION

A summary of the stray light values from measurements and simulations can be found in table 6.1. Assuming that configuration C correspond to an as-designed optical system, the stray light levels between the ASAP simulations, Ronchi Ruling, Slit and GSL measurements agree with each other. A total an in-field stray light between 6.5% to 11% can be confirmed depending on instrument mission and version. Even if only the stray light-intensive PSM data based on configuration C allow an evaluation of the ghost stray light, an average ratio to the signal level of about 10% could be determined by isolating the ghost artifacts from other stray light. This is in agreement with both the numerical simulation and the simplified analytical model calculations. Considering the simulated stray light caused by contamination of 0.7 % more than 90% of the total in-field stray light is caused by ghost artefacts. The extent to which stray light contributes to the instrument’s measurement error depends on the visibility of the stray light and 2<sup>nd</sup> order interferogram caused by the ghosts. Using a point source as an example, it could be shown that ghost artifacts in configuration C do not interfere with the PSF or itself, in contrast to the symmetrical stray light kernel surrounding the PSF. The distribution

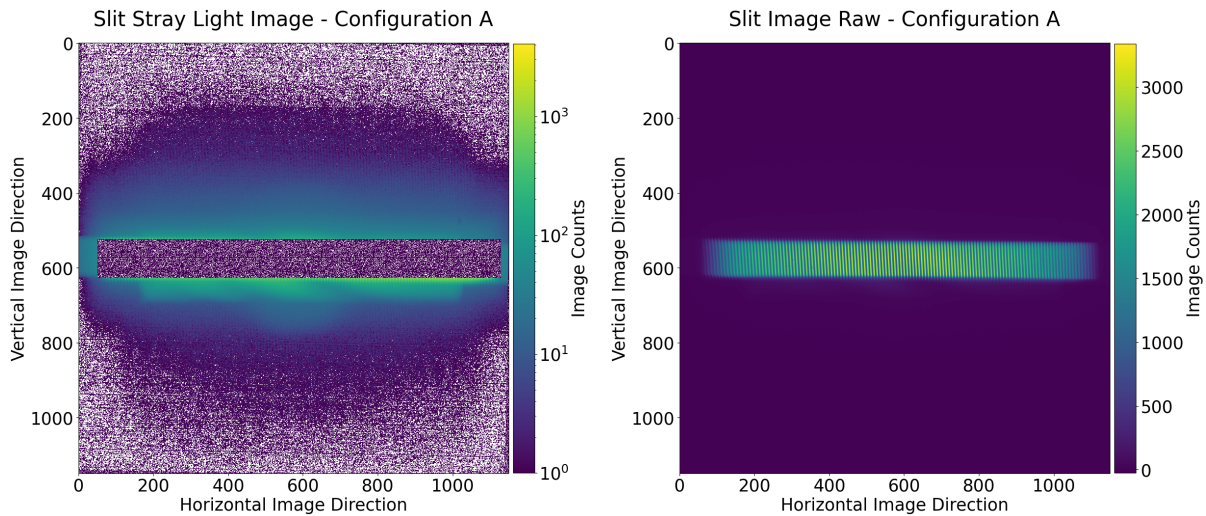


**Figure 6.1:** This stray light measurements demonstrated the best performance across all instrument configurations, with the lowest values for RSL, slit stray light, and shadowed visibility.

of the ghost artefact shows strong variation from 2% to 20 % depending on the field angle of point source. Integrating all ghost artefacts shows a high correlation between the visibility distribution and ghost intensity. Although a spatially resolved analysis of the interference of two point light sources could not be performed, the correlations between visibility and ghost intensity indicated interference effects. Measurements of slit and Ronchi Ruling configuration A have shown that low stray light visibility and low total stray light intensities are achievable.

The stray light measurements with the slit in figure 6.1 show the lowest stray light modulation compared to the other configurations. Since it has not been possible to optimize visibility, spatial resolution and stray light simultaneously for current instruments, it is to be assumed that these values do not represent the global optimum that can be achieved for this optical design and that significantly better values are still possible. Preliminary evaluation of the SHIPAS FM data have shown, that harmonic frequencies can be another artefact that needs to be observed when adjusting the instrument optics. The assumption that ghost artifacts fall back to the nominal signal areas, which was made within the ASAP simulation, could only be confirmed experimentally for a radius of 100 pixels in the center of the image. In the outer image areas there are up to 140 pixels between signal and ghost.

Although the presented calibration procedure provides the possibility to specify a traceable measurement uncertainty in the long term, not all uncertainties could be estimated with sufficient ac-

curacy. For a final estimate of stray light uncertainty, the entire data processing chain must be included in the assessment. However, equation 3.23 can be used to estimate the magnitude of spectral stray light to derive possible improvements and recommendations. Considering a signal level of  $N_{Signal} = 3000$  counts and an integration time of  $\Delta t_{Integration} = 1$  s as a typical observation scenario. The best stray light configuration was A with a mean shadow visibility of  $V_{IFSL} = 27.018$  %, a mean signal visibility of  $V_{Signal} = 66.11$  % and an average Ronchi Stray Light (RSL) of 6.8 %. Assuming that the PST measurement is consistent between different front optic configurations, a reconstructed stray light level of  $\frac{N_{OFSL}}{\Delta t} = 56.27 \frac{counts}{s}$  and a mean out-of-field stray light visibility of  $V_{OFSL} = 38.14$  % is considered. From this, the Interfering Stray Light to Signal Ratio (ISR) for Config A can be determined as follows:

$$ISR_{Config A} = \frac{V_{IFSL} \cdot RSL \cdot N_{Signal} + V_{OFSL} \cdot \frac{N_{OFSL}}{\Delta t} \cdot \Delta t_{Integration}}{V_{Signal} \cdot N_{Signal}} = 3.8 \% \quad (6.1)$$

This does not fulfill the required ISR of max. 1 %. However, by examining each parameter, there are numerous opportunities for optimization and correction.

## 6.2 INSTRUMENT STRAY LIGHT REDUCTION AND CORRECTION

Comprehensive system-level stray light analysis and literature review provide several possible solutions to significantly reduce in-field stray light, ghosting and out-of-field stray light.

1. The most straightforward method for mitigating the impact of in-field stray light visibility  $V_{IFSL}$  on the signal is to incorporate it into the calibration process. This parameter has not yet been included in the instrument calibration, so it is likely that even lower values than 27% are possible. However, the extent to which this value can be optimized independently of other calibration parameters such as spatial resolution is not known and needs to be investigated in further experiments.
2. Looking at the simplified analytical model for ghosting in equation 3.31, it is clear that increasing the external quantum efficiency offers the greatest potential for reducing in-field stray light.

Nano-black antireflective coatings on detectors and other post-manufacturing treatments have shown absorption of up to 99%.<sup>136 137 138 139</sup> The GSL would then drop to 0.35%, reducing the in-field stray light by a factor of about 20. At the same time, the sensitivity of the detector would increase. However, such a coating would reduce the detector MTF. It is also unknown how such a coating affects the generation of the interferogram on the detector. Another option is to use low dark current deep depletion CCD technology, which has a quantum efficiency of up to 93% in the NIR.<sup>140</sup> Using such a detector would reduce the GSL to about 1.95 %.

3. Since the interferogram spectrum for the in-field and out-of-field measurements is measured to be consistent, the out-of-field interferogram spectrum can be modelled using radiative transfer models for further corrections, as shown in figure 5.15. Assuming that the out-of-field irradiance simulation can be validated for different perspectives, a subtraction of the out-of-field interferogram is possible. This alone would be a 0.9 % reduction in the ISR to 2.7 %.
4. The field stop is widely recognised as one of the most effective methods of reducing out-of-field stray light in telescope design, but has not been implemented due to integration challenges. It's created by an aperture placed on the intermediate image to limit the FOV of the instrument in front of the actual image plane. Thus, any optical path outside the intermediate image plane cannot cause further scattering in the instrument. Since the only given intermediate images are on the diffraction gratings, the field stops must be placed there. Such a mask would also increase the complexity of the alignment, since both masks have to be aligned relative to each other. Given the observation of strong ghost reflections in the near-field region, it can be concluded that a field stop would also limit the boundaries of the second-order image, since the out-of-field stray light image also shows a strong correlation with the in-field stray light image. A black, highly absorbent foil, which can easily be placed on the diffraction grating for initial tests, could not yet be tested in stray light experiments to evaluate the advantages of the field stop. However, a preliminary test in the laboratory can be performed in the future without much effort.

5. The effect of diffraction gratings on stray light could not be measured or further analyzed. In general, the design recommendation for stray light is to avoid intermediate images on optical surfaces<sup>57</sup>, which can not be avoided for an ISHI design. Several manufacturers offer various types of low stray light gratings for space applications, which could be integrated instead of the current off-the-shelf gratings.<sup>100</sup> It is also feasible to determine stray light levels based on in-house test setups, or to determine surface quality and irregularities in order to make the ideal selection from the products currently in use. This could also have a further impact on the spectral variance of the interferogram, as the wavefront is generated consistently over the entire grating.

Considering only the increase in quantum efficiency to 92% and the complete correction of out-of-field stray light, the resulting ISR is 1.1%. This does not yet take into account stray light corrections through deconvolution or further reduction of stray light visibility. Due to the multitude of possible optimization opportunities for reducing stray light, it is likely that future instruments can achieve a ISR value of less than 1%.

### 6.3 EVOLUTION OF LABORATORY CALIBRATION AND METHODOLOGY

Despite the success of the stray light measurements, the validation of the described methodology was limited due to its complexity and the time constraints of the SHIPAS mission. As the stray light measurement methods developed were applied for the first time using a novel SHIPAS QM instrument design, it is necessary to further develop and improve the existing method with the final SHIPAS FM instrument and further missions. In particular, the in-orbit validation will show whether laboratory measurements agree with in-orbit measurements. In order to increase traceability and reproducibility for future instruments, various methodological improvements and possible sources of uncertainties have been identified:

1. The alignment of the instrument lenses and gratings can be significantly improved by using Ronchi ruling measurements. Currently, the instrument is manually rotated 90 deg to mea-

sure visibility at the ACU and the PSF at the mACU, optimizing spectral and spatial performance sequentially. However, the PSM measurements have shown that a single PSF measurement is not sufficient to optimize spatial performance and minimize stray light, as these parameters can vary significantly across the FOV. The two PSF maxima shown by the PSM measurements for certain areas of the image cause light from different field angles to interfere with each other. In addition, visibility, spatial resolution, and stray light are interconnected and should not be optimized separately. Thus, with the exception of the horizontal spatial resolution, all relevant optimization parameters can be set with a single measurement setup without any mechanical adjustments. Since the image is integrated in the horizontal direction in the later evaluation, the horizontal spatial resolution is less relevant for the optimization process and can be validated later by rotating the target by 90 deg.

2. No systematic error could be evaluated for the stray light measurements presented here. In order to obtain measurements of the stray light quantities that are traceable to SI standards, the stray light performance of the reference autocollimator telescope must be calibrated using light sources with known scattering properties. To ensure comparability between the instrument and the reference telescope, the FOV needs also to be increased to cover the instrument FOV.
3. For PSM measurements, the stray light signal had to be extrapolated based on unsaturated pixels near the PSF. Since the power meter measurements could not sufficiently resolve the PSF power, a validation or extrapolation based on this variable was not feasible. By further splitting the power between the mACU and the power meter, the PSF can be resolved by both measurement devices to cross validate both methods.
4. Resolving PSF both below and above the laser threshold can significantly enhance the understanding of the instrument's spectral and spatial behavior. Measuring the coherent PSF above the laser threshold provides the optical transfer function needed for possible future deconvolution techniques. Using the PSM method with an unsaturated coherent PSF, the interferogram should theoretically be reproduced by the sum of the individual field angles. Since the existing

interferogram simulation in ZEMAX also constructs the overall image from a sum of individual point measurements, the PSM offers an ideal supplement and long-term convergence to approximate simulations and measurements and thus to understand the function of the system more deeply.

5. Approx. 50% of the instrument incident power is backscattered onto the mACU due to the beam splitter. The sensitivity to stray light uncertainties caused by this effect can be experimentally estimated by varying the Ronchi angle or the distance between the mACU and the instrument. Although small changes in the Ronchi ruling angle did not show any change in the stray light values, this cannot be proven by sufficient data. To avoid any backscattering, it is recommended that future experiments use a Ronchi ruling where shadowed areas are coated with highly absorbent black material. Assuming that backscattering from the mACU into the instrument is no longer collimated, there must be a correlation between the distance to the instrument and observed stray light artifacts. In previous experiments, the mACU was moved manually along the optical axis, which caused undesired rotation. Two parameters were modified in the experiment, making it impossible to directly relate the data to each other. A more precise and controlled way to perform this test is by moving the instrument along the optical axis using the hexapod.
6. The aperture illumination of the instrument is inhomogeneous when imaging the laser waist with the mACU. Therefore, the optical parameters of the outer optical elements are underestimated, while those of the inner areas are overestimated. The creation of a point source that is simultaneously tunable in wavelength, sufficiently small, homogeneous across the mACU aperture and bright enough for stray light measurements has not yet been achieved. To estimate the extent to which the aperture illumination homogeneity is relevant to the laboratory point source, observing stars, or other small targets provides an option for ground validation. Also the homogeneity of the illumination with extended light sources like the split should be evaluated using the methods developed for the ACU diffuser configuration. An additional

method for evaluating and correcting the inhomogeneity of the light source is to move the instrument laterally in both the vertical and horizontal directions on the hexapod relative to the light source. This allows the Gaussian distribution of irradiance to be positioned at different aperture positions.

7. It was not feasible to quantify the illumination distribution of the instrument aperture through the Ronchi ruling. Consequently, this assessment must be conducted once more for the mACU with the extended Ronchi ruling target, which was utilised for the ACU. Given that the diameter of the exit aperture of the integrating sphere is more than twice that of the ACU, it can be postulated that a uniform aperture illumination can be achieved.
8. For the stray light measurement with PSM, a rather large signal distance of 40 pixel had to be selected. In addition to insufficient extrapolation of the signal strength, stray light at the output of the fiber or in the microscope objective could be another cause for this. To measure the stray light contribution of the autocollimator, the slanted edge measurement could provide the necessary data. However, the data sets repeatedly exhibit damaged image data and unrealistically uniform and deep detector noise at zero counts for the shadowed regions. Likewise the point source measurements showed inconsistent dark image values and uncertainty due to the monochromatic illumination of the RGB sensor. Therefore, an alternative monochromatic sensor should be considered with a better understanding of the detector noise and the pre-processing performed by the readout software.
9. The in-field stray light correction methods that employ classical deconvolution techniques have proven to be ineffective, as they are only applicable to incoherent light that does not result in interference. Furthermore, the current experimental setup does not provide an appropriate test case for validating such a correction method. Using the integrating sphere with the Ronchi ruling, the spectra are distributed homogeneously over the output aperture, even when two different laser light sources are used simultaneously. Consequently, it is currently not possible to experimentally determine whether a correction method is capable of correcting for the

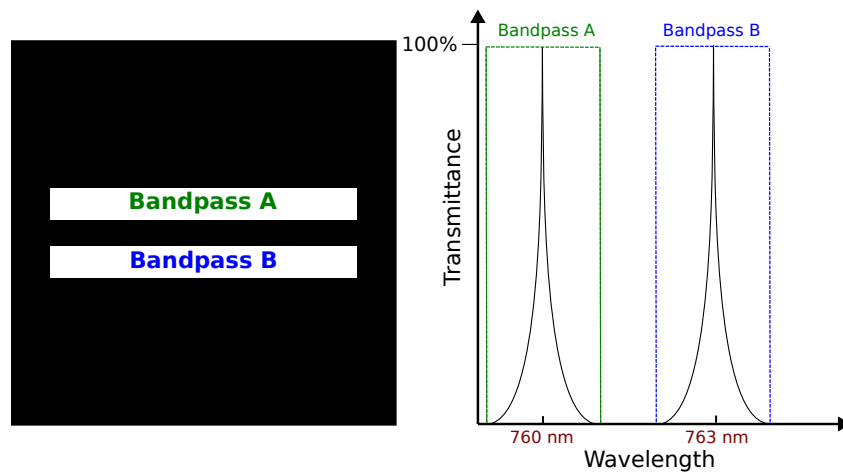


**Figure 6.2:** The proposed double slit target, using two different bandpass filters, enables testing of a stray light correction method for inhomogeneous spectral distribution, as expected for in-orbit airglow measurements.

overlap of stray light from two different light source spectra at two different locations. Figure 6.2 illustrates what a target might look like that allows validation of stray light correction methods for the ISHI system. Instead of a single slit, a double slit is created by coating a glass plate with a highly absorbent black material. The transparent slits are coated with different bandpass filters corresponding to two different wavelengths of the two lasers. This allows the wavelengths of the two mixed lasers to be spatially separated. The black-coated, shadowed area between the two apertures should be free of stray light after the correction methods is been applied correctly. The spectrum of each slit is altered only by the stray light from the source aperture.

10. To investigate the increase in stray light through the front optics, a component-based measurement can narrow down the source of the scattering. To do this, the front optics are placed in front of the mACU, isolated from other components and the Ronchi control is imaged on a free-standing detector. If the high stray light values in this configuration can be reproduced independently of the mACU, they can be isolated as a problem caused only by the front optics.
11. When the lasers were set to medium power to illuminate the integrating sphere, it was observed that the laser light source sporadically had a wider FWHM when measured by the spectrum analyzer. This behavior was also visible in the interferograms. Currently, only the peak value

of the spectrum analyzer is recorded. For future measurements, recording the full spectrum visible in the bandpass may help to better identify such behavior and compare the FWHM of the laser spectrum with the interferogram spectrum.

12. The uncertainty of PSM-based stray light measurements relies heavily on the quality of noise reduction and shot noise. A qualitative assessment of the raw log-scaled stray light data was used to determine the adequacy of the chosen stray light background in relation to the noise level. To improve the current interpolation method with different laser power configurations, adjusting the integration time instead of the laser power could be used as a second method for cross-validation, resulting in the same amount of integrated energy detected.
13. Details of the data processing of stray light measurements have not been published in the literature. However, experience from this work has shown that stray light values strongly depend on the experimental setups as well as on the stray light limits set in the data processing. An open source software that standardizes data processing based on different stray light calibration targets would be useful for the whole remote sensing community. Stray light quantities would then be comparable between instruments.
14. The dark images are significantly affected by fluctuations in the discharge lag noise, especially for out-of-field stray light measurements. This can be reduced by avoiding in-field PST measurements in the measurement grid. Also, using a snake pattern in the scan sequence, measuring in the positive and negative horizontal directions consecutively, should improve the median dark image subtraction, reduce the total measurement time and reduce fluctuations in the discharge lag noise.

#### 6.4 IN-ORBIT SIMULATION AND VALIDATION

The open-source software packages Skyfield and Eradiate have demonstrated promising capabilities for simulating stray light scenarios and possible observation of stellar objects to validate in orbit instrument performance. The documentation as well as the applications of Eradiate have also proven to

be much more user-friendly than previously used software packages used for radiative transfer simulation. Smaller experiments with Eradiate's abstract canopy function, based on floating disks arranged in different geometric shapes, have shown promising results in modeling different cloud formations and accurately correcting out-of-field irradiance for different cloud coverage scenarios. Eradiate also enables the modeling of inhomogeneous ground reflection properties and 3D surface models.

Skyfield has proven capable of simulating satellite orbits and instrument LOS with respect to a variety of celestial objects. Since the integrated libraries for satellite propagation, spacecraft mission planning, and the data source for orbital elements have been used for a variety of space missions, a high accuracy should be achievable. However, the implementation of the LVLH coordinate system is based on in-house development and has not been tested. The Skyfield community is currently developing an LVLH implementation, but it has not yet been released. To validate the software package, one possible strategy is to compare it with closed-source software frameworks such as Freeflyer, which are based on the same open-source libraries as Skyfield. Another option is to validate observations based on other limb sounding instruments already in orbit, such as the freely available Level 1 data product from the MIGHTI instrument.



# Appendix

**Table A.1:** AtmoLITE optical specifications. Values are obtained from the thesis of Oliver Wroblowski and are based on ZEMAX simulations, datasheets and measurements<sup>6</sup>

<b>Optics</b>	front	camera	combined	
eff. focal length	653.22	85.74	403.06	[mm]
object space NA		0.061		[—]
image space NA	0.0573	0.0937	0.0926	[—]
field of view			$\pm 0.65$	[deg]
image height			19.684	[mm]
magnification		0.625		[mm]
image distortion	1.09	0.15	1.38	[%]
operational temperature			-30 to +30	[°C]

<b>Spectrometer</b>			
littrow wavenumber $\sigma_L$		13047	[ $cm^{-1}$ ]
littrow angle $\theta_L$		6.6018	[deg]
prism apex angle $\alpha$		5.47	[deg]
entrance angle $\beta$		4.8375	[deg]
grating angle $\eta$		1.7643	[deg]
groove density G		3000	[ $cm^{-1}$ ]
illuminated grating area width		1.6	[cm]

<b>Bandpass Filter</b>			
central wavelength		$762.8 \pm 0.3$	[nm]
thermal drift		$< 0.005$	[nm/ $K^1$ ]
covered wave numbers		13057 to 13160	[ $cm^{-1}$ ]
FWHM		6.5	[nm]
covered interferogram frequencies		9.0 to 85	[ $cm^{-1}$ ]

<b>Detector Array</b>			
detector type		GSENSE400Bsi	[—]
illuminated pixels		1010 x 950	[—]
pixel size		11	[ $\mu m$ ]
External quantum efficiency @ 763 nm		0.7	[—]

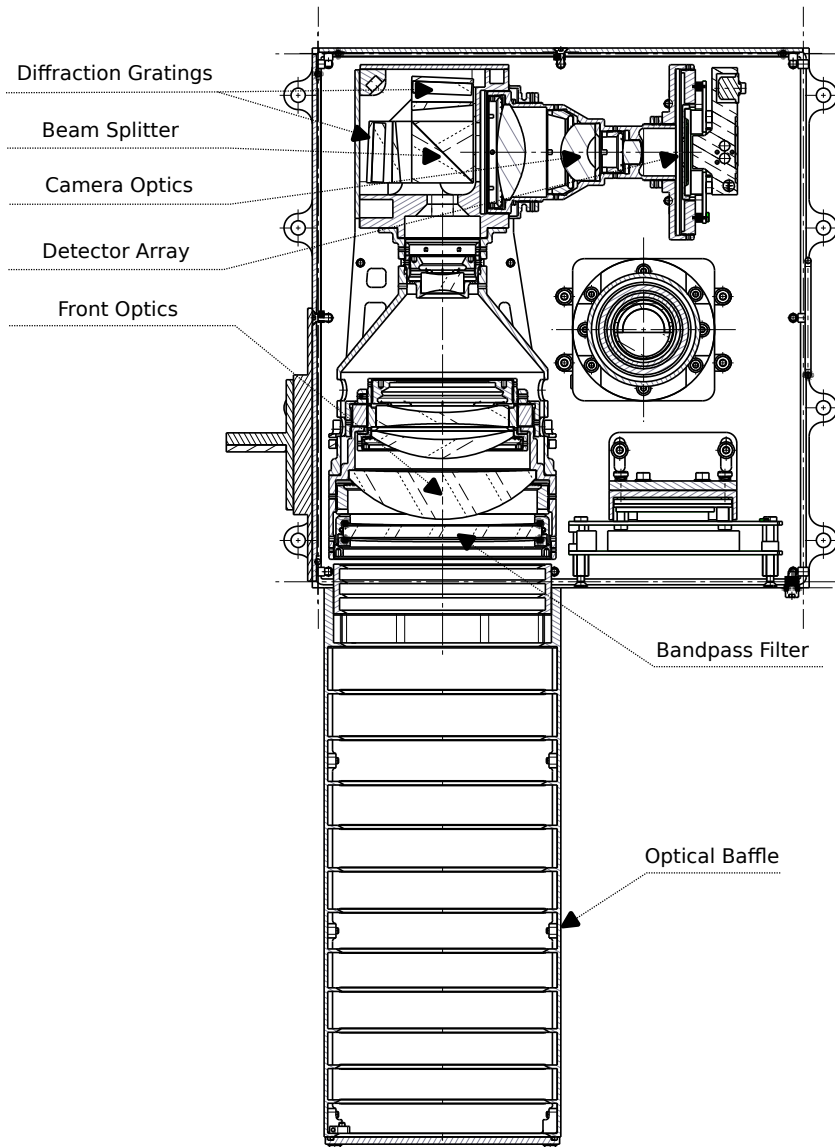
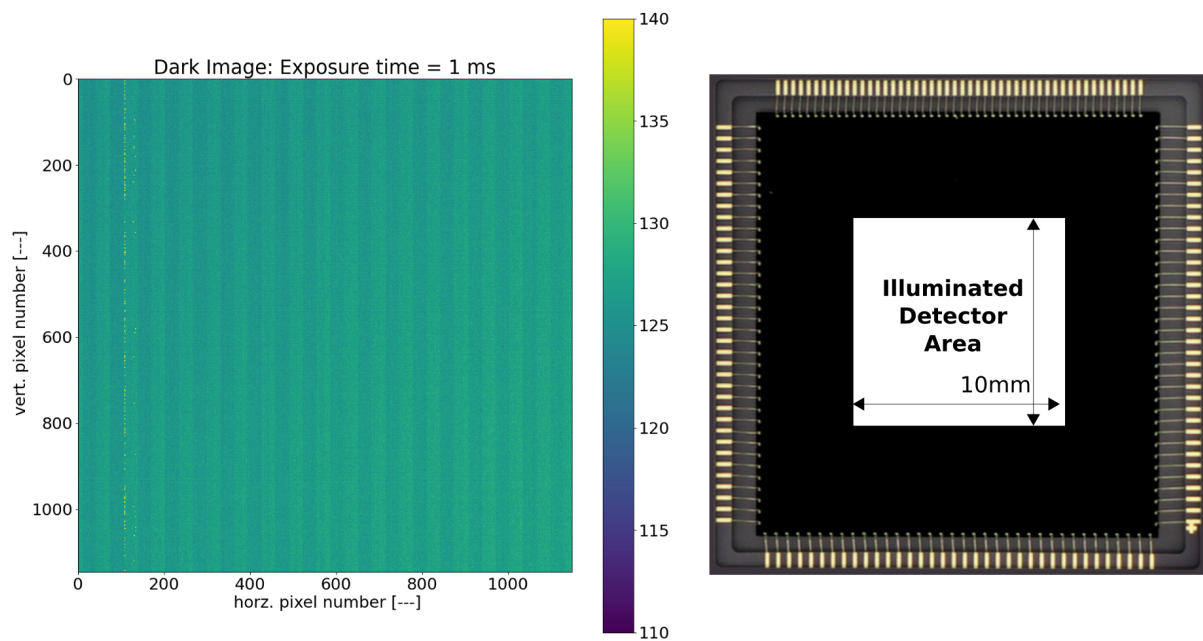
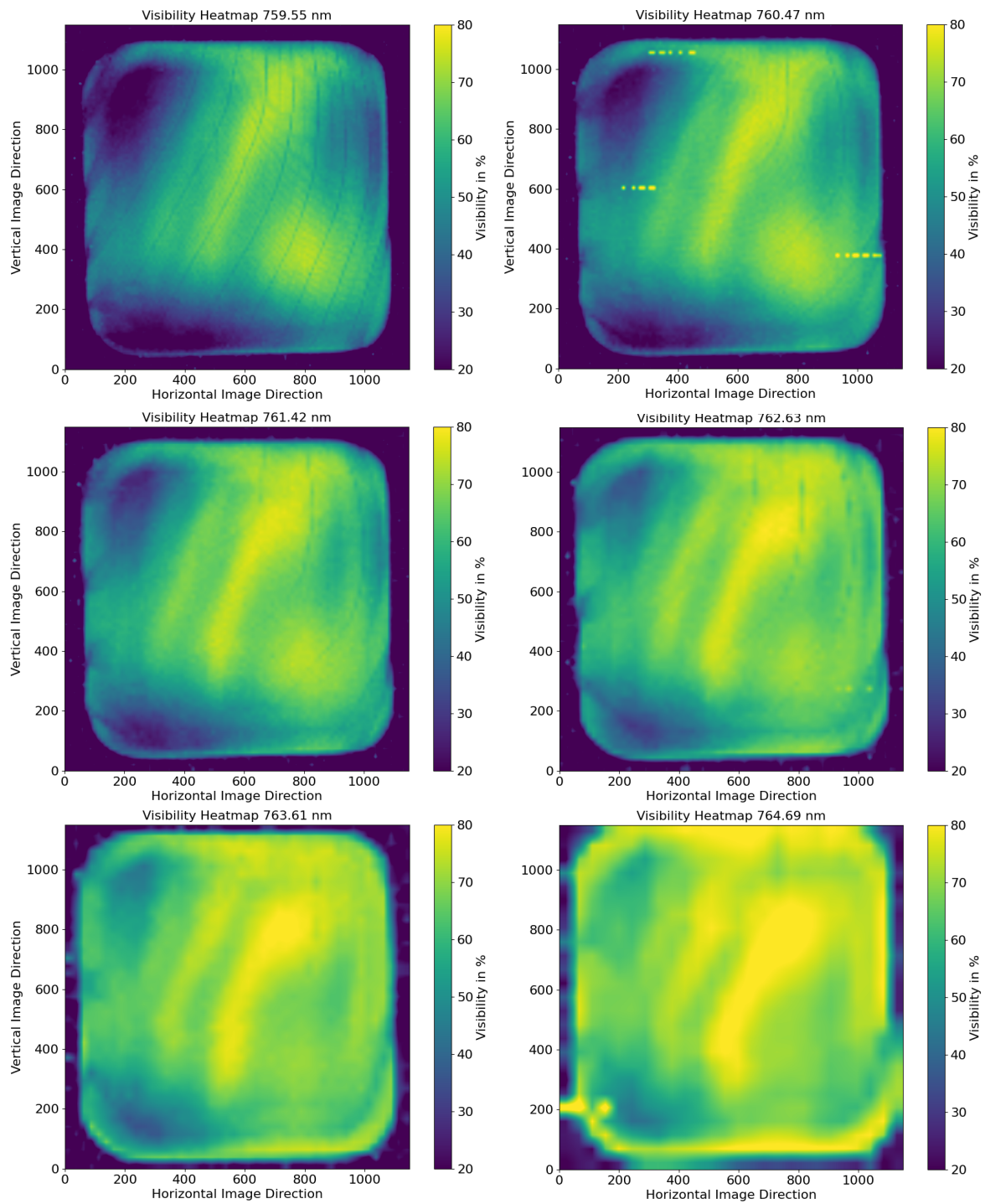


Figure A.1: Top view of the SHIPAS QM CAD design showing the main optical components of the instrument.



**Figure A.2:** **Left:** Fixed Pattern Noise  $\sigma_F$  visible in the raw data of the detector used in the AtmoLITE IS-4 configuration. **Right:** The illuminated area of the detector is limited with a mask to the FOV of the instrument.



**Figure A.3:** Visibility heatmaps of the SHIPAS QM instrument. The visibility is estimated using a 2D sliding window that is scaled based on an initial interferogram period estimation in the middle cross section. Therefore, the window size increases with lower interferogram frequency.

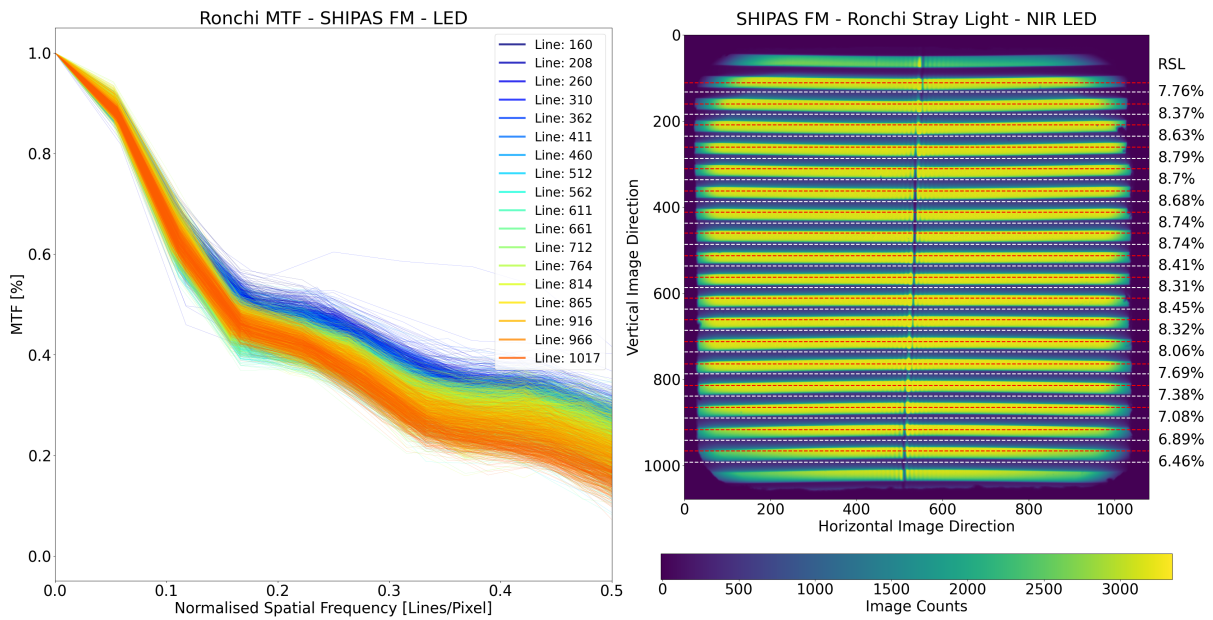


**Figure A.4:** Evaluation of MTF and RSL across the FOV for the final SHIPAS FM. **Left:** MTF evaluation across the FOV. The upper region of the image provides better spatial resolution than the SHIPAS QM. **Right:** The RSL is evenly distributed with a mean value of 7.44 %.

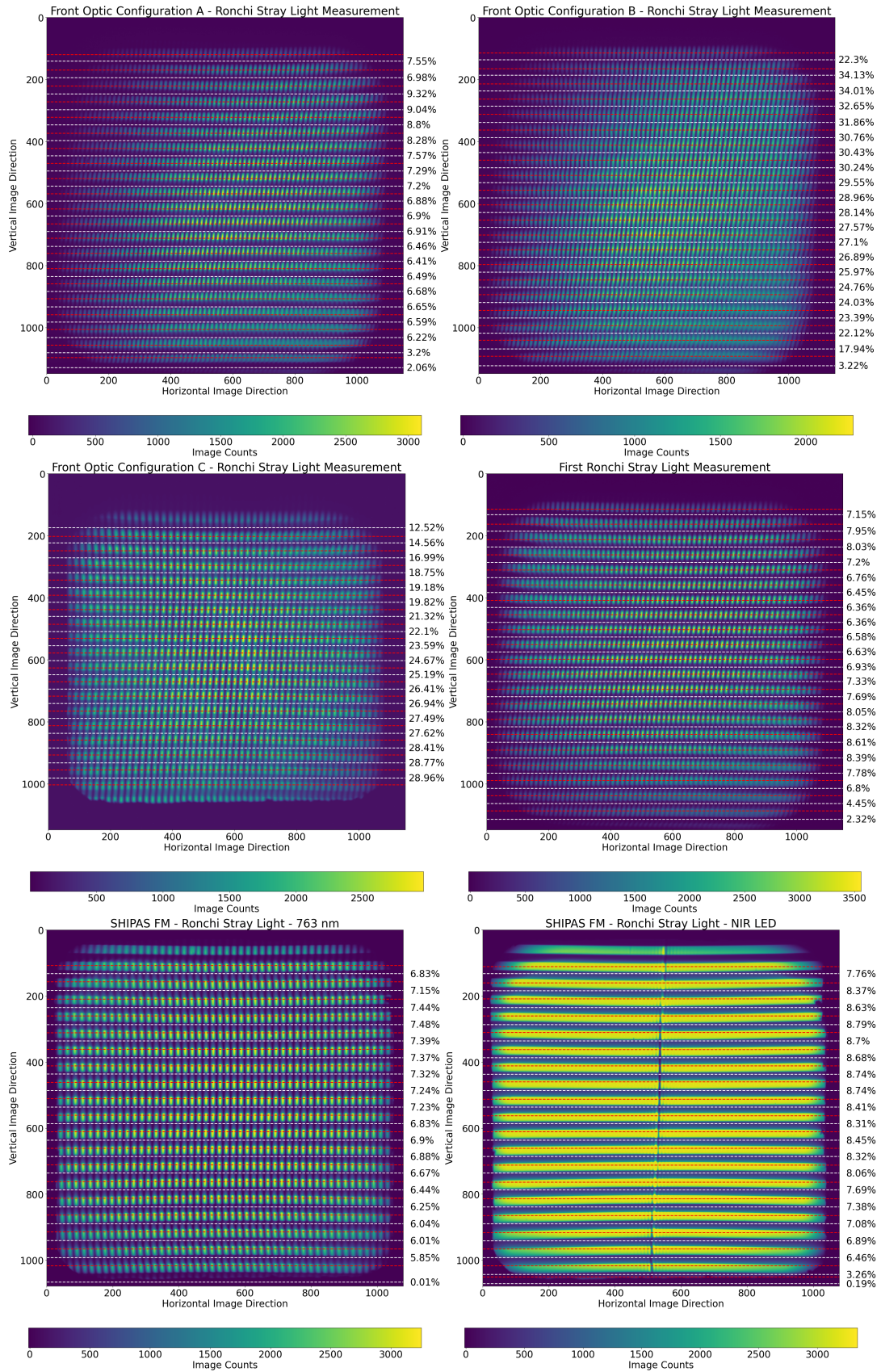
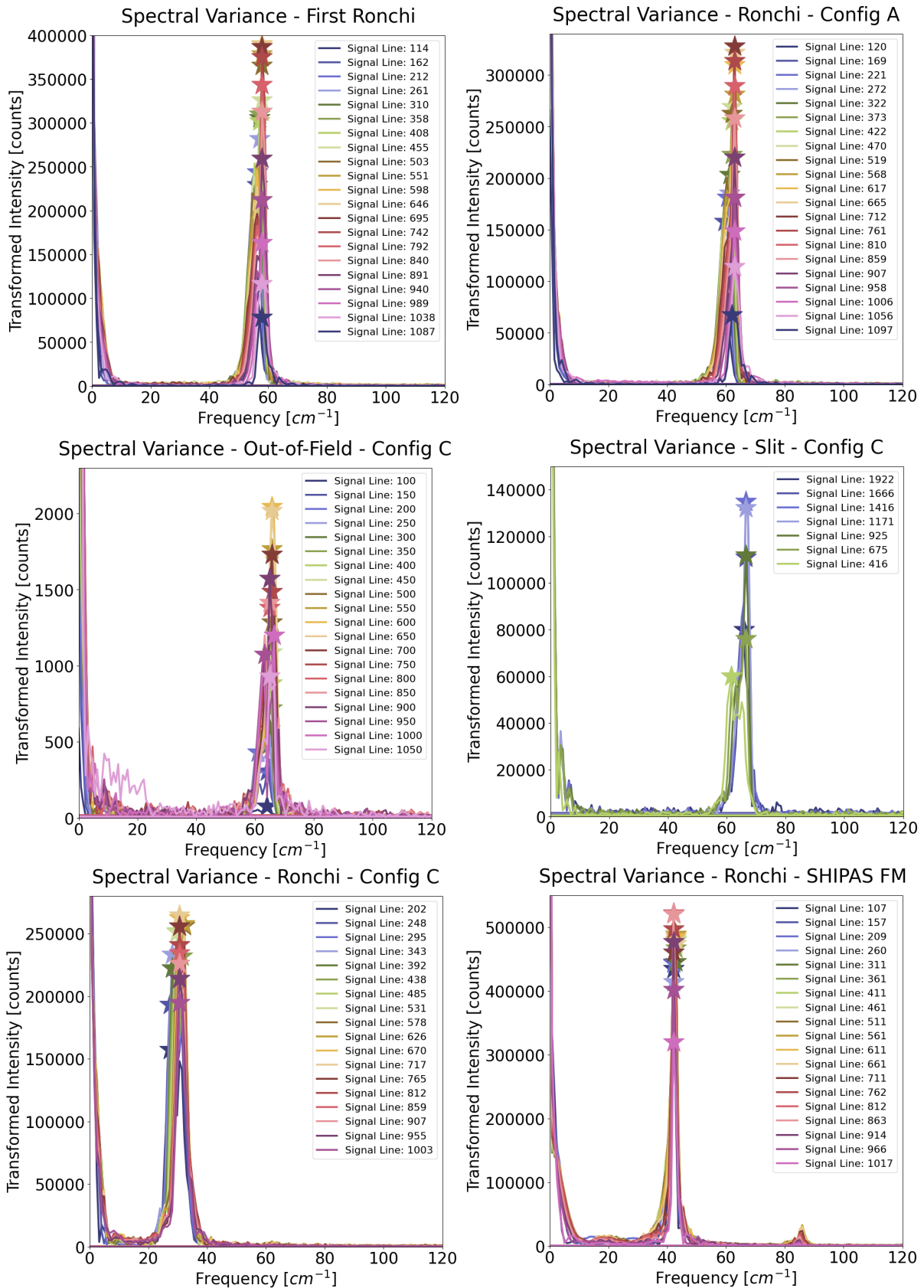
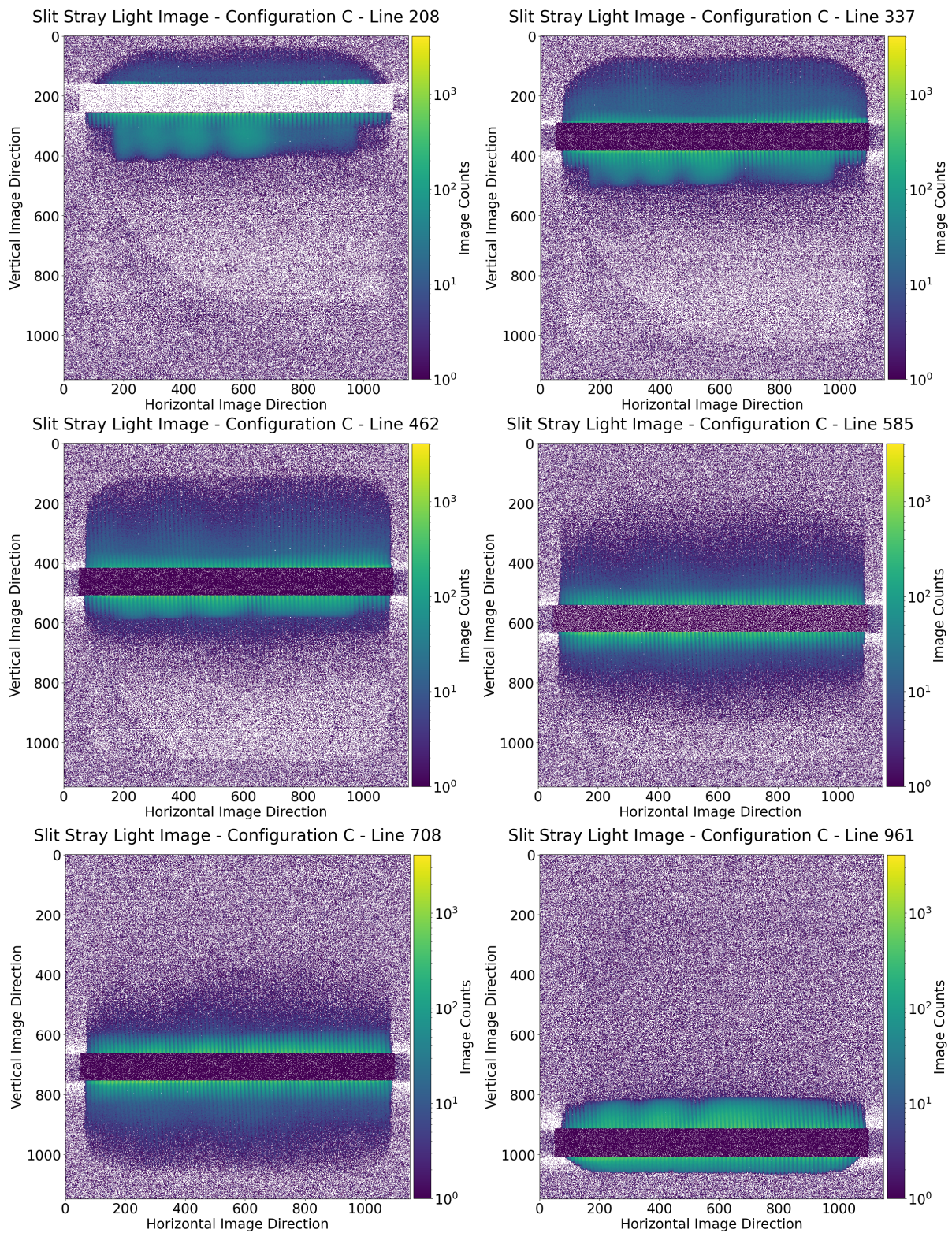


Figure A.5: Ronchi rulings measurements of different instrument configurations showing the distribution of RSL in the vertical direction on the right side of the image.



**Figure A.6:** The spectral variance in the vertical image direction differs depending on the instrument configuration. The SHIPAS FM instrument shows a significant increase in spectral variance, but harmonics are visible in the spectrum.



**Figure A.7:** Slit measurements at 763 nm in vertical image direction. Visibility decreases with a constant gradient into the shadowed areas and drops to zero only leaving unmodulated stray light as can be seen for the slit at row 208.

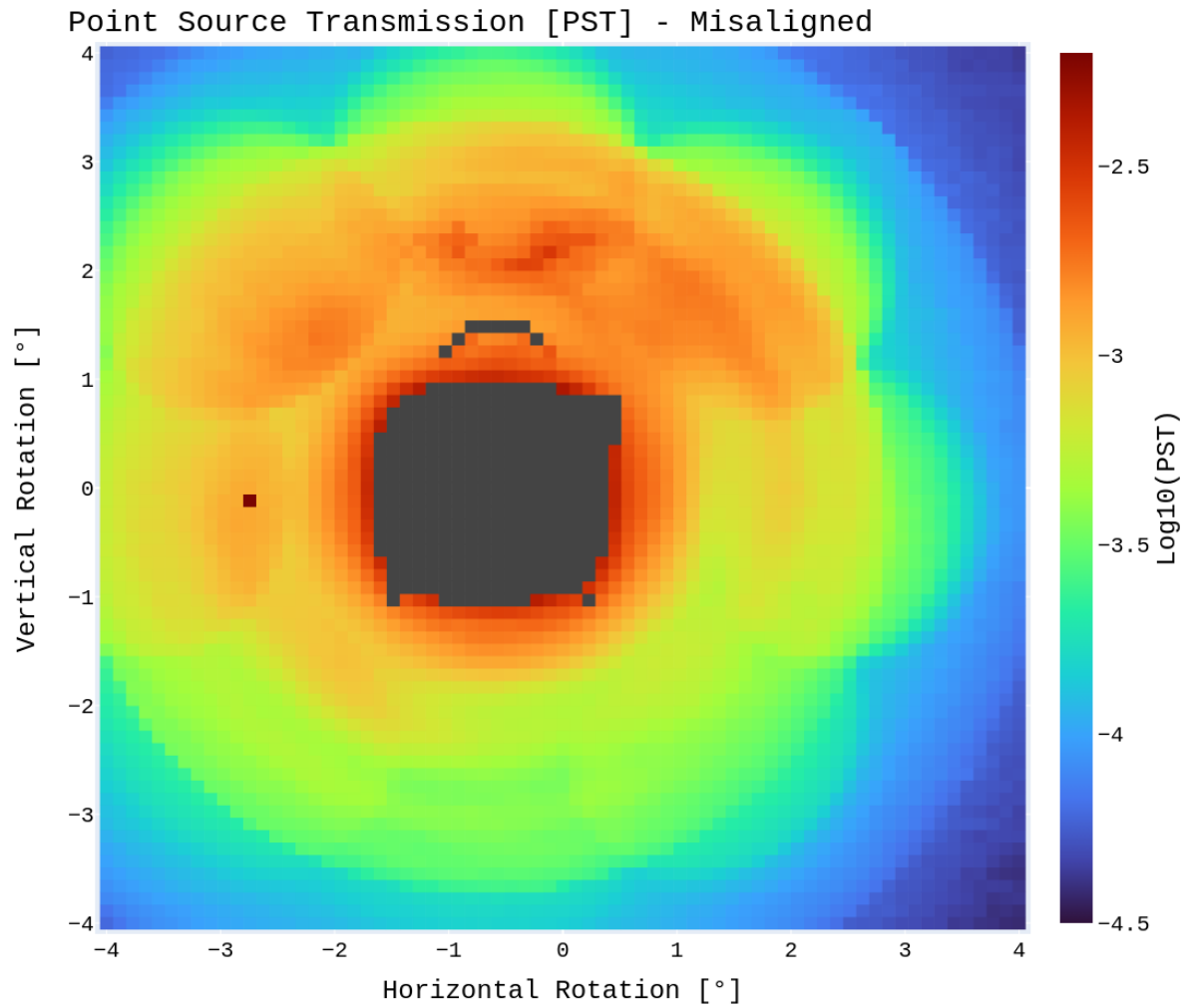


**Figure A.8:** PST measurement after increasing the distance between mACU and the instrument by opening the optical rail carrier of the mACU. This causes a misalignment between LOS and the optical axis of the mACU. However, the data is comparable to the on-axis data.

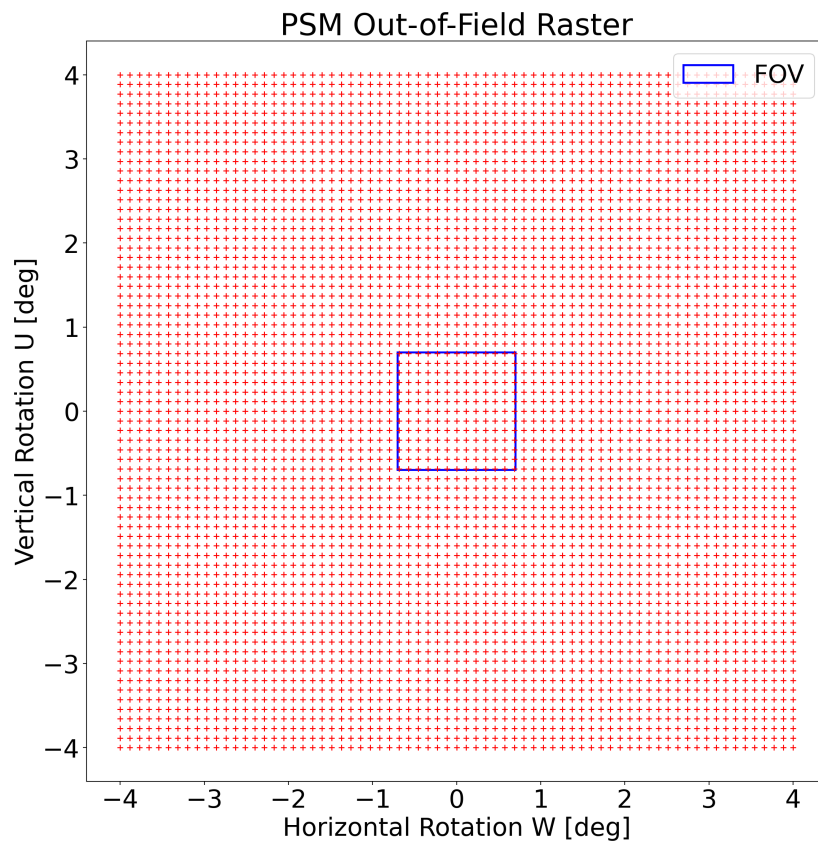
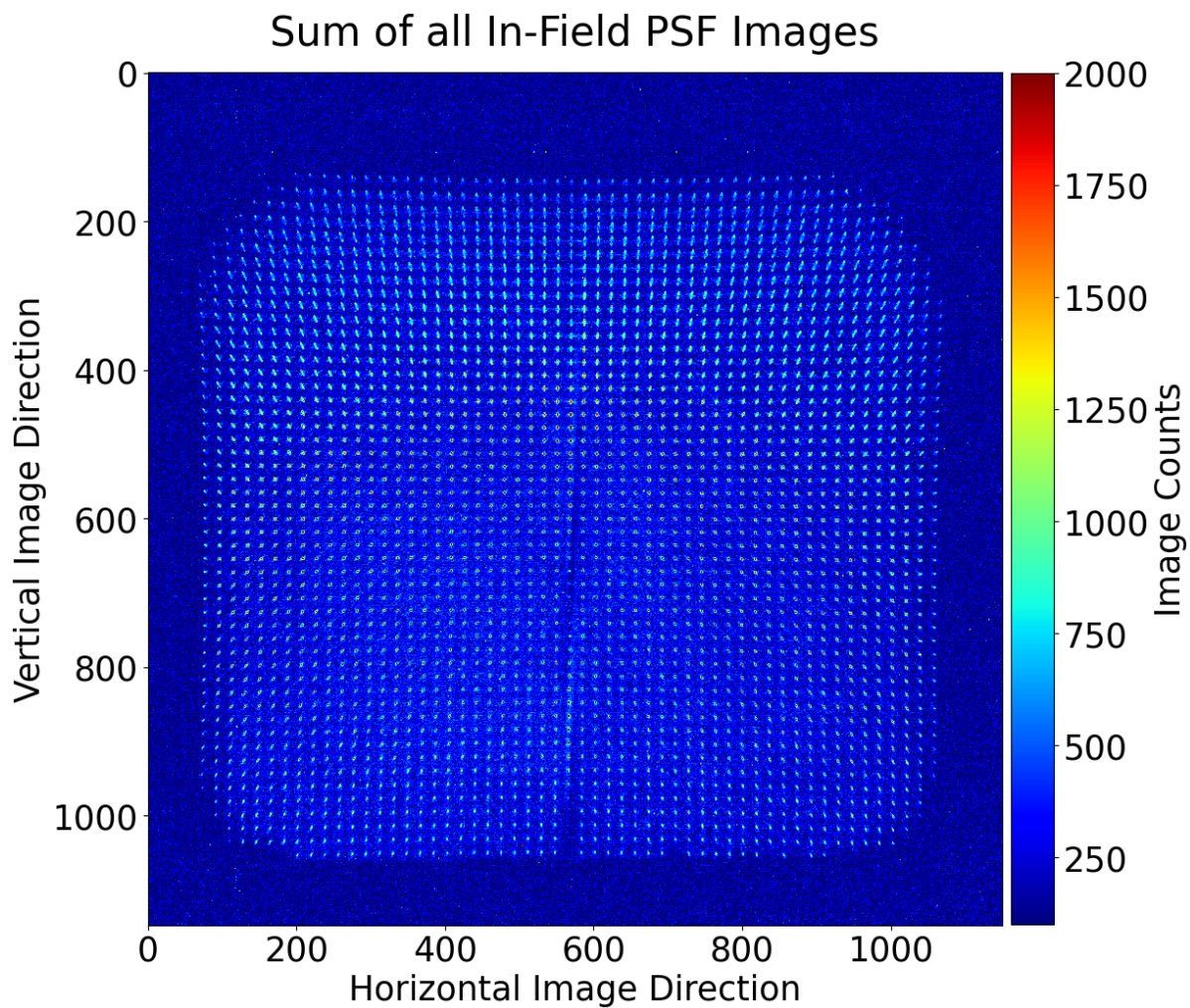
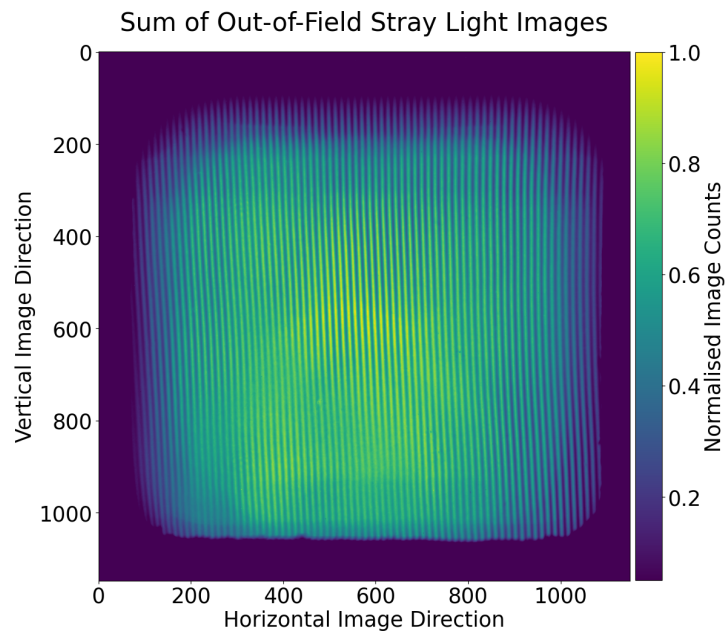


Figure A.9: PSM Out-of-Field Raster configured for the movement of the hexapod.



**Figure A.10:** The sum of all in-field PSF images provided by the PSM method shows that the PSF reflected from both diffraction gratings no longer overlap at the upper side of the image. Therefore, two PSFs next to each other are visible. The colour bar has been limited to 2000 counts to improve visualisation of the PSF positions.



**Figure A.11:** The PST measurement provides the normalised sum of all out-of-field stray light images in both the vertical and horizontal directions, from +4 degrees to -4 degrees.

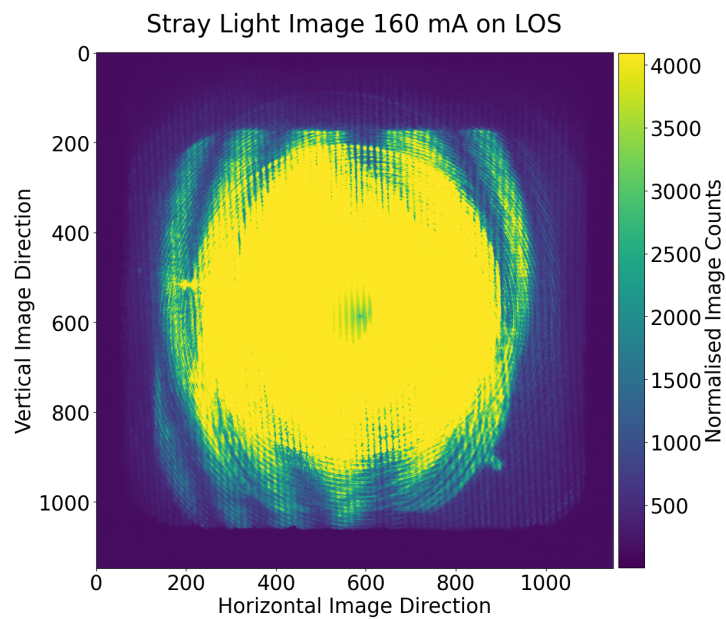


**Figure A.12:** At full laser power, the point source is positioned at the line of sight of the instrument. Although large parts of the instrument are saturated, the power increase can still be validated at the outer image regions.

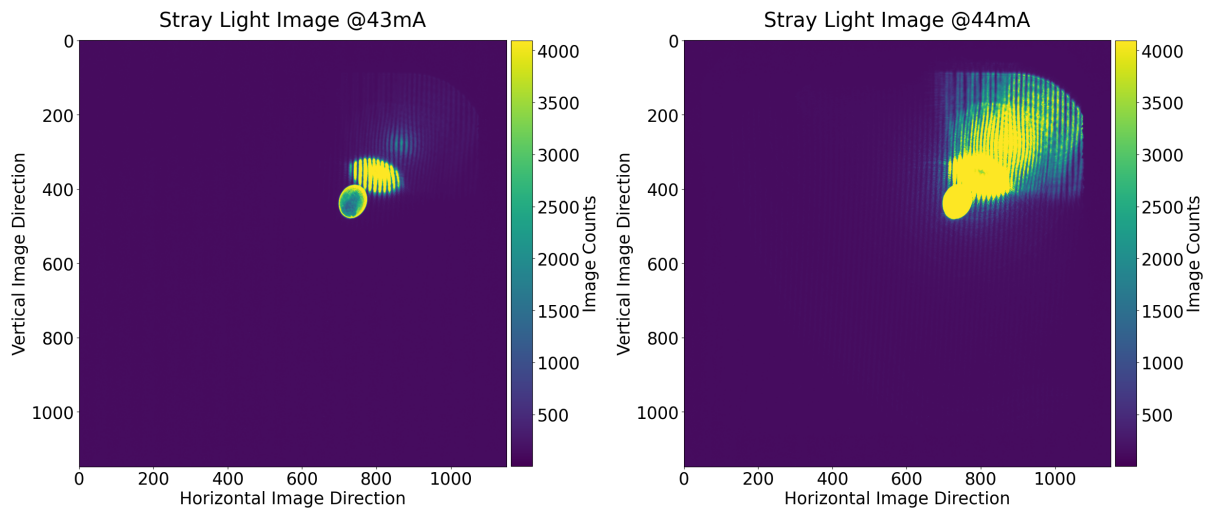


**Figure A.13:** Above the laser threshold, the in-field stray light images at 43 mA and 44 mA laser current demonstrate the complexity of higher order stray light effects and their interference. The PSF is positioned at +0.4 degrees vertically and +0.4 degrees horizontally.

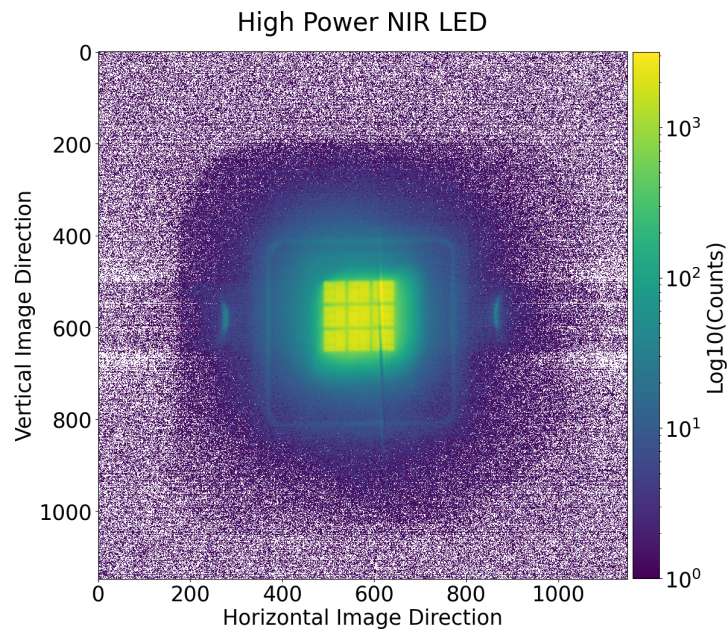


**Figure A.14:** High Power NIR LED imaged with the mACU. Even the wiring of the LED semiconductor is visible. The data was not usable for stray light estimation because the LED illuminates the surrounding surfaces

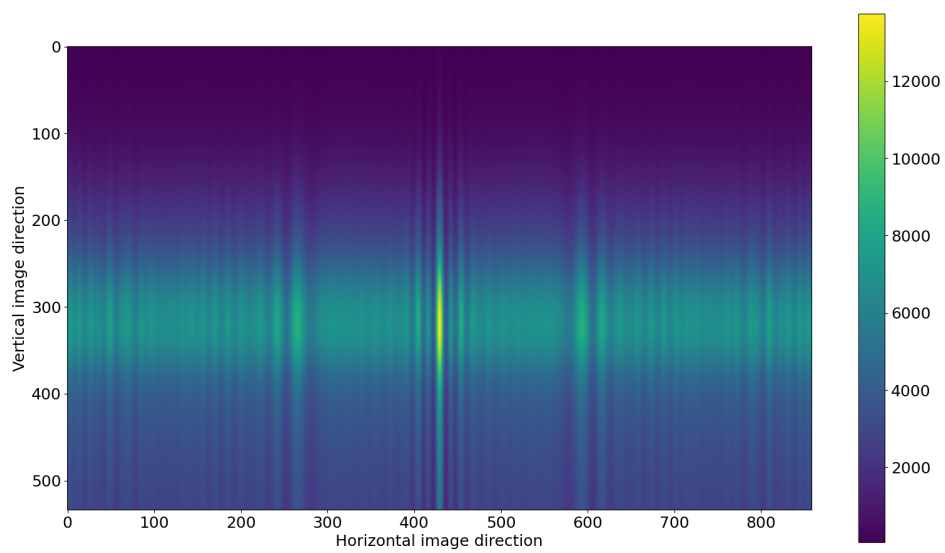


**Figure A.15:** Exemplary forward modelled measurements of  $O_2$ -A band emissions interferogram created with software packages *atmosimulation* and *o2aband*. The software was developed by Konstantin Ntokas

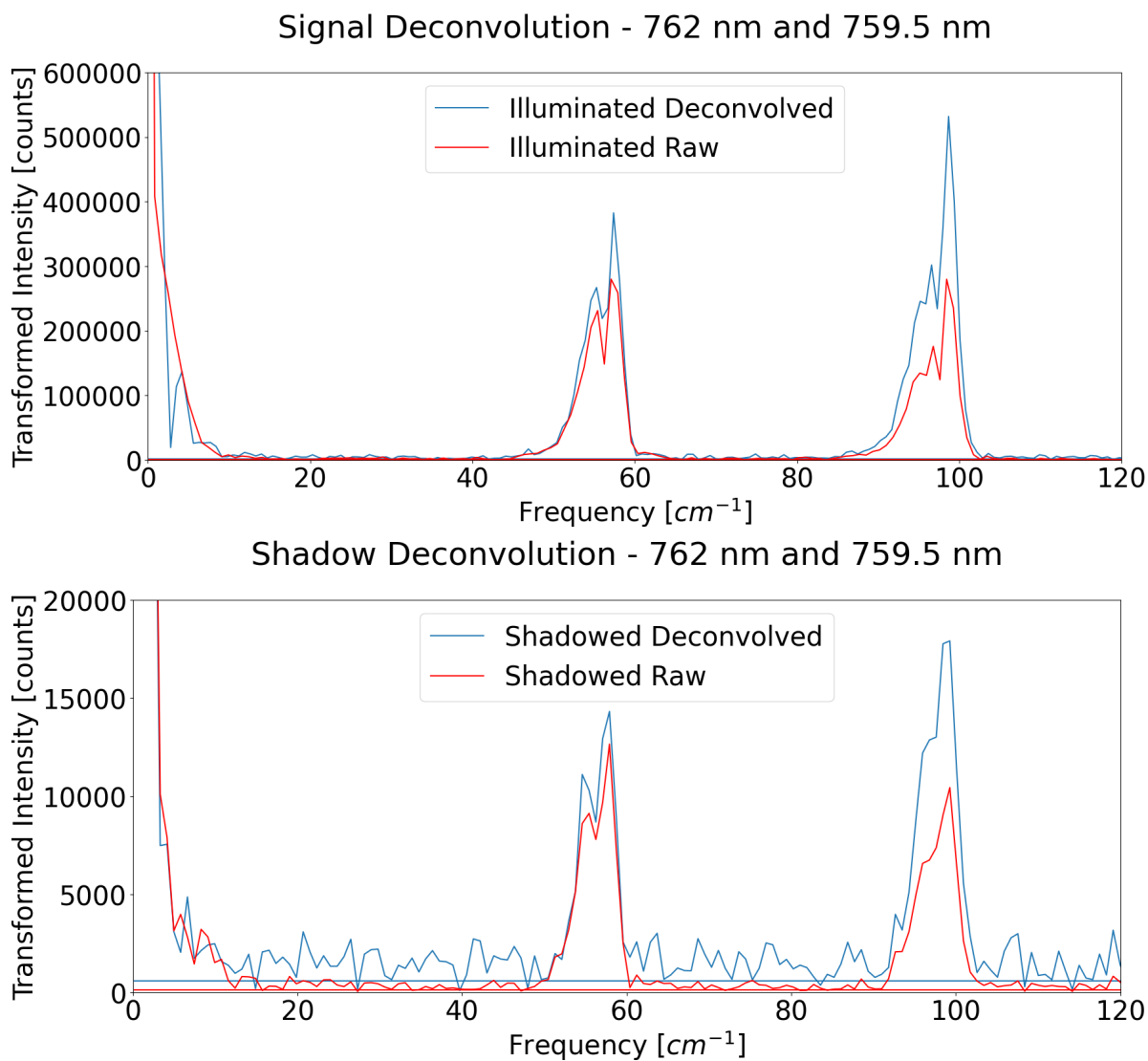


**Figure A.16:** The two superimposed interferograms were deconvoluted using a PSF kernel of 10x10, which was cropped from a previous broadband point source measurement. The shadowed region shows an increase in noise after deconvolution. No deconvolution parameters or methods were found that preserve the peak relation and decrease the stray light in the shadowed region.

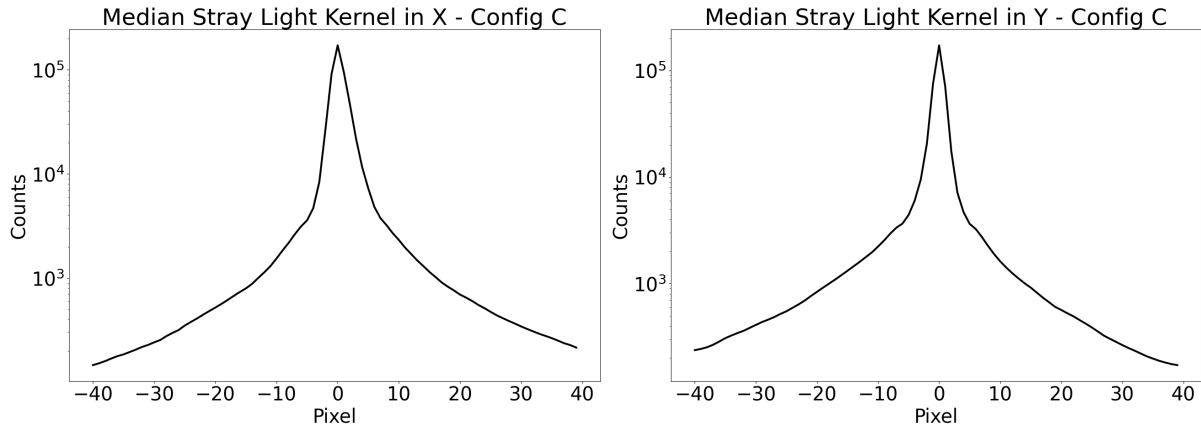


**Figure A.17:** Median stray light kernels for all PSM in-field measurements of configuration C. The low stray light descent to the outer regions causes the high stray light values for this configuration.

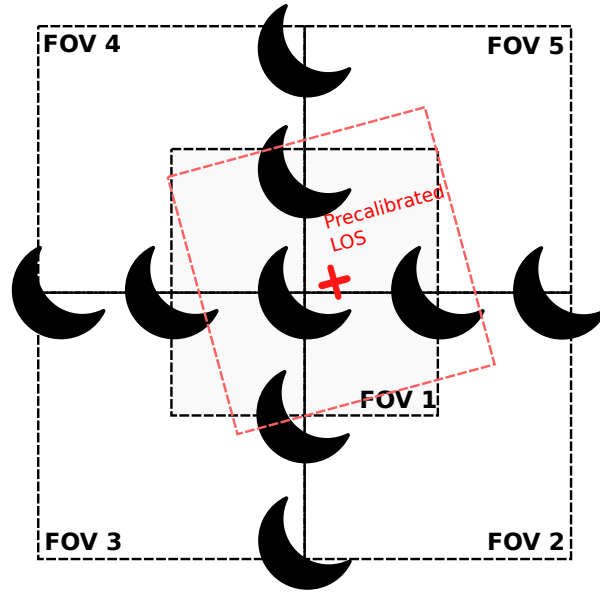


**Figure A.18:** The lunar disk raster used for in-orbit validation of LOS, in-field stray light and spatial resolution. The overlap of the five images increases the likelihood of the moon being fully captured in at least one image. The misalignment between the precalibrated LOS and the theoretical LOS should be evaluated and corrected first, before conducting out-of-field stray light measurements.

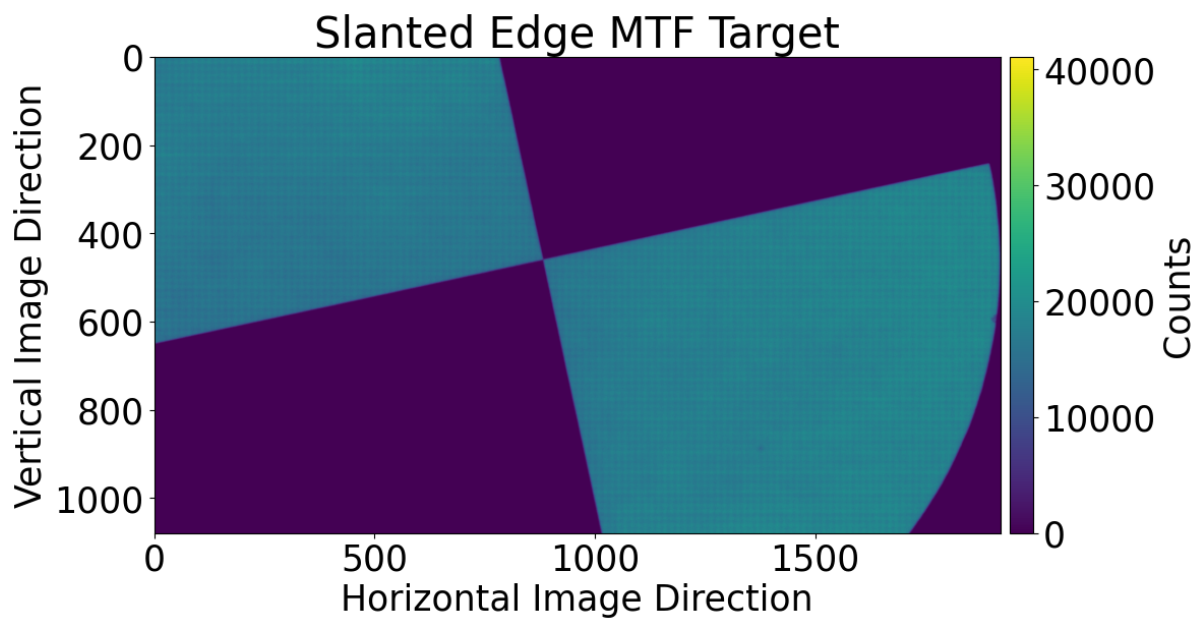


**Figure A.19:** The mACU is aligned with the autocollimator in order to align the focal point of the microscope objective with the focal point of the mACU by using an slanted edge target.

# References

- [1] M. Deiml, *Development of a Small Satellite Remote Sensing Payload for Passive Limb Sounding of the Atmospheric Oxygen Emission*. Dissertation, Uni Wuppertal, 2017.
- [2] R. Song, *Tomographic reconstruction of gravity wave parameters from satellite-borne airglow observations*. PhD thesis, University of Wuppertal, 2018.
- [3] J. Liu, *Study on a miniaturized satellite payload for atmospheric temperature measurements*. PhD thesis, Dissertation, Wuppertal, Bergische Universität, 2019.
- [4] Q. Chen, *Retrieval of atmospheric quantities from remote sensing measurements of nightglow emissions in the MLT region*. PhD thesis, Dissertation, Wuppertal, Bergische Universität, 2020.
- [5] Q. Gong, *Characterization and calibration of the AtmoLITE satellite instrument for the INSPIRESat-4 mission*. PhD thesis, University of Wuppertal, 2022.
- [6] O. Wroblowski, *Characterisation and In-Orbit Demonstration of a Heterodyne Spectrometer for Atmospheric Research from Small Satellites*. PhD thesis, University of Wuppertal, 2023.
- [7] K. Ntokas, *Development of a data processing chain for a spatial heterodyne interferometer measuring temperature in the mesosphere and lower thermosphere*. Dissertation, Bergische Universität Wuppertal, 2023. Dissertation, Bergische Universität Wuppertal, 2023.
- [8] M. Kaufmann, F. Olschewski, K. Mantel, B. Solheim, G. Shepherd, M. Deiml, J. Liu, R. Song, Q. Chen, O. Wroblowski, *et al.*, “A highly miniaturized satellite payload based on a spatial heterodyne spectrometer for atmospheric temperature measurements in the mesosphere and lower thermosphere,” *Atmospheric measurement techniques*, vol. 11, no. 7, pp. 3861–3870, 2018.
- [9] A. Ludewig, Q. Kleipool, R. Bartstra, R. Landzaat, J. Leloux, E. Loots, P. Meijering, E. van der Plas, N. Rozemeijer, F. Vonk, and P. Veefkind, “In-flight calibration results of the tropomi payload on board the sentinel-5 precursor satellite,” *Atmospheric Measurement Techniques*, vol. 13, no. 7, pp. 3561–3580, 2020.
- [10] D. Fussen, N. Baker, J. Deboscher, E. Dekemper, P. Demoulin, Q. Errera, G. Franssens, N. Mateshvili, N. Pereira, D. Pieroux, and F. Vanhellefont, “The altius atmospheric limb sounder,” *Journal of Quantitative Spectroscopy and Radiative Transfer*, vol. 238, p. 106542, 2019.

- [11] J. J. Remedios, R. J. Leigh, A. M. Waterfall, D. P. Moore, H. Sembhi, I. Parkes, J. Greenhough, M. P. Chipperfield, and D. Hauglustaine, “Mipas reference atmospheres and comparisons to v4.61/v4.62 mipas level 2 geophysical data sets,” *Atmospheric Chemistry and Physics Discussions*, vol. 7, pp. 9973–10017, 2007.
- [12] Y. Nollet and V. Leroy, “Joseki,” Feb. 2024.
- [13] M. P. Baldwin and T. J. Dunkerton, “Propagation of the arctic oscillation from the stratosphere to the troposphere,” *Journal of Geophysical Research: Atmospheres*, vol. 104, no. D24, pp. 30937–30946, 1999.
- [14] L. J. Gray, J. Beer, M. Geller, J. D. Haigh, M. Lockwood, K. Matthes, U. Cubasch, D. Fleitmann, G. Harrison, L. Hood, *et al.*, “Solar influences on climate,” *Reviews of Geophysics*, vol. 48, no. 4, 2010.
- [15] C. J. Wright, N. P. Hindley, M. J. Alexander, M. Barlow, L. Hoffmann, C. N. Mitchell, F. Prata, M. Bouillon, J. Carstens, C. Clerbaux, *et al.*, “Surface-to-space atmospheric waves from hunga tonga–hunga ha’apai eruption,” *Nature*, vol. 609, no. 7928, pp. 741–746, 2022.
- [16] A. K. Smith, “Global dynamics of the mlt,” *Surveys in Geophysics*, vol. 33, pp. 1177–1230, 2012.
- [17] M. Deiml, M. Kaufmann, P. Knieling, F. Olschewski, P. Toumpas, M. Langer, M. Ern, R. Koppmann, and M. Riese, “Dissect–development of a small satellite for climate research,” in *Proceedings of the 65th International Astronautical Congress, Toronto, Canada*, 2014.
- [18] P. Sheese, E. Llewellyn, R. Gattinger, A. Bourassa, D. Degenstein, N. Lloyd, and I. McDade, “Temperatures in the upper mesosphere and lower thermosphere from osiris observations of o2 a-band emission spectra,” *Canadian Journal of Physics*, vol. 88, no. 12, pp. 919–925, 2010.
- [19] R. Song, M. Kaufmann, J. Ungermann, M. Ern, G. Liu, and M. Riese, “Tomographic reconstruction of atmospheric gravity wave parameters from airglow observations,” *Atmospheric measurement techniques*, vol. 10, no. 12, pp. 4601–4612, 2017.
- [20] M. Touzeau, M. Vialle, A. Zellagui, G. Gousset, M. Lefebvre, and M. Pealat, “Spectroscopic temperature measurements in oxygen discharges,” *Journal of Physics D: Applied Physics*, vol. 24, p. 41, jan 1991.
- [21] E. Pannier and C. O. Laux, “RADIS: A nonequilibrium line-by-line radiative code for CO<sub>2</sub> and HITRAN-like database species,” *Journal of Quantitative Spectroscopy and Radiative Transfer*, vol. 222–223, pp. 12–25, jan 2019.
- [22] H. Community, “The HITRAN2020 molecular spectroscopic database,” *Journal of Quantitative Spectroscopy and Radiative Transfer*, vol. 277, p. 107949, jan 2022.
- [23] A. Bourassa, *The characterization and calibration of the OSIRIS infrared imager*. PhD thesis, University of Saskatchewan, 2003.

- [24] G. Jaross, P. K. Bhartia, G. Chen, M. Kowitt, M. Haken, Z. Chen, P. Xu, J. Warner, and T. Kelly, "Omps limb profiler instrument performance assessment," *Journal of Geophysical Research: Atmospheres*, vol. 119, no. 7, pp. 4399–4412, 2014.
- [25] M. Stevens, C. Englert, J. Harlander, K. Marr, B. Harding, C. Triplett, M. Mlynczak, T. Yuan, J. Evans, S. Mende, *et al.*, "Temperatures in the upper mesosphere and lower thermosphere from o2 atmospheric band emission observed by icon/mighti," *Space Science Reviews*, vol. 218, no. 8, p. 67, 2022.
- [26] P. Connes, "Spectromètre interférentiel à sélection par l'amplitude de modulation," *Journal de Physique et le Radium*, vol. 19, no. 3, pp. 215–222, 1958.
- [27] J. M. Harlander, *Spatial heterodyne spectroscopy: interferometric performance at any wavelength without scanning*. The University of Wisconsin-Madison, 1991.
- [28] C. R. Englert and J. M. Harlander, "Flatfielding in spatial heterodyne spectroscopy," *Appl. Opt.*, vol. 45, pp. 4583–4590, Jul 2006.
- [29] C. R. Englert, J. M. Harlander, J. G. Cardon, and F. L. Roesler, "Correction of phase distortion in spatial heterodyne spectroscopy," *Applied optics*, vol. 43, no. 36, pp. 6680–6687, 2004.
- [30] B. W. Smith and J. M. Harlander, "Imaging spatial heterodyne spectroscopy: theory and practice," in *Infrared Technology and Applications XXV*, vol. 3698, pp. 925–931, SPIE, 1999.
- [31] S. Milligan, J. W. Howard, B. E. Laubscher, B. W. Smith, R. R. Berggren, and J. M. Harlander, "Optical design of an imaging spatial heterodyne infrared spectrometer," in *Infrared Technology and Applications XXV*, vol. 3698, pp. 869–881, SPIE, 1999.
- [32] B. E. Laubscher, B. W. Smith, B. J. Cooke, P. C. LaDelfe, R. R. Berggren, P. V. Villeneuve, R. M. Goeller, G. M. Obbink, S. Milligan, J. W. Howard, *et al.*, "Infrared imaging spatial heterodyne spectrometer (irishs) experiment effort," in *Infrared Imaging Systems: Design, Analysis, Modeling, and Testing X*, vol. 3701, pp. 194–205, SPIE, 1999.
- [33] R. F. Horton, C. A. Conger, and L. Pelligrino, "High etendue imaging fourier transform spectrometer: initial results," in *Imaging Spectrometry III*, vol. 3118, pp. 380–390, SPIE, 1997.
- [34] C. R. Englert, M. H. Stevens, D. E. Siskind, J. M. Harlander, F. L. Roesler, H. M. Pickett, C. von Savigny, and A. J. Kochenash, "First results from the spatial heterodyne imager for mesospheric radicals (shimmer): Diurnal variation of mesospheric hydroxyl," *Geophysical Research Letters*, vol. 35, no. 19, 2008.
- [35] ASTM, "Standard test method for estimating stray radiant power ratio of dispersive spectrophotometers by the opaque filter method," tech. rep., ASTM, 2022.
- [36] J. M. Harlander, F. L. Roesler, J. G. Cardon, C. R. Englert, and R. R. Conway, "Shimmer: a spatial heterodyne spectrometer for remote sensing of earth's middle atmosphere," *Applied Optics*, vol. 41, no. 7, pp. 1343–1352, 2002.

- [37] J. M. Harlander, F. L. Roesler, C. R. Englert, J. G. Cardon, R. R. Conway, C. M. Brown, and J. Wimperis, "Robust monolithic ultraviolet interferometer for the shimmer instrument on stpsat-1," *Appl. Opt.*, vol. 42, pp. 2829–2834, May 2003.
- [38] Y. Lin, G. Shepherd, B. Solheim, M. Shepherd, S. Brown, J. Harlander, and J. Whiteway, "Introduction to spatial heterodyne observations of water (show) project and its instrument development," in *Proc. XIV Int. TOVS Study Conf., 25-31 May 2005, Beijing, China*, pp. 835–843, 2005.
- [39] J. Langille, D. Letros, A. Bourassa, B. Solheim, D. Degenstein, F. Dupont, D. Zawada, and N. D. Lloyd, "Spatial heterodyne observations of water (show) from a high-altitude airplane: characterization, performance, and first results," *Atmospheric Measurement Techniques*, vol. 12, no. 1, pp. 431–455, 2019.
- [40] J. M. Harlander and C. R. Englert, "Doppler asymmetric spatial heterodyne spectroscopy," Aug. 10 2010. US Patent 7,773,229.
- [41] C. R. Englert, D. D. Babcock, and J. M. Harlander, "Doppler asymmetric spatial heterodyne spectroscopy (dash): concept and experimental demonstration," *Appl. Opt.*, vol. 46, pp. 7297–7307, Oct 2007.
- [42] B. J. Harding, J. L. Chau, M. He, C. R. Englert, J. M. Harlander, K. D. Marr, J. J. Makela, M. Clahsen, G. Li, M. V. Ratnam, *et al.*, "Validation of icon-mighti thermospheric wind observations: 2. green-line comparisons to specular meteor radars," *Journal of Geophysical Research: Space Physics*, vol. 126, no. 3, p. e2020JA028947, 2021.
- [43] C. R. Englert, J. M. Harlander, C. M. Brown, K. D. Marr, I. J. Miller, J. E. Stump, J. Hancock, J. Q. Peterson, J. Kumler, W. H. Morrow, *et al.*, "Michelson interferometer for global high-resolution thermospheric imaging (mighti): instrument design and calibration," *Space science reviews*, vol. 212, pp. 553–584, 2017.
- [44] H. Gao, J. Xu, G.-M. Chen, Y. Zhu, M. He, W. Yuan, L. Sun, D. Li, and H. Liu, "Response of icon/mighti measured low-mid latitude oi630. 0 and oi557. 7 nm dayglow emissions to the 27 august 2021 geomagnetic storm," *Journal of Geophysical Research: Space Physics*, vol. 129, no. 1, p. e2023JA032070, 2024.
- [45] B. J. Harding, Y.-J. J. Wu, P. Alken, Y. Yamazaki, C. C. Triplett, T. J. Immel, L. C. Gasque, S. B. Mende, and C. Xiong, "Impacts of the january 2022 tonga volcanic eruption on the ionospheric dynamo: Icon-mighti and swarm observations of extreme neutral winds and currents," *Geophysical Research Letters*, vol. 49, no. 9, p. e2022GL098577, 2022.
- [46] K. Marr, C. Englert, and J. Harlander, "The indi instrument: A miniaturized implementation of the dash technique for measuring upper atmospheric oxygen winds," *Bulletin of the American Astronomical Society*, vol. 55, no. 3, p. 267, 2023.
- [47] J. M. Harlander, C. R. Englert, and K. D. Marr, "Mini-mighti: A prototype sensor for thermospheric red-line (630 nm) neutral wind measurements from a 6u cubesat," *Fourier Transform Spectroscopy*, pp. FTu4B–3, 2019.

- [48] J. M. Harlander and S. P. Laut, “Indi: A prototype optical sensor for measuring upper thermospheric dynamics from a smallsat,” in *Fourier Transform Spectroscopy*, pp. FM1B-4, Optica Publishing Group, 2023.
- [49] F. Olschewski, M. Kaufmann, K. Mantel, T. Neubert, H. Rongen, M. Riese, and R. Koppmann, “Atmocube a1: airglow measurements in the mesosphere and lower thermosphere by spatial heterodyne interferometry,” *Journal of applied remote sensing*, vol. 13, no. 2, pp. 024501–024501, 2019.
- [50] T. Neubert, H. Rongen, D. Froehlich, G. Schardt, M. Dick, T. Nysten, E. Zimmermann, M. Kaufmann, F. Olschewski, and S. van Waasen, “System-on-module-based long-life electronics for remote sensing imaging with cubesats in low-earth-orbits,” *Journal of applied remote sensing*, vol. 13, no. 3, pp. 032507–032507, 2019.
- [51] J. Florczak, K. Ntokas, T. Neubert, E. Zimmermann, H. Rongen, U. Clemens, M. Kaufmann, M. Riese, and S. van Waasen, “Bad pixel detection for on-board data quality improvement of remote sensing instruments in cubesats,” in *CubeSats and SmallSats for Remote Sensing VI*, vol. 12236, pp. 6–14, SPIE, 2022.
- [52] H. Shi, Z. Li, H. Ye, H. Luo, X. Wang, and W. Xiong, “Calibration of the greenhouse gas monitoring instrument (gmi) based on a digital calibration field network,” *Remote Sensing*, vol. 15, no. 2, 2023.
- [53] Q. Wang, H. Luo, Z. Li, H. Shi, Y. Han, and W. Xiong, “Greenhouse gases monitoring instrument on a gf-5 satellite-ii: correction of spatial and frequency-dependent phase distortion,” *Opt. Express*, vol. 31, pp. 3028–3045, Jan 2023.
- [54] G. K. Ackermann and J. Eichler, *Holography: a practical approach*. John Wiley & Sons, 2007.
- [55] J. Ungermann, *Tomographic reconstruction of atmospheric volumes from infrared limb-imager measurements*, vol. 106. Forschungszentrum Jülich, 2011.
- [56] Q. Chen, K. Ntokas, B. Linder, L. Krasauskas, M. Ern, P. Preusse, J. Ungermann, E. Becker, M. Kaufmann, and M. Riese, “Satellite observations of gravity wave momentum flux in the mesosphere and lower thermosphere (mlt): feasibility and requirements,” *Atmospheric Measurement Techniques*, vol. 15, no. 23, pp. 7071–7103, 2022.
- [57] E. Fest, *Stray Light Analysis and Control*. SPIE Press, 2013.
- [58] C. Pope and A. Baumgartner, “Light source for stray light characterisation of enmap spectrometers,” in *Sensors, Systems, and Next-Generation Satellites XXIII*, vol. 11151, pp. 452–459, SPIE, 2019.
- [59] S. Grabarnik, G. B. Courrèges-Lacoste, C. Pachot, L. Gambicorti, R. Rivière, and S. Riedl, “In-field and out-of-field stray light analysis for the copernicus sentinel 4 instrument,” in *International Conference on Space Optics—ICSO 2018*, vol. 11180, pp. 1027–1038, SPIE, 2019.

- [60] Y. Zong, S. W. Brown, B. C. Johnson, K. R. Lykke, and Y. Ohno, “Simple spectral stray light correction method for array spectroradiometers,” *Applied optics*, vol. 45, no. 6, pp. 1111–1119, 2006.
- [61] Gpixel, *GSENSE400BSI 4 Megapixels Scientific BSI CMOS Image Sensor Datasheet V1.1.12020*, 2020.
- [62] Thorlabs, “Camera noise and temperature tutorial,” 2024.
- [63] E. R. Fossum *et al.*, “Charge transfer noise and lag in cmos active pixel sensors,” in *Proc. 2003 IEEE Workshop on CCDs and Advanced Image Sensors, Elmau, Bavaria, Germany*, pp. 11–13, Citeseer, 2003.
- [64] P. J. J. Tol, T. A. van Kempen, R. M. van Hees, M. Krijger, S. Cadot, R. Snel, S. T. Persijn, I. Aben, and R. W. M. Hoogeveen, “Characterization and correction of stray light in tropomi-swir,” *Atmospheric Measurement Techniques*, vol. 11, no. 7, pp. 4493–4507, 2018.
- [65] C. J. Dennehy, A. A. Wolf, and D. K. Swanson, “Spacecraft line-of-sight jitter management and mitigation lessons learned and engineering best practices,” tech. rep., NASA, 2021.
- [66] T. Ott, A. Benoit, P. Van den Braembussche, and W. Fichter, “Esa pointing error engineering handbook,” in *8th International ESA Conference on Guidance, Navigation Control Systems*, p. 17, 2011.
- [67] S. Tukiainen, E. Kyrölä, P. Verronen, D. Fussen, L. Blanot, G. Barrot, A. Hauchecorne, and N. Lloyd, “Retrieval of ozone profiles from gomos limb scattered measurements,” *Atmospheric Measurement Techniques Discussions*, vol. 3, no. 5, pp. 4355–4382, 2010.
- [68] B. Rhodes, “Skyfield: High precision research-grade positions for planets and earth satellites generator,” *Astrophysics Source Code Library*, pp. ascl–1907, 2019.
- [69] E. Hecht, *Optik*. Walter de Gruyter GmbH & Co KG, 2023.
- [70] D. Tichenor and J. Goodman, “Coherent transfer function,” *JOSA*, vol. 62, no. 2, pp. 293–295, 1972.
- [71] B. T. Rowe, M. Jarvis, R. Mandelbaum, G. M. Bernstein, J. Bosch, M. Simet, J. E. Meyers, T. Kacprzak, R. Nakajima, J. Zuntz, *et al.*, “Galsim: The modular galaxy image simulation toolkit,” *Astronomy and Computing*, vol. 10, pp. 121–150, 2015.
- [72] Q. Kleipool, A. Ludewig, L. Babić, R. Bartstra, R. Braak, W. Dierssen, P.-J. Dewitte, P. Kenter, R. Landzaat, J. Leloux, *et al.*, “Pre-launch calibration results of the tropomi payload onboard the sentinel-5 precursor satellite,” *Atmospheric Measurement Techniques*, vol. 11, no. 12, pp. 6439–6479, 2018.
- [73] S. van der Walt, J. L. Schönberger, J. Nunez-Iglesias, F. Boulogne, J. D. Warner, N. Yager, E. Gouillart, T. Yu, and the scikit-image contributors, “scikit-image: image processing in python,” *PeerJ*, vol. 2, p. e453, jun 2014.

- [74] S. Community, “SciPy 1.0: Fundamental Algorithms for Scientific Computing in Python,” *Nature Methods*, vol. 17, pp. 261–272, 2020.
- [75] A. Community, “The Astropy Project: Sustaining and Growing a Community-oriented Open-source Project and the Latest Major Release (v5.0) of the Core Package,” *The Astrophysical Journal*, vol. 935, no. 2, 2022.
- [76] F. Orieux, J.-F. Giovannelli, and T. Rodet, “Bayesian estimation of regularization and point spread function parameters for wiener–hunt deconvolution,” *JOSA A*, vol. 27, no. 7, pp. 1593–1607, 2010.
- [77] C. Beck, R. Rezaei, and D. Fabbian, “Stray-light contamination and spatial deconvolution of slit-spectrograph observations,” *Astronomy & Astrophysics*, vol. 535, p. A129, 2011.
- [78] S. M. Jefferies and J. C. Christou, “Restoration of astronomical images by iterative blind deconvolution,” *Astrophysical Journal v. 415, p. 862*, vol. 415, p. 862, 1993.
- [79] Y. Zong, S. W. Brown, G. Meister, R. A. Barnes, and K. R. Lykke, “Characterization and correction of stray light in optical instruments,” in *Sensors, Systems, and Next-Generation Satellites XI*, vol. 6744, pp. 422–432, SPIE, 2007.
- [80] P. Gamet, S. Fourest, T. Sprecher, and E. Hillairet, “Measuring, modeling and removing optical straylight from venus super spectral camera images,” in *International Conference on Space Optics—ICSO 2018*, vol. 11180, pp. 1638–1661, SPIE, 2019.
- [81] L. Clermont, C. Michel, E. Mazy, C. Pachot, N. Daddi, C. Mastrandread, and Y. Stockman, “Stray-light calibration and correction for the metop-sg 3mi mission,” in *Observatory Operations: Strategies, Processes, and Systems VII*, vol. 10704, pp. 71–79, SPIE, 2018.
- [82] J. M. Hughes, C. E. DeForest, and D. B. Seaton, “Coma off it: Regularizing variable point-spread functions,” *The Astronomical Journal*, vol. 165, no. 5, p. 204, 2023.
- [83] C. T. Slater, P. Harding, and J. C. Mihos, “Removing internal reflections from deep imaging data sets,” *Publications of the Astronomical Society of the Pacific*, vol. 121, no. 885, p. 1267, 2009.
- [84] E. Karabal, P.-A. Duc, H. Kuntschner, P. Chaniel, J.-C. Cuillandre, and S. Gwyn, “A deconvolution technique to correct deep images of galaxies from instrumental scattered light,” *Astronomy & Astrophysics*, vol. 601, p. A86, 2017.
- [85] L. Clermont, W. Uhring, and M. Georges, “Stray light characterization with ultrafast time-of-flight imaging,” *Scientific reports*, vol. 11, no. 1, pp. 1–9, 2021.
- [86] V. Demjanov, “What and how does a michelson interferometer measure,” *arXiv preprint arXiv:1003.2899*, 2010.
- [87] A. Matter, B. Lopez, S. Lagarde, W. C. Danchi, S. Robbe-Dubois, R. G. Petrov, and R. Navarro, “Parasitic interference in long baseline optical interferometry: Requirements for hot jupiter-like planet detection,” *The Astrophysical Journal*, vol. 706, no. 2, p. 1299, 2009.

- [88] V. Khodnevych and D. Simeoni, “Stray light analysis of compact gas imager,” in *International Conference on Space Optics—ICSO 2022*, vol. 12777, pp. 2284–2291, SPIE, 2023.
- [89] P. Etcheto, A. Rosak, P. Parant, and O. Vigier, “Coherent modeling and stray light in a static fourier transform spectrometer,” in *Optical Design and Engineering*, vol. 5249, pp. 22–33, SPIE, 2004.
- [90] I. S. Sullivan, “Fast holographic deconvolution: A new technique for precision radio interferometry,” *The Astrophysical Journal*, vol. 759, p. 17, oct 2012.
- [91] Y. Cotte, F. M. Toy, C. Arfire, S. S. Kou, D. Boss, I. Bergoënd, and C. Depeursinge, “Realistic 3d coherent transfer function inverse filtering of complex fields,” *Biomedical optics express*, vol. 2, no. 8, pp. 2216–2230, 2011.
- [92] E. Kristensson, J. Bood, M. Alden, E. Nordström, J. Zhu, S. Hultdt, P.-E. Bengtsson, H. Nilsson, E. Berrocal, and A. Ehn, “Stray light suppression in spectroscopy using periodic shadowing,” *Optics express*, vol. 22, no. 7, pp. 7711–7721, 2014.
- [93] R. P. Breault, “Problems and techniques in stray radiation suppression,” in *Stray Light Problems in Optical Systems*, vol. 107, pp. 2–23, SPIE, 1977.
- [94] A. W. Greynolds, “Formulas for estimating stray-radiation levels in well-baffled optical systems,” in *Radiation scattering in optical systems*, vol. 257, pp. 39–49, SPIE, 1981.
- [95] J. Gumbel, L. Megner, O. M. Christensen, N. Ivchenko, D. P. Murtagh, S. Chang, J. Dillner, T. Ekebrand, G. Giono, A. Hammar, *et al.*, “The mats satellite mission—gravity wave studies by mesospheric airglow/aerosol tomography and spectroscopy,” *Atmospheric Chemistry and Physics*, vol. 20, no. 1, pp. 431–455, 2020.
- [96] M. Kaufmann, K. Ntokas, D. Sivil, B. Michel, Q. Chen, F. Olschewski, O. Wroblowski, T. Augspurger, M. Miebach, J. Ungermann, *et al.*, “Optical design and straylight analyses of a spatial heterodyne interferometer for the measurement of atmospheric temperature from space,” in *CubeSats, SmallSats, and Hosted Payloads for Remote Sensing VII*, vol. 12689, pp. 13–19, SPIE, 2023.
- [97] A. Crocherie, J. Pond, F. D. Gomez, K. Channon, and F. Fantoni, “Micro to macro scale simulation coupling for stray light analysis,” *Optics Express*, vol. 29, no. 23, pp. 37639–37652, 2021.
- [98] B. Harnisch, A. Deep, R. Vink, and C. Coatantiec, “Grating scattering brdf and imaging performances: A test survey performed in the frame of the flex mission,” in *International Conference on Space Optics—ICSO 2012*, vol. 10564, pp. 697–706, SPIE, 2017.
- [99] C. Palmer and E. G. Loewen, *Diffraction grating handbook*, 2005.
- [100] R. Steiner, A. Pesch, L. H. Erdmann, M. Burkhardt, A. Gatto, R. Wipf, T. Diehl, H. Vink, and B. van den Bosch, “Fabrication of low straylight holographic gratings for space applications,” in *Imaging Spectrometry XVIII*, vol. 8870, pp. 105–113, SPIE, 2013.

- [101] C. Emde, R. Buras-Schnell, A. Kylling, B. Mayer, J. Gasteiger, U. Hamann, J. Kylling, B. Richter, C. Pause, T. Dowling, and L. Bugliaro, “The libradtran software package for radiative transfer calculations (version 2.0.1),” *Geoscientific Model Development*, vol. 9, no. 5, pp. 1647–1672, 2016.
- [102] R. Datla, J. P. Rice, K. R. Lykke, B. C. Johnson, J. J. Butler, and X. Xiong, “Best practice guidelines for pre-launch characterization and calibration of instruments for passive optical remote sensing,” *Journal of Research of the National Institute of Standards and Technology*, vol. 116, no. 2, p. 621, 2011.
- [103] J. Tansock, D. Bancroft, J. Butler, C. Cao, R. Datla, S. Hansen, D. Helder, R. Kacker, H. Latvakoski, M. Mylnczak, *et al.*, *Guidelines for radiometric calibration of electro-optical instruments for remote sensing*, 2015.
- [104] A. Ludewig, Q. Kleipool, R. Bartstra, R. Landzaat, J. Leloux, E. Loots, P. Meijering, E. van der Plas, N. Rozemeijer, F. Vonk, *et al.*, “In-flight calibration results of the tropomi payload on board the sentinel-5 precursor satellite,” *Atmospheric Measurement Techniques*, vol. 13, no. 7, pp. 3561–3580, 2020.
- [105] X. Xiong, A. Angal, J. Sun, T. Choi, and E. Johnson, “On-orbit performance of modis solar diffuser stability monitor,” *Journal of Applied Remote Sensing*, vol. 8, no. 1, pp. 083514–083514, 2014.
- [106] J. Sun, R. Eplee Jr, X. Xiong, T. Stone, G. Meister, and C. McClain, “Modis and seawifs on-orbit lunar calibration,” in *Earth Observing Systems XIII*, vol. 7081, pp. 277–285, SPIE, 2008.
- [107] K. D. Marr, W. H. Morrow, C. M. Brown, C. R. Englert, J. M. Harlander, A. Cerrato, K. Lamport, and S. E. Harris, “Calibration lamp design, characterization, and implementation for the michelson interferometer for global high-resolution thermospheric imaging instrument on the ionospheric connection satellite,” *Optical Engineering*, vol. 58, no. 5, pp. 054104–054104, 2019.
- [108] A. Gerace and M. Montanaro, “Derivation and validation of the stray light correction algorithm for the thermal infrared sensor onboard landsat 8,” *Remote Sensing of Environment*, vol. 191, pp. 246–257, 2017.
- [109] J. J. Shea, “Lunar limb knife-edge optical transfer function measurements,” *Journal of Electronic Imaging*, vol. 8, no. 2, pp. 196–208, 1999.
- [110] M. Estriebeau and P. Magnan, “Fast mtf measurement of cmos imagers using iso 12333 slanted-edge methodology,” in *Detectors and Associated Signal Processing*, vol. 5251, pp. 243–252, SPIE, 2004.
- [111] T. Wilson and X. Xiong, “Modulation transfer function characterization for goes-16 advanced baseline imager using lunar observations,” in *Earth Observing Systems XXIV*, vol. 11127, pp. 460–467, SPIE, 2019.
- [112] Z. Wang and X. Xiong, “Viirs on-orbit spatial characterization using the moon,” *IEEE Geoscience and Remote Sensing Letters*, vol. 11, no. 6, pp. 1116–1120, 2013.

- [113] G. R. Keller, T. Chang, and X. Xiong, “Mtf analysis using lunar observations for himawari-8/ahi,” in *Earth Observing Systems XXII*, vol. 10402, pp. 757–766, SPIE, 2017.
- [114] T. Wilson and X. Xiong, “Surface corrected lunar mtf measurements in modis and viirs using the sp model,” *IEEE Transactions on Geoscience and Remote Sensing*, vol. 60, pp. 1–12, 2022.
- [115] S. Ando and K. Tanaka, “In-orbit straylight characterization and correction of optical radiometer using the moon image,” *Mechanical Engineering Journal*, vol. 6, no. 6, pp. 19–00098, 2019.
- [116] J. Caron and C. Rollins, “Improved lunar edge response function for on-orbit mtf calibration using albedo lunar flattening,” in *Proc. EUMETSAT Meteorological Satellite Conference*, 2018.
- [117] J. Ungermann, A. Kleinert, G. Maucher, I. Bartolomé, F. Friedl-Vallon, S. Johansson, L. Krasauskas, and T. Neubert, “Quantification and mitigation of the airborne limb imaging ftir gloria instrument effects and uncertainties,” *Atmospheric Measurement Techniques Discussions*, vol. 2021, pp. 1–69, 2021.
- [118] C. H. Acton Jr, “Ancillary data services of nasa’s navigation and ancillary information facility,” *Planetary and Space Science*, vol. 44, no. 1, pp. 65–70, 1996.
- [119] L. Clermont, C. Michel, and Y. Stockman, “Stray light correction algorithm for high performance optical instruments: The case of metop-3mi,” *Remote Sensing*, vol. 14, no. 6, 2022.
- [120] M.-W. Optical, *Examples for Applications of Collimators, Telescopes, Visual and Electronic Autocollimators*, 2016.
- [121] O. Svelto, D. C. Hanna, *et al.*, *Principles of lasers*, vol. 1. Springer, 2010.
- [122] P. Guillard, T. Rodet, S. Ronayette, J. Amiaux, A. Abergel, V. Moreau, J. Augueres, A. Bensalem, T. Orduna, C. Nehmé, *et al.*, “Optical performance of the jwst/miri flight model: characterization of the point spread function at high resolution,” in *Space Telescopes and Instrumentation 2010: Optical, Infrared, and Millimeter Wave*, vol. 7731, pp. 166–178, SPIE, 2010.
- [123] R. Samadi, A. Deru, D. Reese, V. Marchiori, E. Grolleau, J. Green, M. Pertenais, Y. Lebreton, S. Deheuvels, B. Mosser, *et al.*, “The plato solar-like light-curve simulator-a tool to generate realistic stellar light-curves with instrumental effects representative of the plato mission,” *Astronomy & Astrophysics*, vol. 624, p. A117, 2019.
- [124] M. M. McKerns, L. Strand, T. Sullivan, A. Fang, and M. A. Aivazis, “Building a framework for predictive science,” *arXiv preprint arXiv:1202.1056*, 2012.
- [125] T. M. Jeong and J. Lee, “Generation of high-intensity laser pulses and their applications,” *High Energy and Short Pulse Lasers*, vol. 1, 2016.
- [126] V. Leroy, Y. Nollet, S. Schunke, N. Misk, and Y. Govaerts, “Eradiate radiative transfer model,” June 2024.

- [127] G. Anderson, S. Clough, F. Kneizys, J. Chetwynd, and E. Shettle, “Afgl atmospheric constituent profiles,” *Environ. Res. Pap.*, vol. 954, pp. 1–46, 1986.
- [128] P. L. Richards, “Bolometers for infrared and millimeter waves,” *Journal of Applied Physics*, vol. 76, no. 1, pp. 1–24, 1994.
- [129] C. Toledano, S. Taylor, A. Barreto, S. Adriaensen, A. Berjón, A. Bialek, R. González, E. Williams, and M. Bouvet, “Lime: Lunar irradiance model of esa, a new tool for the absolute radiometric calibration using the moon,” *EGUsphere*, vol. 2023, pp. 1–39, 2023.
- [130] S. D. Miller and R. E. Turner, “A dynamic lunar spectral irradiance data set for npoess/viirs day/night band nighttime environmental applications,” *IEEE Transactions on Geoscience and Remote Sensing*, vol. 47, no. 7, pp. 2316–2329, 2009.
- [131] N. Ahmad, M. S. A. M. Nawawi, M. Z. Zainuddin, Z. M. Nasir, R. M. Yunus, and I. Mohamed, “A new crescent moon visibility criteria using circular regression model: A case study of teluk kemang, malaysia,” *Sains Malaysiana*, vol. 49, no. 4, pp. 859–870, 2020.
- [132] A. J. P. Aparicio, J. Vaquero-Martínez, M. C. Gallego, M. Antón, and J. M. Vaquero, “Validation of precipitable water vapor estimates from an inexpensive infrared thermometer,” *Journal of Atmospheric and Solar-Terrestrial Physics*, vol. 249, p. 106107, 2023.
- [133] E. Marchand, “Derivation of the point spread function from the line spread function,” *JOSA*, vol. 54, no. 7, pp. 915–919, 1964.
- [134] E. Marchand, “From line to point spread function: the general case,” *JOSA*, vol. 55, no. 4, pp. 352–354, 1965.
- [135] A. Mallama and J. L. Hilton, “Computing apparent planetary magnitudes for the astronomical almanac,” *Astronomy and computing*, vol. 25, pp. 10–24, 2018.
- [136] G. G. Pethuraja, J. W. Zeller, R. E. Welser, A. K. Sood, H. Efstathiadis, and P. S. Wijewarnasuriya, “Nanostructured antireflection coatings for infrared sensors and applications,” in *Infrared Sensors, Devices, and Applications VIII*, vol. 10766, pp. 99–108, SPIE, 2018.
- [137] K. Minoglou, D. S. S. Bello, D. S. Tezcan, L. Haspeslagh, J. Van Olmen, B. Merry, C. Cavaco, F. Mazzamuto, I. Toqué-Trésonne, R. Moirin, *et al.*, “A platform for european cmos image sensors for space applications,” in *International Conference on Space Optics—ICSO 2014*, vol. 10563, pp. 26–34, SPIE, 2017.
- [138] Int. Image Sensors Society, *Near Infrared Quantum Efficiency Simulations for CMOS Image Sensors*, 2023.
- [139] Int. Image Sensors Society, *Improved QE in CMOS image sensors with nano-black antireflection layer*, 2023.
- [140] Q. D. GmbH, *Low dark current deep-depletion (LDC-DD) technology A new standard for low-light NIR spectroscopy*, 2020.

# Acronyms

ACU	AtmoX Calibration Unit
AR	Anti-Reflection
ASE	Amplified Spontaneous Emission
BSDF	Bidirectional Scattering Distribution Function
BSDF	Computer Aided Design
BSL	Background Stray Light
EQE	External Quantum Efficiency
FHWM	Full Width at Half Maximum
FM	Flight Model
FOV	Field of View
GSL	Ghost Stray Light
ISHS	Imaging Spatial Heterodyne Interferometer
LOS	Line-of-Sight
LSL	Lunar Stray Light
LVLH	Local Vertical Local Horizontal
mACU	modular AtmoX Calibration Unit
MLT	Mesosphere and Lower Thermosphere
MTF	Modulation Transfer Function
NEP	Noise-Equivalent Power
NIR	Near-infrared
NSR	Noise to Signal Ratio
OPL	Optical Path Length

OTF Optical Transfer Function  
PSF Point Spread Function  
PSFO Point Source Focusing Optics  
PSM Point Source Mapping  
PST Point Source Transmittance  
PV Peak-to-Valley  
QM Qualification Model  
RMS Root Mean Square  
RSL Ronchi Stray Light  
SDF Stray-Light Distribution Function  
SHI Spatial Heterodyne Interferometer  
SHS Spatial Heterodyne Spectroscopy  
SLNR Stray Light to Noise Ratio  
SNR Signal-to-Noise-Ratio  
TIFSL Total In-Field Stray Light  
TLE Two Line Elements  
TSR Total Stray Light to Signal Ratio